Time-resolved Multiplexed Förster Resonance Energy Transfer for Nucleic Acid Biosensing

Jiajia Guo

NNT : 2019SACLS162

Time-resolved Multiplexed Förster Resonance Energy Transfer for Nucleic Acid Biosensing

Thèse de doctorat de l'Université Paris-Saclay
préparée à l'Université Paris-Sud

École doctorale n°575:
Electrical, Optical, Bio: PHYSICS_AND_ENGINEERING (EOBE)
Spécialité de doctorat: Physique
(Electronique et Optoélectronique, Nano et Microtechnologies)

Thèse présentée et soutenue à Orsay, le 18 Juin 2019

Mme Jiajia GUO

Composition du Jury :

Mme Rachel Méallet-Renault Professeure, Université Paris-Sud	Présidente
Mme Julia Pérez-Prieto Professeure, University of Valencia	Rapporteur
M. Marcus Wilhelmsson Professeur, Chalmers University Gothenburgh	Rapporteur
M. Andreas Reisch Maître de conférences, Université de Strasbourg	Examinateur
M. Niko Hildebrandt Professeur, Université Paris-Sud	Directeur de thèse

Thèse de doctorat

université PARIS-SACLAY
ÉCOLE DOCTORALE
Physique et ingénierie : électrons, photons, sciences du vivant (EOBE)

Titre: Transfert d'énergie par résonance de type Förster résolu en temps pour la bio-détection multiplexée des acides nucléiques

Mots clés: FRET, complexe de lanthanide, multiplexage, résolue dans le temps, acides nucléiques

Résumé: Les biomarqueurs à base d'acides nucléiques, qui sont impliqués dans le contrôle de l'expression génétique, sont spécifiques de nombreux types de cancers. Les applications basées sur le transfert d'énergie par résonance de Förster (FRET) sont parmi les plus prometteuses pour la biodétection d'acides nucléiques. Comme la détection simultanée de plusieurs acides nucléiques est très demandée et que le multiplexage spectral est limité par des interférences (optical crosstalk), le multiplexage temporel est utilisé ici pour ajouter de nouvelles possibilités de multiples détections simultanées. La thèse porte sur le développement de systèmes comprenant différentes distances entre molécules donneuses et acceptrices de FRET (Terbium vers fluorophores) pour créer des signaux d'intensité spécifiques correspondant à différentes séquences d'acides nucléiques. Les distances Tb-to-dye peuvent être arrangées en positionnant spécifiquement le donneur Tb sur des molécules d'ADN de différentes longueurs. Les technologies d'amplification d'acides nucléiques, telles que la réaction d'hybridation en chaîne (HCR) et l'amplification circulaire de l'ADN (RCA), ont été utilisées pour obtenir simplicité, rapidité, sélectivité et sensibilité dans la détection d'acides nucléiques. Le multiplexage temporel du signal de FRET a également été combiné avec le multiplexage spectral (couleur) pour le démultiplier. De plus, la possibilité d'un multiplexage temporel à base de nanoparticules a été démontrée.

Title: Time-resolved Multiplexed Förster Resonance Energy Transfer for Nucleic Acid Biosensing

Keywords: FRET, lanthanide complex, multiplexing, time-resolved, nucleic acid

Abstract: Nucleic acid biomarkers, which involve in gene expression control, are found specific for many kinds of cancers. Förster Resonance Energy Transfer (FRET) based applications are one of the most promising for nucleic acid biosensing. As parallel detection of multiple nucleic acids is highly demanded and spectral multiplexing is limited by optical crosstalk, temporal multiplexing is used for opening another dimension of the multiplexing. The thesis focuses on developing different Tb-to-dye FRET distances to create specific intensity signals corresponding to different nucleic acid sequences. The Tb-dye distances can be tuned by specific location of the Tb donor using different lengths of DNA. Amplification technologies, such as hybridization chain reaction (HCR) and rolling circle amplification (RCA), are used to achieve simplicity, rapidity, selectivity, and sensitivity of nucleic acid detection. Temporal multiplexing FRET was also combined with spectral (color) multiplexing for higher order multiplexed detection. Moreover, a single Tb-QD FRET modeling demonstrated the possibility of nanoparticle-based temporal multiplexing.

Université Paris-Saclay
Espace Technologique / Immeuble Discovery
Route de l'Orme aux Merisiers RD 128 / 91190 Saint-Aubin, France

Acknowledgment

I would like to convey my heartfelt gratitude and sincere appreciation to all people who have helped and inspired me during my doctoral study. This thesis would not have been possible without those supports from many people.

First, I would like to express my special appreciation and thanks to my supervisor Professor Dr. Niko Hildebrandt, for his trust in my abilities, the liberties in the laboratory, opportunities to attend to different conferences and his endless support. His perpetual energy and enthusiasm in research extremely motivated me in my studies. I appreciate all his invaluable contributions of time and advice on both research and life in the last four years. I could not have imagined having a better supervisor than him.

My sincere thanks also go to Prof. Dr. Julia Pérez-Prieto and Prof. Dr. Marcus Wilhelmsson for being the reviewers of my Ph.D. thesis.

I also want to thank our collaborator Dr. Igor Medintz for his kindness and scientific support, and all the co-authors of my publications.

Many thanks to all former and current members of the NanoBioPhotonics group, special thanks to Dr. Xue Qiu, Dr. Shashi Bhuckory and Dr. Yu-tang Wu for their continuous guidance, patience and valuable time devoted in sharing their technical and scientific knowledge with me. I also want to thank Ms. Jingyue Xu for spending a lot of happy dinner and weekend's time with me together, Dr. Thomas Plénat for improving my drive skills.

My gratefully acknowledge to Dr. Monique Chan-Hout for teaching me French. I learned a lot from her, not only French, but also her positive and optimistic attitude towards life.

I thanks China Scholarship Council for supporting the funding of my Ph.D. study.

Last but not least, my deepest gratitude goes to my parents, my boyfriend Bingrun Liu and my best friend Haiwa Zhang for their unflagging love and support throughout my life.

List of publications

Original publications

1. Jiajia Guo, Carlos Mingoes, Xue Qiu, and Niko Hildebrandt. "Simple, Amplified, and Multiplexed Detection of MicroRNAs Using Time-Gated FRET and Hybridization Chain Reaction." *Analytical Chemistry* 91, no. 4 (2019): 3101−3109.
2. Jiajia Guo, Xue Qiu (co-first author), Carlos Mingoes, Jeffrey R. Deschamps, Kimihiro Susumu, Igor L. Medintz, and Niko Hildebrandt. "Conformational Details of Quantum Dot-DNA Resolved by Förster Resonance Energy Transfer Lifetime Nanoruler." *ACS Nano* 13, no.1 (2018): 505-514.
3. Xue Qiu, Jiajia Guo (co-first author), Jingyue Xu, and Niko Hildebrandt. "Three-Dimensional FRET Multiplexing for DNA Quantification with Attomolar Detection Limits." *The journal of physical chemistry letters* 9, no. 15 (2018): 4379-4384.
4. Xue Qiu, Jingyue Xu, Jiajia Guo, Akram Yahia Ammar, Nikiforos-Ioannis Kapetanakis, Isabelle Duroux-Richard, Julia Unterluggauer et al. "Advanced microRNA-based cancer diagnostics using amplified time-gated FRET." *Chemical Science* 9, no. 42 (2018): 8046-8055.
5. Xue Qiu, Jiajia Guo, Zongwen Jin, Alexandra Petreto, Igor L. Medintz, and Niko Hildebrandt. "Multiplexed Nucleic Acid Hybridization Assays Using Single-FRET-Pair Distance-Tuning." *Small* 13, no. 25 (2017): 1700332.

Oral presentations

1. Jiajia Guo, Xue Qiu, Carlos Mingoes, Jeffrey Deschamps, Igor Medintz, Niko Hildebrandt. Temporal multiplexing FRET: using single Tb-to-quantum dot pair distance-tuning. *SPIE Photonics West*, San Francisco, USA, **2019 (Invited talk)**
2. Jiajia Guo, Xue Qiu, Carlos Mingoes, Jingyue Xu, Niko Hildebrandt. Temporal multiplexing of microRNA detection using Tb-dye FRET and amplifications. *10th International Conference on f-Elements (ICFE-10)*, Lausanne, Switzerland, **2018 (Invited talk)**
3. Jiajia Guo, Qiu, Xue, Zongwen Jin, Igor L. Medintz, and Niko Hildebrandt. Lifetime-multiplexed microRNA detection based on distance-dependent FRET from Terbium-Quantum Dot. *Fluorescent Biomolecules and Their Building Blocks.* Tianjin, China, **2016 (Short talk)**

Poster presentations

1. Jiajia Guo, Qiu, Xue, Zongwen Jin, Igor L. Medintz, and Niko Hildebrandt. One Quantum Dot Based Time-Gated Förster Resonance Energy Transfer for MicroRNA Duplexing. *Förster resonance energy transfer in life sciences.* Göttingen, Germany, **2016**

2. Jiajia Guo, Qiu, Xue, Zongwen Jin, Igor L. Medintz, and Niko Hildebrandt. Multiplexed Nucleic Acid Hybridization Assays Using Single Tb-to-Quantum Dot FRET Pair Distance-Tuning. *15th Conference on Methods and Applications in Fluorescence (MAF 15).* Bruges, Belgium, **2017**

CONTENTS

1. Introduction

Cancer kills millions of people every year and it is one of the greatest health challenges of human beings. The 2018 Nobel Prize in Physiology or Medicine was awarded to James P. Allison and Tasuku Honjo for their discovery of cancer therapy by inhibition of negative immune regulation. If cancer can be diagnosed at an early stage, it will greatly increase the chance for successful treatment. Recognizing possible warning signs of cancer and taking prompt action leads to early diagnosis.

One of the best ways to diagnose cancer early is to use serum or tissue biomarkers. Cancer biomarkers can be DNA, RNA, proteins, metabolites, or processes such as apoptosis, angiogenesis or proliferation[1]. Such biomarkers are produced either by the tumor itself or by other tissues and can be found in a variety of fluids, tissues and cell lines, in response to the presence of cancer or other associated conditions. MicroRNAs (miRNAs) which are small (~22bp) highly conserved non-coding RNAs endogenously expressed in every cell type, have emerged as a new type of cancer-specific biomarker[2]. They function as key regulators of gene expression by silencing target transcripts through base-pair complementation. MicroRNAs can be secreted from cells and are found in a variety of body fluids including blood, saliva, and urine, where they are quantifiable and extremely stable[1]. For these reasons, miRNAs are becoming ideal candidates as non-invasive biomarkers for cancer.

Förster resonance energy transfer (FRET)-based nucleic acid detection is one of the most promising techniques that can meet almost all the demands for a fast, simple, and multiplexed diagnostic[3]. FRET is a non-radiative energy transfer from an excited donor (FRET-donor) molecule to a ground state acceptor molecule (FRET-acceptor) through dipole-dipole interactions[4]. The principal conditions for FRET are the donor and acceptor should be in close proximity to each other and have a spectral overlap between the donor emission and the acceptor absorption. Due to their strong distance-dependence, FRET biosensors are very sensitive for analyzing biological interactions and structural changes in a nanoscale range of ca.1-20 nm. For most FRET-based nucleic acid detection assays, both donor and acceptor are conjugated with DNA, the target miRNA can complement them to change the distance between donor and acceptor, thereby changing the FRET efficiency and lifetime. MicroRNAs can be qualitatively and quantitatively detected by the change of FRET efficiency and photoluminescence (PL) intensity of donor or acceptor[5]–[9].

As the increasing application of FRET, many kinds of fluorophores have been used as FRET donor. Compared to other traditional fluorophores, luminescent terbium complex (LTC) as FRET donor has unique advantages for multiplexing detection in combination to different FRET acceptors, such as organic dyes and quantum dots (QDs)[10], [11]. Due to the forbidden intra-configurational f-f transitions in the terbium ions, LTC provides distinguished photophysical properties, like large Stokes shift, multiple narrow emission bands and extremely long excited-state lifetimes (up to the milliseconds' range) which allow for time-gated (TG) measurements[12]. The distinction between the FRET signal and short-lived auto-fluorescence background and high detection sensitivity for biological applications all benefit from time-gated measurements. The emission bands of Tb are well separated and therefore superior for spectral multiplexing; the long and distinguished decay time of the sensitized acceptors due to different FRET efficiencies provide a great potential for temporal multiplexing.

Fluorescent dyes, also known as reactive dyes or fluorophores, are non-protein molecules that absorb light and re-emit it at a longer wavelength. They have been used in biological studies for decades because they are easy to handle and less toxic. Fluorescent dyes offer higher photostability and brightness and do not require a maturation time. Fluorescent dyes are popular because of their high quantum yields, solubility, and ease of bioconjugation. The large variety and wide commercial availability of fluorescent dyes have made them the most frequently applied class of fluorophores for FRET[13], [14]. The combination of LTC donors with fluorescent dye acceptors has been used for multiplexing FRET biosensing[15], [16]. Although multiplexed LTC-to-dye FRET is possible and can provide high sensitivity, the poor separation of the absorption and emission spectrum affect spectral crosstalk between different dye acceptors in spectral multiplexing, and appropriate correction is demanded.

Regarding much narrower emission bands and size-tunable emission peaks, QDs are excellent FRET acceptor candidates for multiplexing. QDs have several unique intrinsic photophysical properties: relatively high quantum yields; the size- and material-tunable QDs can be used to give better spectral overlap with their FRET partner; 10 to 100 times higher extinction coefficient than fluorescent dyes which are extremely important for spectral overlap with the LTC emission[17], [18]. Förster distances R_0 of more than 10 nm can be achieved by LTC-to-QD FRET pairs which are significantly larger than the R_0-values for conventional D-A pairs[19], [20]. The combination of LTC and QDs for FRET has a very high potential for the use in biosensing analysis with the possibility of high sensitivity and large Förster radii.

This thesis is divided into six chapters and completed by the appendix and the bibliography. Following the background of this work, three individual studies are presented. Each chapter is corroborated with introduction, materials and methods, results and discussion, and conclusion. The first study (**Figure 1.1**) presents a temporal duplexing assay for miRNA detection using a single Tb-dye FRET pair and hybridization chain reaction (HCR). I demonstrated the implementation of time-gated FRET between terbium donors and dye acceptors into HCR for multiplexed quantification of miRNAs (miR-20a and miR-21) and their DNA analogs. HCR-TG-FRET provided washing-free nucleic acid quantification with very low limits of detection (LOD) down to 240 attomoles (1.7 pM) of miRNA and 123 attomoles (0.88 pM) of DNA. Efficient distinction from very homologous miRNAs demonstrated high target specificity. Multiplexing with a single measurement, a single excitation wavelength, and a single FRET pair allowed for simultaneous quantification of miR-20a and miR-21 at concentrations between 30 pM and 300 pM from the same sample. HCR-TG-FRET showed similar performance for serum-free and serum-containing samples without the use of RNase inhibitors. Our results present a significant improvement in current HCR approaches regarding simplicity, sensitivity, and multiplexing. The versatile diagnostic performance of HCR-TG-FRET even in challenging biological environments presents an important advantage for advanced nucleic acid biosensing.

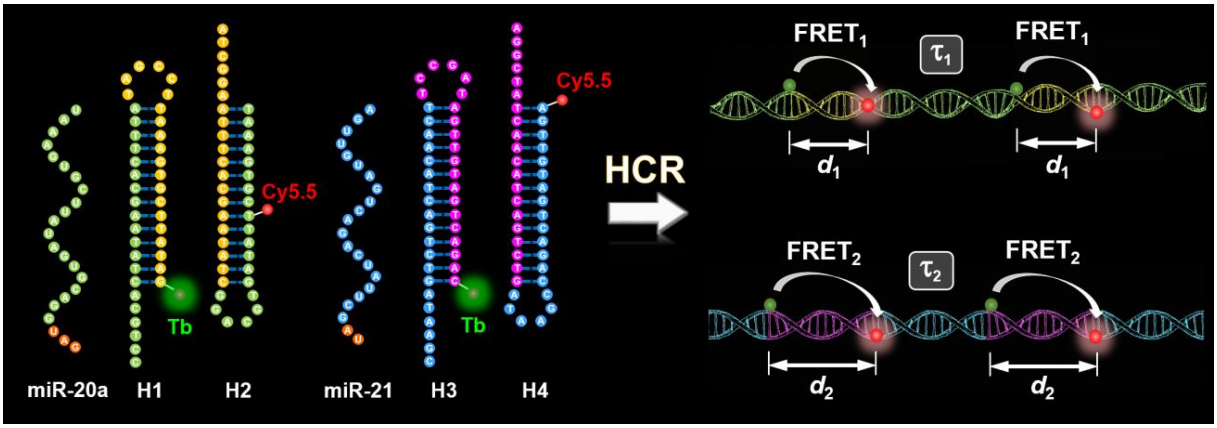

Figure 1.1. Schematic representation for duplexed (miR-20a and miR-21) detection of miRNAs using HCR-TG-FRET.

In the second study (**Figure 1.2**), I combined temporal multiplexing with spectral multiplexing, developed a quadrupling Tb-Dye FRET and rolling circle amplification (RCA) assay for single-stranded DNA (ssDNA) detection. We demonstrated time-gated FRET from a long-lifetime Tb-complex to Cy3.5 and Cy5.5 dyes for spectrotemporal multiplexing of four different DNA targets in the same sample by two time-gated windows for two different colors. We used rolling circle amplification (RCA) for high sensitivity and for placing Tb donors and dye acceptors at

controlled distances within the amplified DNA concatemers. We selected four different short ssDNAs (DNA-20a, DNA-20b, DNA-21, and DNA-191), which are the DNA-equivalents of the miRNAs hsa-mir-20a/20b/21/191, all of which have been found to be related to breast cancer. The principle of RCA-FRET is each DNA target is recognized by the terminal sequences of a specific padlock probe. After this hybridization step, a ligase closes the padlock nick over the target splint, which transfers the target into a primer for subsequent DNA synthesis. DNA amplification by RCA is performed at 37 °C for 2 h, and the resulting rolling circle product is labeled (specific hybridization) by Tb-donor and dye-acceptor DNA probes. The precise distance tuning led to target-specific PL decays of the FRET pairs and simple, separation-free, and higher-order multiplexed quantification of DNA. The RCA-FRET DNA assay could distinguish very homologous target sequences and provided limits of detection between 40 and 570 zeptomoles (0.3 to 4.1 fM) for four different DNA targets. We demonstrated the combination of the spectral and temporal dimensions of PL for higher-order multiplexing with the intensity dimension of PL for quantification of the four different DNAs at low femtomolar concentrations from the same sample, using a single excitation source and only two distinct fluorescence colors.

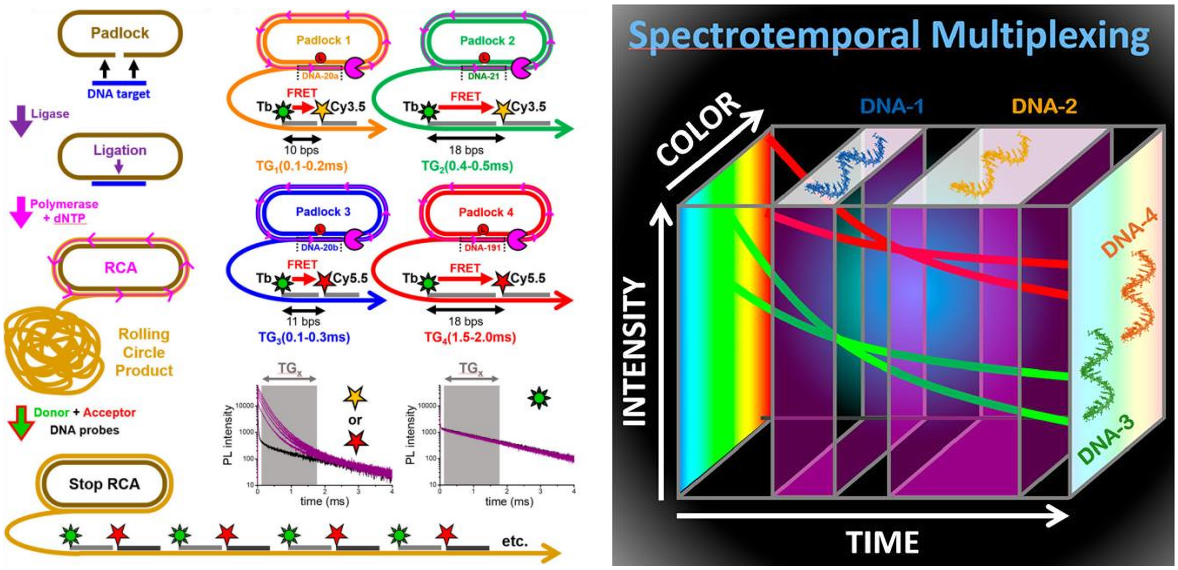

Figure 1.2. The principle of spectrotemporal quadruplexing RCA-FRET assay and PL multiplexing in three dimensions. x-axis: lifetime; y-axis: color; z-axis: intensity

In the third study (**Figure 1.3**), I investigated the Tb-to-QD temporal-multiplexing FRET by tuning the length of DNA. I analyzed 11 configurations of a 31 nt long DNA, which attached to QD by peptide-His_6 sequence (peptide-DNA), with different Tb-conjugated complementary DNA probes hybridized at distances between 0 and 26 nt by time-resolved FRET and

biomolecular modeling. Our results show that the increasing Tb-to-QD distances led to increasing FRET-sensitized lifetimes of the decay curves, all 11 configurations can be distinguished without lifetime fitting of the curves. The temporally distinct PL decays of the different DNA-FRET-configurations can be used for prototypical DNA hybridization assays. Such fine-tuning of PL decay curves via displacement of the Tb donor by only changing a few nucleotides demonstrates the high distance sensitivity of FRET and the possibility to extend nanoparticle-based temporal multiplexing.

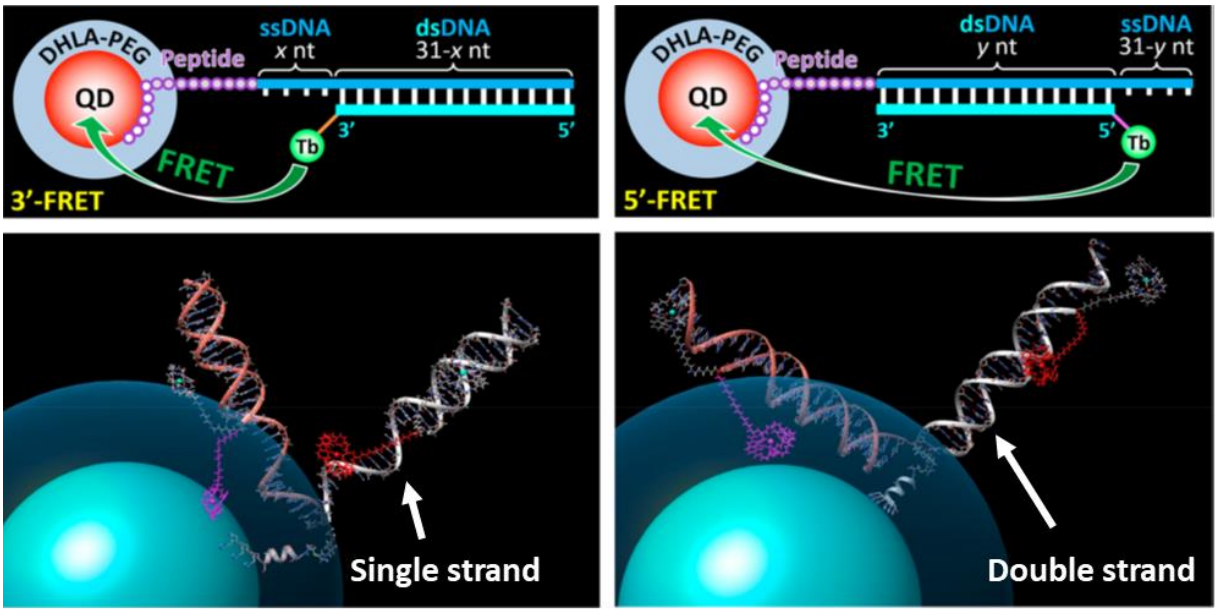

Figure 1.3. Top: Schematic representation for Tb-to-QD temporal-multiplexing FRET. **Bottom:** Biomolecular modeling was used to calculate Tb-to-QD distance ranges in parallel and vertical DNA-surface attachment configurations.

2. Background

2.1 Nucleic acid biomarkers

The term “biomarker”, short for “biological marker”, refers to an accurate and reproducible measurable indicator of some biological state or condition. In 1998, the National Institutes of Health Biomarkers Definitions Working Group defined a biomarker as “a characteristic that is objectively measured and evaluated as an indicator of normal biological processes, pathogenic processes, or pharmacologic responses to a therapeutic intervention”[21]. WHO International Programme on Chemical Safety gave an even broader definition of a biomarker as “any substance, structure, or process that can be measured in the body or its products and influence or predict the incidence of outcome or disease”[22]. Biomarkers have a range of potential clinical utilities, including identifying the presence of disease and characterizing disease subtype (diagnosis), determining disease prognosis, aiding in the selection of appropriate therapeutic doses, predicting clinical benefit or adverse response to therapy, and monitoring treatment outcomes[23]. In recent decades, promising candidate biomarkers such as proteins, metabolites, carbohydrates, steroids, lipids, peptides, nucleic acid and cells involved in different diseases such as cancer, metabolic disorders, inflammatory disorders, and diseases of nervous system and cardiovascular system have been reported[24], [25]. The focus of this work is on cancer-related nucleic acids biomarkers. The cancer diagnosis is the starting point of patient treatment, and a fast and accurate diagnosis is highly demanded.

Nucleic acids include deoxyribonucleic acid (DNA) and ribonucleic acid (RNA), which are essential for all forms of life. DNA stores genetic information and encodes the amino acid sequences of proteins responsible for cellular function. RNA plays various important roles in the coding, decoding, regulation, and expression of genes. Nucleic acids are used as important biomarkers for biological studies and medical diagnostics because sequence-specific hybridization and amplification technologies allow highly accurate and sensitive assessment of these biomarker levels over a broad dynamic range. In addition to their biological roles, nucleic acids can be used as high-affinity recognition molecules for ions, small molecules, proteins, and even whole cells[26], [27]. Nucleic acids can also be coupled with organic or inorganic materials for assembly and construction purposes[28].

2.1.1 MicroRNA biomarker

MicroRNAs are one of the most important nucleic acids biomarker group. MicroRNAs are a class of ~22 nucleotide-long non-coding RNAs that play a central role in the regulation of gene expression by translational repression or degradation of messenger RNAs (mRNAs)[2]. Biogenesis of miRNA occurs through a multi-step process requiring both a nuclear and a cytoplasmic phase (**Figure 2.1**). Firstly, miRNA genes are transcribed into primary miRNAs (pri-miRNA) with a cap and a poly-A tail by pol II or pol III[29]. Pri-miRNA is characterized by a secondary hairpin structure. Then, pri-miRNAs are processed into short 70-110 nucleotides stem-loop structures known as precursor miRNAs (pre-miRNAs) by microprocessor complex, which consists of the RNase III enzyme Drosha, and a double stranded-RNA binding protein, Di George syndrome critical region 8 gene (DGCR8)[30]. Further processing of pre-miRNAs by the RNase III enzyme Dicer generate ~22 nucleotide miRNA duplexes (ds-miRNAs). This duplex binds to the active RNA-induced silencing complex (RISC) that performs gene silencing. Argonaute 2 (AGO2) unwinds the duplex, and removes the passenger strand retaining the mature miRNA molecule[31]. The mature miRNA functional strand is loaded into the RISC complex and AGO2. RISC-AGO2 complex guides the functional strand to target the 3'UTR of the target mRNA, causing translational inhibition or promoting their degradation.

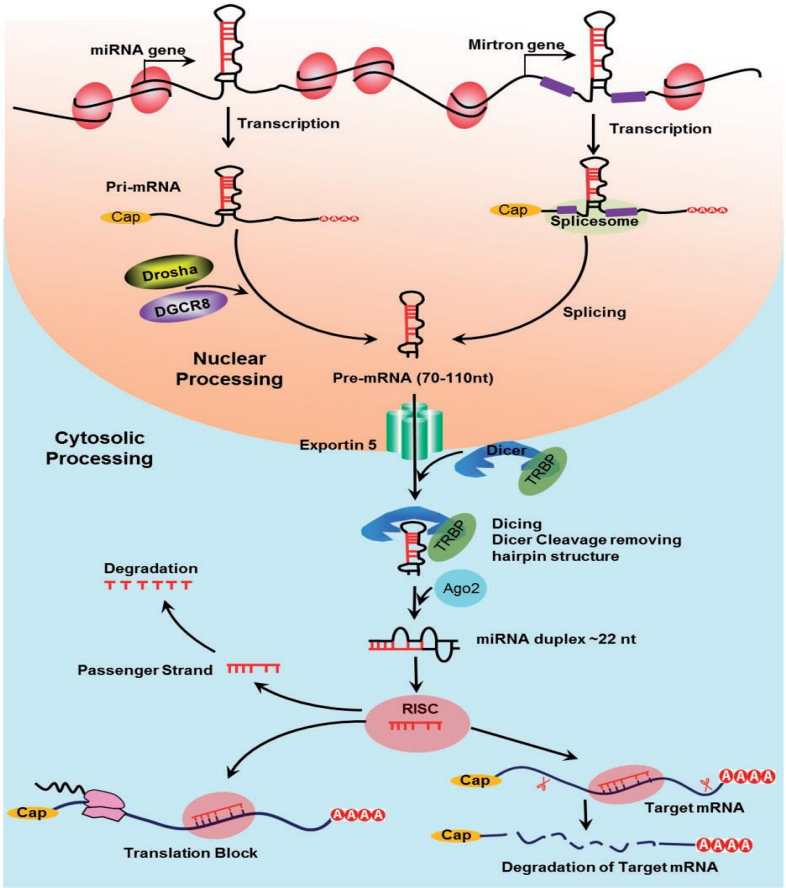

Figure 2.1. Biogenesis of microRNA: miRNA is transcribed in the nucleus as a pri-miRNA and then is micro-processed by Drosha, a class 2 ribonuclease III enzyme, and transported to the cytoplasm by exportin 5 (XPO5) where the hairpin structure is removed by Dicer and a single-stranded mature miRNA is produced, which binds to RISC and induces gene silencing. (Reference [32], copyright 2018 SAGE Journals Publishers.)

2.1.2 Cancer-associated miRNA

Cancer is one of the leading causes of death worldwide. Subsequent investigations demonstrated that almost all cancers have an alternative miRNA expression profile compared to their adjunct normal tissues. Significant progress has been made on the relationship between miRNAs and cancers. For example, miR-181-5p, miR-361-5p, and miR-320b were significantly elevated in plasma exosomes of non-small cell lung cancers (NSCLC) patients[33]. The levels of miR-16-5p, miR-21-5p, and miR-199a-5p declined in plasma and tumor tissues of triple-negative breast cancer (TNBC) patients compared with both non-TNBC and healthy individuals, as well as miR-92a-3p and miR-342-3p elevated[34].

Table 2.1 summarizes the blood-based circulating miRNA expression in the major cancer types. It clearly shows that some miRNAs are overexpressed in cancers, for example, miR-21 is highly expressed in breast cancer. In contrast, some miRNAs, for example, miR-128 is downregulated in brain cancer. More importantly, some miRNAs have different expression profile pattern in different cancer types. Like miR-103 is downregulation in breast cancer, but it is upregulation in prostate cancer. This alternative and unique expression pattern allows miRNAs to become good biomarker for early detection of cancers.

Table 2.1. Examples of the miRNA expression in the major cancer types.

Cancer type	miRNAs Expression statu	Expression status
Colon	miR-7, miR-15b, miR-17-3p, miR-18a, miR-19a, miR-19b, miR-19a-3p, miR-20a, miR-21, miR-25,miR-29a, miR-92, miR-92a, miR-92a-3p, miR-96, miR-106a, miR-106b, miR-133a, miR-139-3p, miR-143, miR-145, miR-155, miR-182, miR-183, miR-196a, miR-200c, miR-206, miR-210, miR-214, miR-221, miR-223-3p, miR-320a, miR-335, miR-372, miR-378, miR-409-3p, miR-423-5p, miR-431, miR-486, miR-720, miR-1180	Upregulated
	miR-7, miR-24, miR-26a-5p, miR-29b, miR-30b, miR-93, miR-103, miR-106a, miR-107, miR-221, miR-124, miR-127-5p, miR-138, miR-142-3p, miR-143, miR-145, miR-146a, miR-151-5p, miR-191, miR-194, miR-199-3p, miR-218, miR-222, miR-320a, miR-375, miR-382, miR-409-3p, miR-422a, miR-423-3p, miR-423-5p, miR-601, miR-652, miR-760, let-7d	Downregulated
Breast	miR-16, miR-19b, miR-21, miR-22a, miR-25, miR-29c, miR-92a, miR-96-5p, miR-127-3p, miR-133a, miR-145, miR-148a, miR-148b, miR-155, miR-199a, miR-222, miR-324-3p, miR-376a, miR-376c, miR-382, miR-409-3p, miR-424, miR-505-5p, miR-652, miR-801,	Upregulated
	miR-103, miR-107, miR-195, miR-205, miR-200c, miR-451, let-7d, let-7i	Downregulated
Prostate	miR-16, miR-21, miR-34b, miR-92a, miR-92b, miR-103, miR-107, miR-130b, miR-141, miR-145, miR-155, miR-197, miR-200a, miR-200c, miR-210, miR-221, miR-301a, miR-326, miR-328, miR-331-3p, miR-375, miR-432, miR-485-3p, miR-486-5p, miR-501-3p, miR-551b, miR-562, miR-574-3p, miR-622, miRr-625*, miR-636, miR-640, miR-766, miR-885-5p, miR-1285, miR-2110	Upregulated
	miR-30, miR-181a-2, let-7a, Let-7c, let-7e	Downregulated
NSCLC	miR-15b-5p, miR-22, miR-26b, miR-28, miR-34b, miR-125a-5p, miR-125b, miR-145, miR-146a, miR-191, miR-200b, miR-200c, miR-203, miR-205, miR-340, miR-425, miR-429, miR-590-3p, miR-766, miR-944, miR-3662	Upregulated
	miR-15, miR-16, miR-16-5p, miR-17b-5p, miR-19-3p, miR-20, miR-20a-5p, miR-25, miR-28, miR-34b, miR-92-3p, miR-148a, miR-148b, miR-152, miR-193a-5p, miR-203, miR-218, miR-323-3p, miR-450b-5p, miR-485-3p, miR-566, miR-642, miR-661, miR-1290, let-7c	Downregulated
Melanoma	miR-210, miR-211	Upregulated
	miR-29c, miR-324-3p, miR-509-3p, miR-509-5p, miR-4706, miR-4731	Downregulated
Bladder	miR-26b-5p, miR-144-5p, miR-148b-3p, miR-152, miR-205, miR-374-5p, miR-663b	Upregulated
	miR-15b-5p, miR-27a-3p, miR-30a-5p, miR-92a, miR-100, miR-143, miR-497, miR-3187-3p	Downregulated
Brain	miR-15b, miR-20a, miR-21, miR-106a, miR-128, miR-181b, miR-210, miR-220, miR-221	Upregulated
	miR-29, miR-125b, miR-128, miR-342-3p, miR-497	Downregulated
Pancreas	miR-10b, miR-16, miR-17-5p, miR-18a, miR-20a, miR-21, miR-22-3p, miR-24, miR-25, miR-26b, miR-27a-3p, miR-30c, miR-99a, miR-106b, miR-134, miR-146a, miR-150, miR-155, miR-181a, miR-181b, miR-182, miR-185, miR-191, miR-192, miR-194, miR-196a, miR-196b, miR-210, miR-212, miR-221, miR-375, miR-378, miR-484, miR-486-5p, miR-628-3p, miR-636, miR-642b, miR-885-5p, miR-938, miR-1290, miR-1825, miR-6075, miR-6836-3p	Upregulated
	miR-26b-3p, miR-34a, miR-106b-3p, miR-122, miR-125a-3p, miR-126*, miR-145, miR-223, miR-492, miR-505, miR-663a, miR-885-5p, miR-4294, miR-4476, miR-4530, miR-6799-5p, miR-6880-5p	Downregulated

*(Reference [35], copyright 2018 Elsevier Publisher.)

2.1.3 MicroRNA detection methods

Detection of miRNA expression can help to identify miRNAs that regulate a range of vital processes and discover miRNA based biomarkers for diverse molecular diagnostic applications in cancer. Traditional strategies for detection of miRNA, including northern blotting, microarrays, and quantitative RT-PCR (qRT-PCR), have their relative strengths and weaknesses. Northern blotting is complex and requires radiolabeling, which can introduce significant contamination and has a low detection efficiency. Microarray is less expensive but does not have a lower sensitivity and dynamic range, therefore, it is often used as screening tool rather than as quantitative assay platform. qRT-PCR has the widest dynamic range and highest

accuracy and is the only method that can easily provide absolute miRNA quantification, however, it suffers from throughput issues. Except for these conventional detection methods, over the past decade, various methods have been implemented for sensitive, selective and high-throughput detection of miRNAs, such as nanoparticle-derived probes, isothermal amplification, electrochemical methods, optical methods and other emerging technologies as summarized in **Figure 2.2**.

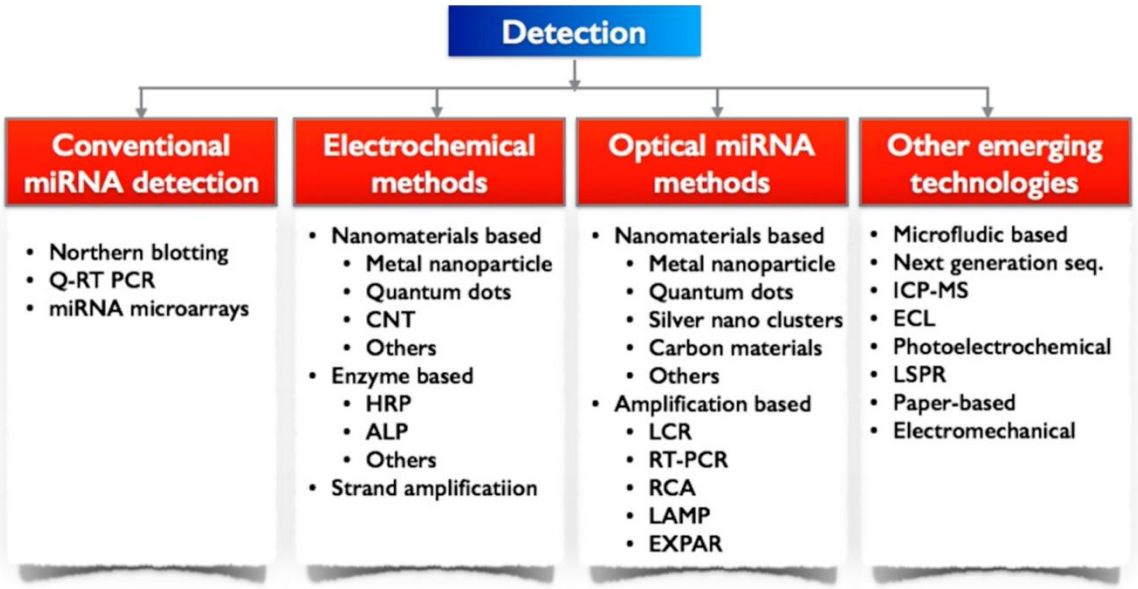

Figure 2.2. Detection methods of miRNA. (Reference [36], copyright 2018 Elsevier Publisher.)

2.2 Förster resonance energy transfer

Förster resonance energy transfer is a well-established photophysical phenomenon of non-radiative resonance energy transfer of excitation energy (not electron) from an excited donor fluorophore to a proximal ground-state acceptor. It was first established theoretically in 1948 and was named after the German scientist Theodor Förster. FRET is analogous to near-field communication, in that the radius of interaction is much smaller than the wavelength of light emitted. In the near-field region, the excited chromophore emits a virtual photon that is instantly absorbed by a receiving chromophore. These virtual photons are undetectable since their existence violates the conservation of energy and momentum, and hence FRET is known as a radiationless mechanism[37]. The principal conditions for FRET are: (i) the energy of the electronically excited state of donor must be higher than the possible energy level of acceptor; (ii) there should be a spectral overlap between the donor emission and the acceptor absorption; (iii) the donor and acceptor should be in close proximity to each other (ca. 1-20 nm). The

applications of FRET have expanded tremendously in the last 30 years, and the technique has become a staple technique in many biological and biophysical fields. FRET is a highly distance-dependent phenomenon and can be used as molecular ruler[38] to measure the distance between two positions of interest on a biological molecule by attaching appropriate donor-acceptor groups. If the molecule only involves one donor and one acceptor group, the distance between the donor and the acceptor can be measured when there is no conformational change. When the molecule has a big conformational change, FRET can also measure the dynamical activities between two sites on the molecule, such as protein interactions[39], [40]. FRET is widely applied in many other fields such as single-molecule experiments, biosensors and DNA mechanical movements[41]–[44]. This chapter provides the required theoretical background for successful use of FRET in biological applications.

2.2.1 FRET theory

FRET is understood as a non-radiative transfer through dipole-dipole interactions that allows electronic energy to be transferred from an excited donor D to a ground-state acceptor A[45], [46]. The donor and acceptor molecule can be seen as a group of coupled electrical oscillators. Donor oscillators will oscillate and generate their own electromagnetic field. Energy transfer only occurs when the acceptor oscillators are sensitive to the donor oscillators' electromagnetic field and "share" electronic transitions, which enable the excitation of the molecule from its ground state to the excited state. These electronic transitions are presented in a simplified Jablonski diagram in **Figure 2.3** (left) showing the basic principle of FRET. The donor is brought to an excited state (D*) from an electronic ground state (D) by light excitation ($h\nu$), followed by inner relaxation (dotted arrows) to an excited electronic ground state and finally to the ground state by radiative decay (k_D), non-radiative decay ($k_{D\text{-}NR}$) or FRET (k_{FRET}, dashed lines referring to possible resonant transitions). FRET (horizontal lines with dots on each end) occurs when the energy transitions of D* and A are in energetic resonance. After FRET, the acceptor is in an excited state (A*), followed by radiative decay (k_A) and non-radiative decay ($k_{A\text{-}NR}$) to its ground state. In spectroscopic terms, there should be a spectral overlap between the donor emission and the acceptor absorption spectra (**Figure 2.3** right). So choosing a suitable FRET pair is the first step for successful FRET, as shown in **Figure 2.4**, there are many different fluorescent materials can be excellent FRET donor and acceptor. The selection of a correct FRET pair depends on the actual biological question to be investigated, the type of biological specimen, the available instrumentation and the technique applied to measure FRET. Various fluorescent proteins, organic dyes with improved photostability and excellent spectral

characteristics as well as quantum dots have been developed and used as FRET donor and acceptor.

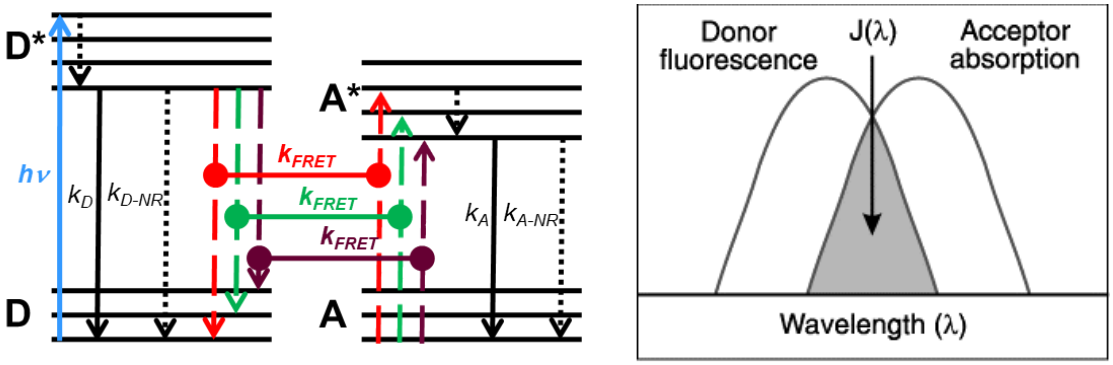

Figure 2.3. (Left) Simplified Jablonski diagram representing the energy levels of the donor (D) and acceptor (A) molecules. (Right) Spectral overlap between the donor emission and the acceptor absorption.

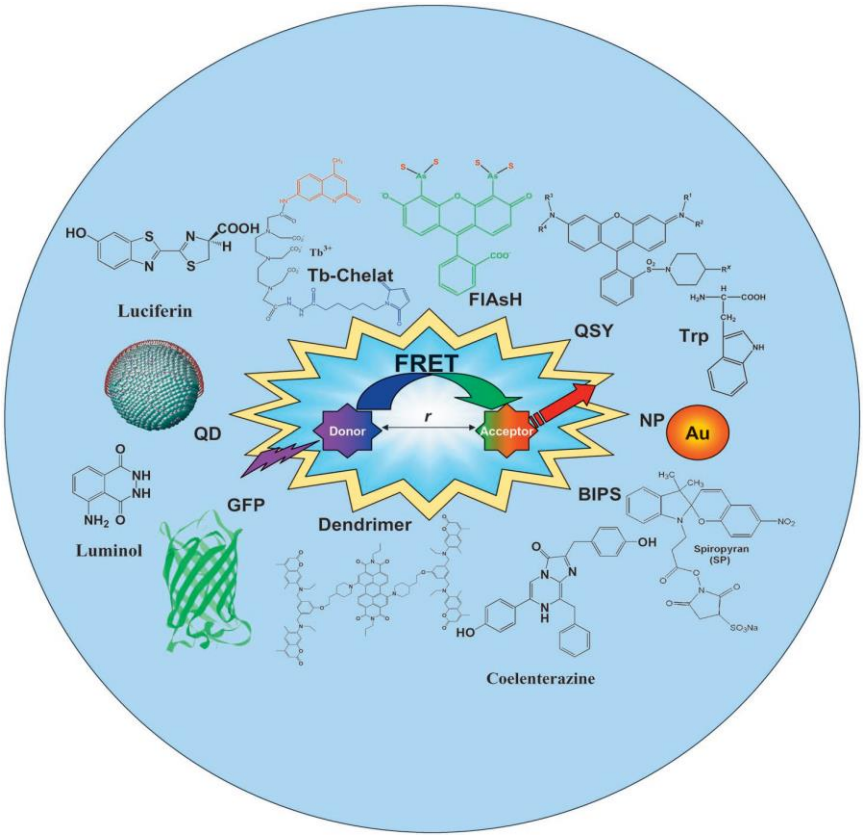

Figure 2.4. Examples of available FRET donor and acceptor candidates. (Reference [14], copyright 2006 Wiley-VCH Publisher.)

FRET theory depends on the distance between the donor and the acceptor, the spectral overlap and their relative orientations, it can be summed up in below equations[47].

The rate of energy transfer is traditionally described as:

$$k_{FRET} = \frac{1}{\tau_D}\left(\frac{R_0}{r}\right)^6 \tag{2.1}$$

where τ_D is the excited-state lifetime of the donor in absence of the acceptor; R_0 is the Förster distance representing a transfer efficiency of 50 %; r is the donor-to-acceptor distance (**Figure 2.5**).

Then, the FRET efficiency is

$$\eta_{FRET} = \frac{k_{FRET}}{k_{FRET}+\tau_D{}^{-1}} = \frac{{R_0}^6}{{R_0}^6+r^6} \tag{2.2}$$

The Förster distance R_0 can be calculated by the spectral overlap integral between the emission spectrum of the donor and the absorption spectrum of the acceptor:

$$R_0 = \left(\frac{9(\ln 10)\kappa^2\Phi_D}{128\pi^5 N_A n^4} J(\lambda)\right)^{1/6} \tag{2.3}$$

where N_A is Avogadro's number (6.023×10^{23} mol^{-1}); n is the refractive index of the medium; κ^2 is the orientation factor of the coupled donor and acceptor transition dipole moments which is usually taken as 2/3; Φ_D is the quantum yield of the donor; $J(\lambda)$ is the spectral overlap between the donor emission and acceptor absorption. A FRET pair with a large R_0 value is generally favored, because of increased likelihood of FRET occurrence. For a given FRET-pair, the larger spectral overlap results in larger Förster distance.

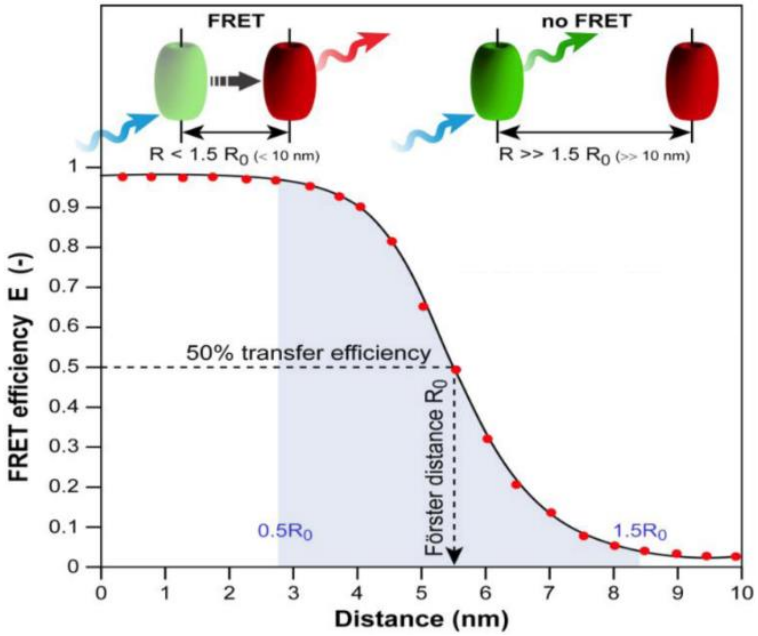

Figure 2.5. FRET efficiency η_{FRET} variation as a function of the donor-acceptor distance (r) shows the sixth power dependency and a measurable range of the FRET efficiency between 0.5 R_0 and 2.0 R_0 with a steep curve around R_0. (Reference [48], copyright 2012 MDPI Publisher)

To enhance the FRET efficiency, the donor group should have good abilities to absorb photons and emit photons. That means the donor group should have a high extinction coefficient and a high quantum yield. The overlap of the emission spectrum of the donor and absorption spectrum of the acceptor means that the energy lost from the excited donor to the ground state could excite the acceptor group. The energy matching is called the resonance phenomenon. Thus, the more overlap of spectra, the better a donor can transfer energy to the acceptor. The spectral overlap can be described as:

$$J = \int \bar{I_D}\,(\lambda)\varepsilon_A(\lambda)\lambda^4 d\lambda \tag{2.4}$$

Where $\varepsilon_A(\lambda)$ is the acceptor extinction coefficient, $\bar{I_D}(\lambda)$ is the donor emission spectrum normalized to unity and is given by:

$$\int \bar{I_D}\,(\lambda)d\lambda=1 \tag{2.5}$$

In addition, the Förster distance strongly depends on the orientation factor κ^2:

$$\kappa^2 = (\cos\theta_R - 3\cos\theta_D \cos\theta_A)^2 \tag{2.6}$$

where θ_{R} is the angle between the donor and acceptor transition dipole moments, θ_D and θ_A are the angles between the respective dipole moments and the line connecting the donor and the acceptor.

Orientation factor κ^2 is in the range 0 to 4. 0 corresponds to a perpendicular orientation between the donor and acceptor transition dipoles, 1 is parallel and 4 a collinear orientation (**Figure 2.6**). In cases when the rotational reorientation of the chromophores is faster compared to the donor excited state lifetime, κ^2 averages to a value of 2/3. Since the sixth root is taken to calculate the distance, variation of κ^2 does usually not result in major errors in the calculated distances except when κ^2 is close to 0. In most biological FRET experiments, the orientation factor is assumed to be 2/3, which simplifies the application of FRET significantly.

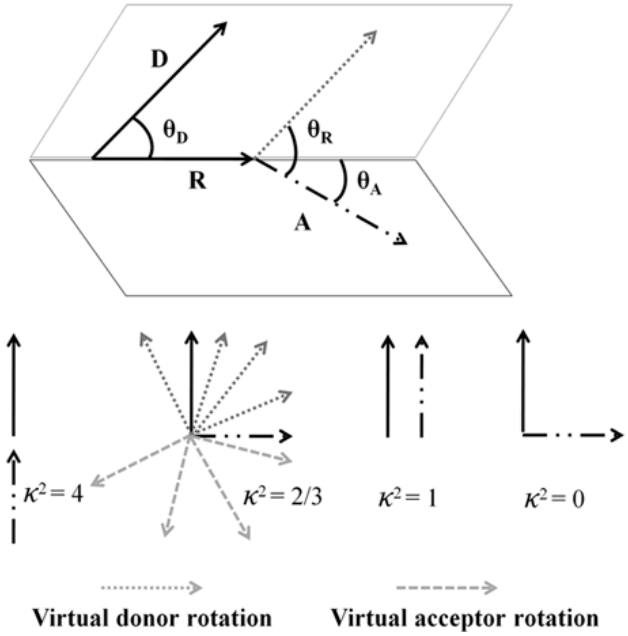

Figure 2.6. The orientation of emission dipole moment of donor and absorption dipole moment of acceptor. (Reference [49], copyright 2015 MDPI Publisher)

2.2.2 FRET applications

The major constituents of all living beings are nano-sized molecular species like lipids, proteins, carbohydrates, and nucleic acids. These molecules are constantly in communication with each other through complex yet specific interactions in a crowded molecular environment, regulating the biological functions in an organism.[50], [51]. Due to the biological nanometer working distance and the high sensitivity for small distance changes, FRET has been widely applied in the study of structure elucidation, cellular processes, and diagnostics. The occurrences of the binding, diffusion, and mobility of molecular structures in situ are easily investigated under the spatial and temporal resolution of FRET[52]. Combined with microscopy and spectroscopy, FRET imaging allows scientists to study a variety of phenomena that produce changes in molecular proximity, thereby leading to many significant findings in the life sciences. FRET imaging is a powerful tool in life-science research[52]–[55]. Unlike the usual two molecule studies, FRET measurements have been made between single-molecules by labeling fluorophores to two different sites of the same molecule (i.e. single-molecule FRET; sm-FRET) to investigate the intra activities of the molecule[56]–[59]. FRET is increasingly being used in the area of "sensing/recognition" molecules as a simple, rapid, and sensitive transduction mechanism[60], [61]. Nearly every target of interest, like cancer markers, pathogen markers, microbes, cells, nucleic acids, toxins, drugs, can be sensed using FRET by exploiting the wide

field of recognition molecules, such as small organic molecules, polymers, carbohydrates, antibodies, proteins and peptides, nucleic acids and aptamers[60], [62]. Most sensing techniques are based on the binding or cleavage of donor and acceptor in the presence of the target, which can be measured mainly by changes of the donor/acceptor emission intensity. One of the main targets of interest which FRET has played a significant role in clinical analysis is nucleic acid testing.

2.2.3 FRET for nucleic acid detection

FRET has a significant impact on molecular diagnostic technologies for detecting specific, relatively short DNA or RNA sequences (typically identified during DNA sequencing) for infectious disease diagnosis, genotyping, and pharmacogenomics[63]–[65]. These technologies rely on the detection of target nucleic acid hybridization and/or amplification. Real-time, homogeneous, and high-throughput FRET-based technologies are desired. The hybridization reaction is one of the most important and sensitive tools in FRET-based nucleic acid assay (**Figure 2.7A**). It is real-time observation directly in solution, as a homogenous type without washing procedures. The high speed of hybridization in solution and the detection of only the hybridized probe signal makes it possible to perform in vivo hybridizations directly in live cells. Multiple formats of FRET hybridization probes have been developed[66]. Molecular beacon is one of the latest developments in the area of hybridizing DNA FRET (**Figure 2.7B**). Molecular beacons are designed as hairpin-shaped oligonucleotides. The double-stranded stem carries the donor and acceptor dyes. The loop fragment can hybridize to the target nucleic acid sequence. When the probe is not hybridized to the target, the donor and acceptor are brought in close proximity by the stem formation, resulting in the FRET-based quenching of the donor. However, in the presence of the target sequence, the FRET transfer is disrupted by the probe, which forms longer and stronger hybrids with the target. Additionally, FRET-based nucleic acid amplification technology has emerged from the marriage between polymerase chain reaction (PCR) and real-time monitoring of fluorescent chemistry. The TaqMan method was developed to allow the real-time monitoring of the reaction. The principle (**Figure 2.7C**) depends on a DNA-based probe with a fluorescent reporter at one end and a quencher of fluorescence at the opposite end of the probe. The close proximity of the reporter to the quencher prevents the emission of its fluorescence; hydroxylation of the probe by the 5' to 3' exonuclease activity of the Taq polymerase releases the reporter and thus allows emission of fluorescence. Therefore, an increase in the product targeted by the reporter probe at each PCR cycle causes a proportional

increase of fluorescence. Fluorescence is detected and measured in a real-time PCR machine[67].

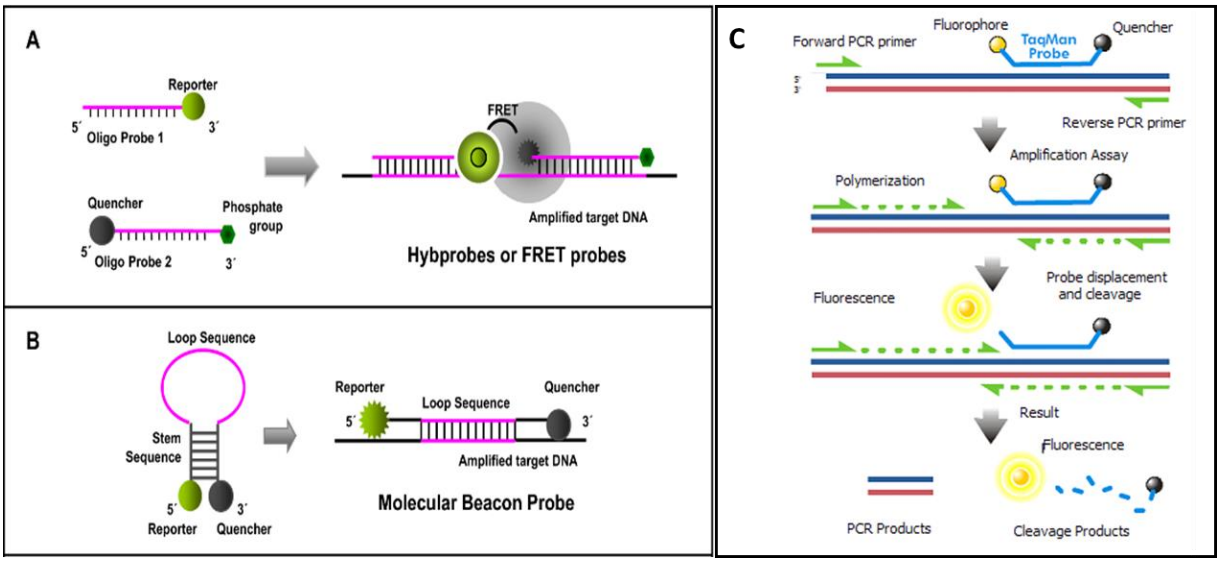

Figure 2.7. Designs of FRET probes for hybridization detection and TaqMan qPCR. (Reference [68], copyright 2015 Elsevier Publisher and Wikipedia)

2.3 Lanthanides

2.3.1. Introduction

Lanthanides are one of the cornerstones of our modern technology. They play a major role in lighting industry[69], electroluminescent materials, telecommunication[70], biological assays[71] and medical imaging purposes[72], [73]. Their growing importance in biological and medical research has been highlighted in a number of recent reviews[74]–[78]. This versatile utilization of lanthanides is due to their unique electrical, optical and magnetic properties, which will be discussed in this chapter.

According to the International Union of Pure and Applied Chemistry (IUPAC) recommendations (1968), lanthanides (Ln) include elements lanthanum (La) and 14 other elements (Ce, Pr, Nd, Pm, Sm, Eu, Gd, Tb, Dy, Ho, Er, Tm, Yb, and Lu) which are listed separately at the bottom of the periodic table. They are called lanthanides because the elements in the series are chemically similar to lanthanum. These fifteen lanthanides, along with similar chemical behavior scandium and yttrium, are often collectively known as rare-earth elements. Their similar chemical properties are due to the electronic configuration of the lanthanide atoms and their corresponding ions. The general electronic configuration of lanthanide atoms are usually denoted as $[Xe]4f^n5d^m6s^2$, where [Xe] represents the electronic configuration of the

noble gas xenon, n represents the number of electrons from 0 to 14, and m represents the number of electrons 0 or 1. Xenon has an electronic configuration of $1s^2$ $2s^2$ $2p^6$ $3s^2$ $3p^6$ $4s^2$ $3d^{10}$ $4p^6$ $5s^2$ $4d^{10}$ $5p^6$ and is abbreviated as [Xe]. The lowest energy orbitals are filled first with electrons and orbital energy follow the sequence:

1s<2s<2p<3s<3p<4s<3d<4p<5s<4d<5p<6s<4f<5d<6p<7s<5f<6d<7p<8s

Depending on the relative energy levels, lanthanum, cerium, gadolinium, and lutetium belong to the electronic configuration type [Xe]$4f^n6s^2$, and the rest of the lanthanides to the type [Xe] $4f^n5d^16s^2$ (for terbium both configurations are energetically close to each other, so either one may be adopted). The 4f orbitals have low radial expansion, and they are shielded from the surroundings by the filled energetically lower 5s and 5p sub-shells which results in very weak perturbations of the spectroscopic and magnetic properties of Ln ions by the surrounding microenvironment. Additionally, this shielding effect causes the interaction between Ln ions (the Ln ion being the central ion) with ligands to form complexes to be electrostatic in nature rather than covalent.

2.3.2. Luminescence lanthanide complexes

Most of the trivalent lanthanide ions are luminescent. The luminescence intensity of the lanthanide ion is dependent on the quantum yield, which is related to the ratio of radiative and nonradiative relaxation processes of the excited energy levels. The quantum yield is also related to the extent of the energy gap between the lowest excited energy level of the ion and the highest sublevel of its ground state multiplet [79]. The partial energy level diagram for aqueous lanthanide ions, illustrating also the energy gaps, is presented in **Figure 2.8**. Judged by the energy gap criterion, Eu^{3+}, Tb^{3+}, and Gd^{3+} ions have the strongest luminescence. The most commonly used lanthanide ions in bioanalytical applications are Eu^{3+} and Tb^{3+}. In addition to their intense emission in the visible wavelengths, their particularly long lifetime is a very important reason[80].

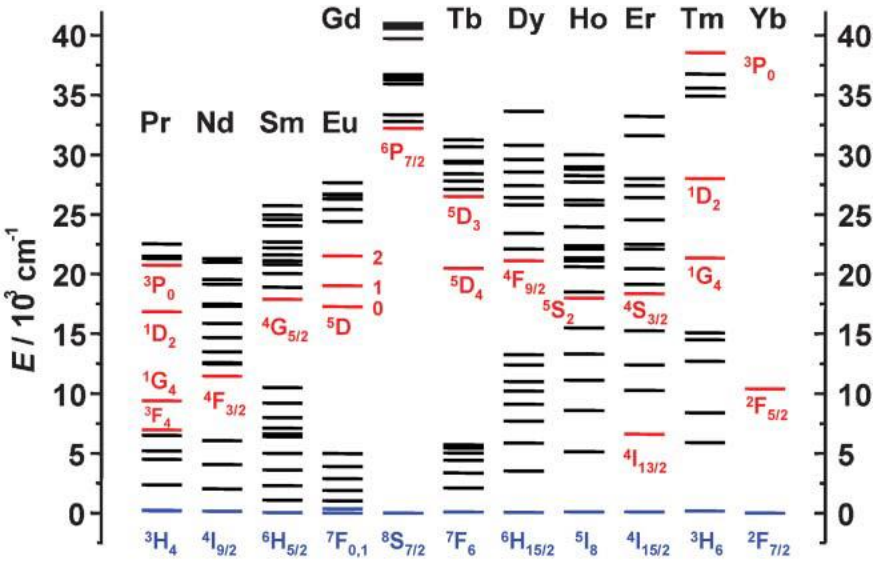

Figure 2.8. Partial energy diagrams for the lanthanide aquo ions. The main luminescent levels are drawn in red, while the fundamental level is indicated in blue. (Reference [79], copyright 2005 RSC Publisher.)

The most common oxidation state of lanthanide ions in aqueous solvents is Ln^{3+}. The trivalent lanthanide ions may be implied in three types of electronic transitions:

(1) Charge transfer transition: Both ligand-to-metal and metal-to-ligand transitions are allowed by Laporte's selection rule. Their energy is usually very large so that they appear in the UV[81].

(2) 4f-5d transitions: They correspond to the promotion of a 4f electron into the 5d sub-shell are also allowed by the parity rule, resulting in sizable oscillator strengths with absorption coefficients in the range 10^2-10^3 $M^{-1}cm^{-1}$, that is, comparable to those of the charge transfer transitions. Their energy depends largely upon the metal environment because 5d orbitals are external and they interact directly with ligand orbitals; however, these transitions are also quite energetic[82].

(3) f-f transitions: The very low level of direct excitation of the lanthanide ions as well as their extremely long excited state lifetimes come from the Laporte's selection rule and spin-multiplicity rule. Most of the transitions of the Ln^{3+} ions involve redistribution of electrons within the 4f sub-shell, but f-f transitions are parity-forbidden[83]. That explains their faint intensities and very low molar extinction coefficients (<1 $M^{-1}cm^{-1}$)[84].

To get more excited, lanthanide ions usually require indirect excitation from a sensitizing structure, which can be an organic ligand containing a light absorbing chromophore structure and a moiety that coordinates the central ion, or an inorganic crystal structure containing a sensitizer. The absorption can be promoted by operators linked to the nature of light, the odd-parity electric dipole (ED) operator, the even-parity magnetic dipole (MD) and electric

quadrupole (EQ) operators. Laporte's parity selection rule states that levels with the same parity cannot be connected by electric dipole transitions, therefore, f-f transitions are forbidden by the ED mechanism. However, under the influence of a ligand-field, non-centrosymmetric interactions result in the mixing of electronic states of opposite parity, which somewhat relaxes the selection rule and the transitions become partially allowed. Together with the parity-allowed magnetic dipole transitions, the lanthanide ions are greatly sensitized in a three-step mechanism. Light is first absorbed by the immediate surrounding of the lanthanide, then energy is transferred to the Ln ion and then the Ln ion emits light. The overall process is quite complex and involves several mechanisms and energy levels. When sensitized by an inorganic matrix or an organic ligand, the molar absorption coefficients can be compared with that of organic fluorophores and they can emit multiple, characteristic narrow emission bands. The specific, narrow lanthanide emission bands are a result of the sharp transitions between the well-defined J-levels (be degenerated from the electronic configuration based on Coulomb interaction and spin-orbit coupling) of lanthanide ions due to the shielding of the 4f orbitals by the filled $5p^6 6s^2$ sub-shells. The J-levels can be further split into sublevels (which can be seen as the fine structure of the main emission bands of the lanthanide ion) if the lanthanide ions are in a coordinating environment[85]. Eu^{3+} ion is taken as an example in **Figure 2.9**.

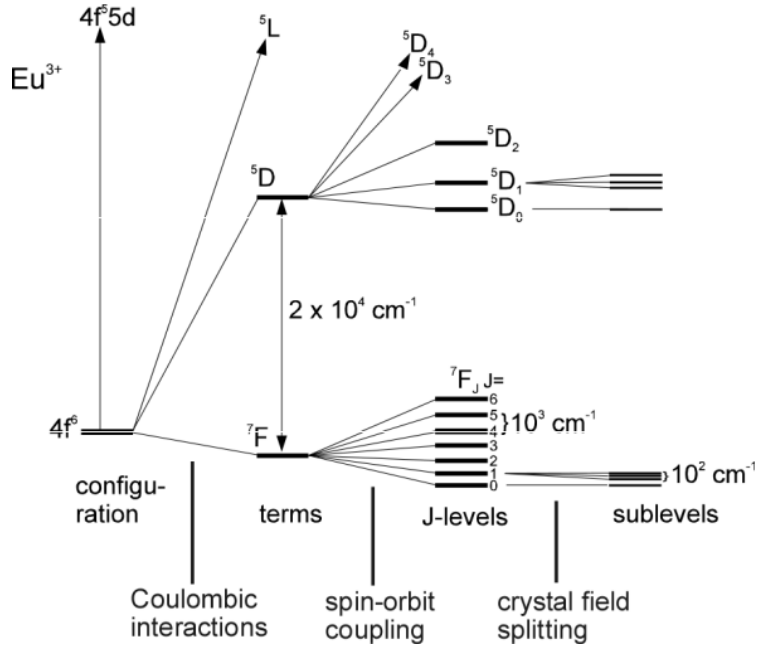

Figure 2.9. The interactions lead to the different electronic energy levels for the [Xe] $4f^6\ 5d^0$ configuration of Eu^{3+}. (Reference [85], copyright 2005 Science Reviews 2000 Ltd.)

Luminescent lanthanide complexes offer several distinct advantages. First, their sensitized emission gives rise to a large Stokes shift between the absorption of the antenna and the emission of the lanthanide, thus avoiding concentration-dependent self-absorption problems (**Figure 2.10a**). Second, their emission spectra are characterized by very narrow bands (ca. 20 nm wide), therefore, lanthanide probes can be concurrently employed to monitor several analytes simultaneously (**Figure 2.10b**). Lastly, lanthanide emissions are Laporte forbidden and therefore are characterized by extremely long luminescence lifetimes, in the millisecond range for europium and terbium and the microsecond range for samarium and dysprosium[12], [79]. In comparison, the lifetimes of most organic dyes are in the nanosecond range, whereas those of biological media are typically in the sub-microsecond range. The very long luminescence lifetime is ideal for the direct, time-gated detection of analytes in a complex biological medium. The time gate allows no auto-luminescence interference before measuring the luminescence of the complex (**Figure 2.10c**). For a high luminescent lanthanide complex, introducing a suitable light-harvesting chromophore or ‘‘antenna” is essential. The function of this antenna is to absorb energy from UV-Vis radiation and transfer it to the Ln^{3+} ion, then result in the high luminescence of lanthanide complex which can reach to 10^4-10^5 $M^{-1}cm^{-1}$, being essentially determined by the molar absorption coefficients of the surrounding ligands (**Figure 2.10d, e**). This effective way to sensitize the Ln^{3+} ion is the so-called ‘‘antenna effect”. The commonly used antenna molecules are organic ligands bearing aromatic chromophores, such as bipyridine, terpyridine, triphenylene, quinoline, or substituted phenyl and naphthyl groups.

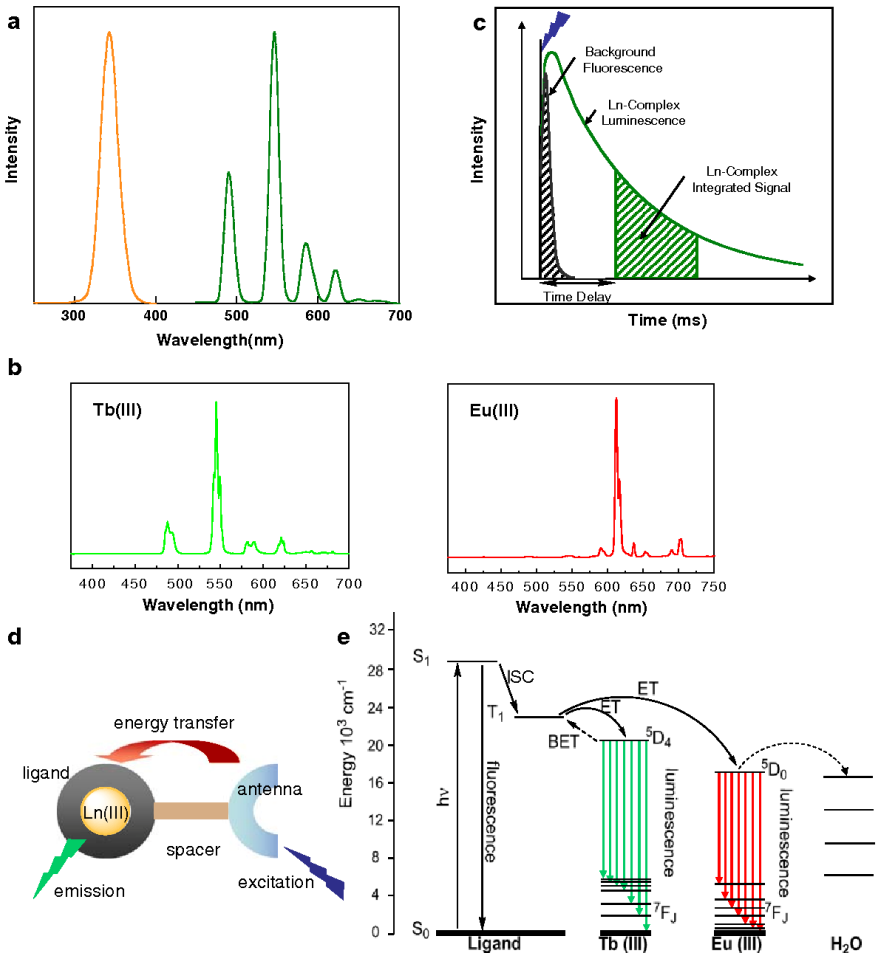

Figure 2.10. Principles of lanthanide luminescence. a) Stokes shift between the absorption of an antenna (orange) and the emission of terbium (green). b) Emission of terbium and europium. c) principle of time-gated spectroscopy. d) Indirect excitation of a lanthanide via an antenna. e) Simplified Jablonski diagram showing the main energy flow paths during sensitization of lanthanide luminescence via its antenna. (Reference [86], copyright 2009 Springer Publisher.)

2.3.3. Lanthanide complex applications

Luminescent lanthanide complexes play a crucial role in biological applications, such as probes for diagnostics, and bioconjugates for medical imaging and the photodynamic treatment of cancer[87], [88]. They are widely used in Magnetic Resonance Imaging for diagnostic purposes or for monitoring the effects of therapy, usually applied for patients with cancers, cardiovascular problems, central nervous system, and other conditions[89], [90]. Moreover, lanthanide complexes are good factors for luminescence imaging because of their emission in the near-infrared region (NIR) which can be used to study the biological structures at different depths and resolutions with the accuracy of analysis[91]. Lanthanide complexes offer several advantages over conventional organic fluorophores in bioanalysis due to their unique

spectroscopic properties, such as large Stokes shifts, long luminescence lifetimes, and narrow emission bands. The large Stokes shifts contribute to the low background signal since there is minimal crosstalk between excitation and emission signals. The long-lived luminescence of lanthanide complex can be collected using time-resolved fluorescence measurement, while the interference of short-lived background fluorescence can be eliminated. Furthermore, narrow emission can improve the detection sensitivity of luminescent probes for analytes, hence, lanthanide-based luminescent probes have favorable signal-to-noise ratios and could serve as sensitive probes for various targets. Some of them have been successfully commercialized within detection systems for immunoassays and DNA assays based on luminescent Tb^{3+} or Eu^{3+} complexes to detect various clinical biomarkers in biomedical diagnostics and imaging[11], [92]. The conjugation of lanthanide complexes to biomolecules can be established by covalently bound functional groups on the ligand. The most popular conjugation strategies are using Ln-complexes functionalized with NHS-esters or maleimide groups, which selectively bind to amino or thiol groups, respectively.

Multiplexing

Multiplexing has stimulated the renewed interest because it can save time and reagents, increasing demand for the simultaneous measurement of multiple biological parameters (e.g., concentrations or distances) in a single sample. The most frequently used technique to detect multiple parameters from the same sample is spectral (or color) multiplexing with different fluorophores, such as organic dyes[93], [94], fluorescent proteins[95] and quantum dots[96]. Luminescent lanthanide complex-based FRET is a valuable tool for sensitive and versatile multiplexing. In preference to other lanthanide complexes, luminescent Tb complexes have been the major players in this field because of their large quantum yields, extremely long lifetime and multiple emission bands.

In recent years, different multiplexed LTC-based FRET biosensors have been developed, most of them use the principle of FRET from one LTC donor to different acceptor molecules or particles (spectral multiplexing)[8], [97]. As shown in **Figure 2.11**, the multiplexing capacity of LTC donor is due to the narrow and well-separated emission bands, where we can put several different acceptors in between or beyond the LTC emission bands.

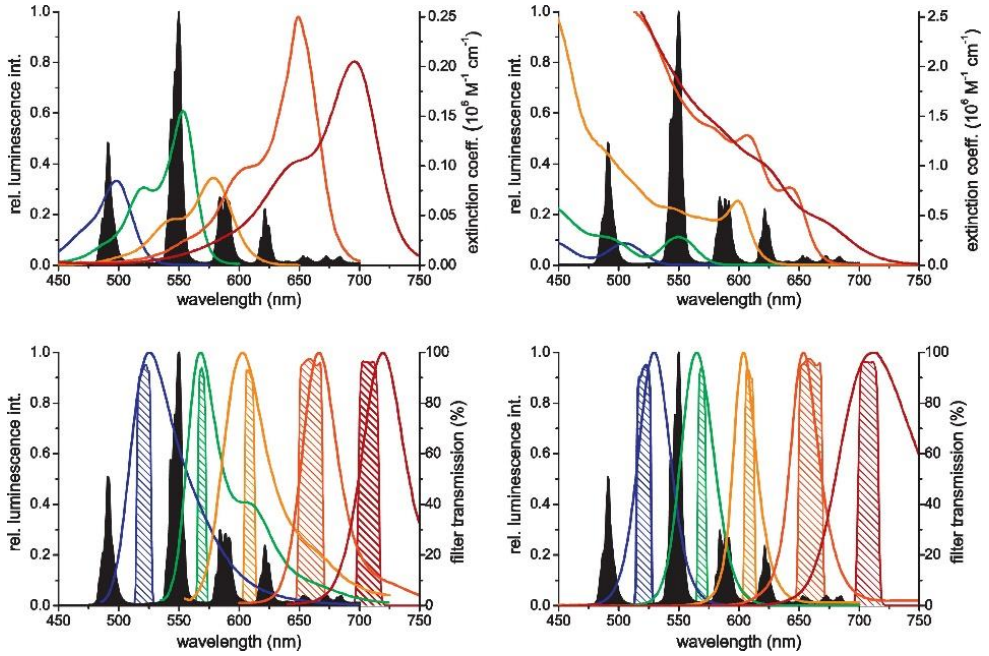

Figure 2.11. LTC-donor-based multiplexed FRET. **Top:** Broad spectral overlap between LTC emission and the absorption of several different acceptors (Left: organic dyes; Right: QDs). **Bottom:** Separation of the single Tb emission bands allows the measurement of different acceptors in wavelength ranges with very low Tb intensity. Left: organic dyes, Oregon Green(blue), Alexa Fluor555 (green), Alexa Fluor568 (orange), Cy5 (red) and Alexa Fluor700 (brown); right: QDs, Qdot525 (blue), Qdot565 (green), Qdot605 (orange), Qdot655 (red) and QDot705 (brown), LTC-PL-spectra in black. (Reference [10], copyright 2014 Elsevier Publisher.)

The number of spectral multiplexing is still limited. Thus, the big challenge in multiplexing is to create additional distinguishable dimensions. The multiplexing based on lifetime (temporal multiplexing) is a very promising concept. LTC based FRET is well suited in temporal multiplexing. Using the extremely long PL lifetimes of LTC and different donor-acceptor distances for a single donor-acceptor pair would allow for designing different FRET-quenched and FRET-sensitized PL decay times.

If different PL decay times can be distinguished, then temporal and spectral multiplexing could be reliably combined. When different acceptor PL intensities can also be distinguished and controlled, this parameter can be used as a third multiplexing dimension (**Figure 2.12**).

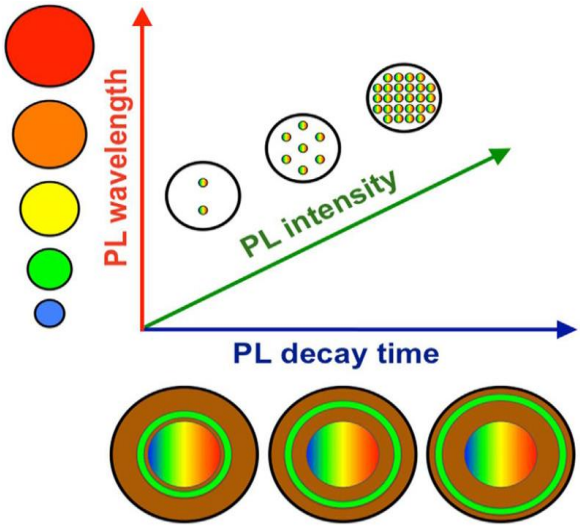

Figure 2.12. Photoluminescence multiplexing in three dimensions. The combination of PL wavelengths (e.g., from different QD sizes) with PL decay times (e.g., from different LTC-donor to QD-acceptor distances) and PL intensities (e.g., from different concentrations of the LTC-QD hybrid nanoparticles) can offer different distinguishable signals for multiplexed sensing or optical barcoding. (Reference [10], copyright 2014 Elsevier Publisher.)

Although the advantages of LTC for multiplexed FRET are numerous, and theoretical construction of a multiplexed LTC-based FRET is relatively easy, the practice is much more challenging. Pulsed excitation and time-gated or time-resolved detection must be combined with different wavelength separation technologies. Determination of conformational changes as well as distance distributions within a biological FRET system can most often only be determined by time-resolved measurements[3]. Time-resolved measurement provides more dynamic information that is available from the steady-state data. Time-dependent intensities are measured following short pulsed excitation of light. Data collection starts after the excitation pulse has decayed and fluorescent samples with long lifetimes even allow an almost background-free detection after the complete decay of detrimental effects such as sample auto-fluorescence.

Each fluorophore requires a distinct detection channel and excitation wavelength and spectral overlap, which needs to take into account the entire spectrum of each fluorophore (not only the full-width-at-half-maximum, FWHM), imposes fundamental limits to color multiplexing. Even the spectra of quantum dots (with FWHM of ~30 nm) extend over >100 nm, which limits the spectral range of 400 to 800 nm to approximately four completely distinct signals.

2.4 Fluorescent dyes

In the last decades, the popularity of organic dyes as fluorescent probes has steeply risen in biophysical research. Fluorescent dyes are often used as fluorescent labels attached to specific locations within the biomolecule. The message of the labeled object is qualitatively or quantitatively transferred by detecting the fluorescence intensity. The majority of common fluorophores such as fluoresceins, rhodamines, 4,4´-difluoro-4-bora-3a,4a-diaza-s-indacenes (BODIPY dyes) and cyanines have been widely used in bioimaging, biosensing, medical diagnosis, and environmental detection. Fluorescent dyes have many good chemical and physical properties, such as, easy chemical structure tuning, good biocompatibility, low-toxicity, easy metabolism in the biological system, and non-radiation which are based on their slight structure, high molar absorption coefficient, moderate-to-high fluorescence quantum yield, etc. However, their comparatively not narrow absorption and emission bands can favor crosstalk between different dye molecules and small Stokes shifts (typically less than 25 nm) can lead to serious self-quenching and fluorescence detection errors because of excitation backscattering effects. Fluorescence dye probes have been used to detect the structures of RNA and DNA, study the remedy of DNA damaged basic group, identify the status of the amino group and the active area of the protein molecule, distinguish nucleic acids with different conformation and the chemical reactive activities of related drugs.

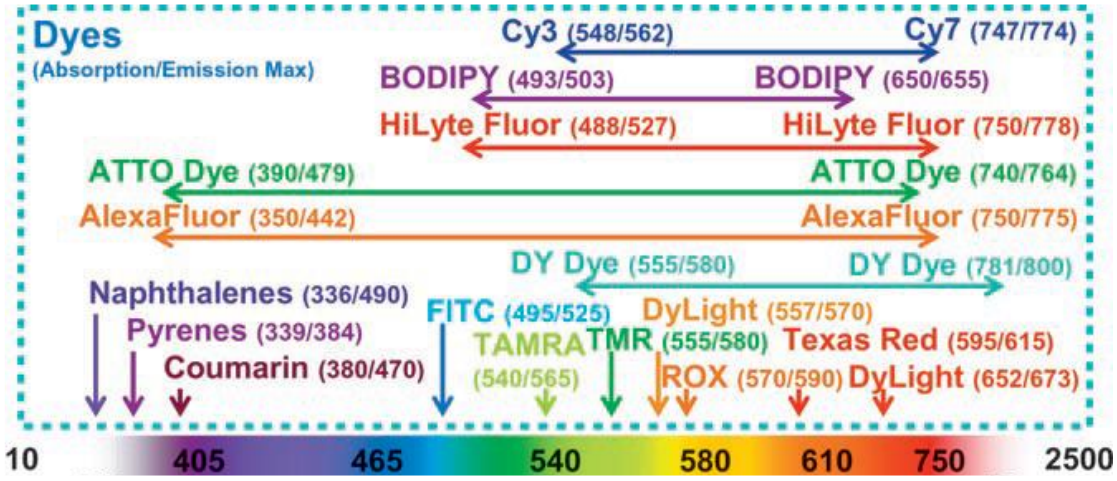

Figure 2.13. Examples of available fluorescent dye. (Reference [14], copyright 2006 Wiley-VCH Publisher)

2.4.1 Cyanine dyes

Cyanine dyes are small organic molecules with two nitrogen-containing aromatic heterocyclic rings linked via a polymethine bridge, which are also named polymethine cyanine dyes. Cyanine dyes are broadly used in the life sciences and other biologically related disciplines as optical probes of membrane potential[98], organelle[99], [100], labels for neuron pathway tracing[101] and as probes for membrane structure and dynamics. Moreover, their applications as fluorescent labels for proteins, nucleic acids and other demanding fluorescence microscopy applications made cyanine dyes more popular in the last two decades because of their remarkable photostability, good fluorescence efficiency, and commercial availability as derivatives for covalent labeling of proteins and nucleic acids. The small organic dyes with spectral properties are covalently or non-covalently bound to biomolecules. The interaction of small organic dyes with proteins or nucleic acids giving a detectable signal is a very useful method for the investigation of biological processes on the molecular level.

2.4.2 Cyanine dyes applications in FRET

Cyanine dyes as energy acceptors have been widely used in a variety of FRET biophysical applications. Lee[102] reported dye cyanine 3-labeled human serum albumin can be applied to construct QDs-based FRET systems by their high affinity interaction with CdZn SeS/ZnS QDs capped with multifunctional polymer ligands containing dihydrolipoic acid (DHLA). This dye-based FRET protein complex can serve as a sensitive sensor for probing the interaction of clofazimine with proteins using fluorescence spectroscopic techniques (**Figure 2.14A**). Löhmannsröben[103] developed an aptasensing system based on FRET from a lanthanide terbium complex to a cyanine 5 to detect L-selectin in PBS. FRET signal was measured by time-resolved luminescence spectroscopy. Using their system, L-selectin can effectively be recognized in the concentration range of 10-500 ng/ mL that covers the completely relevant pathological range for Alzheimer's disease (**Figure 2.14B**). Bald[104] investigated the FRET between the donor fluorescein and the acceptor cyanine 3 to establish a DNA origami-based dye array for light harvesting, signal amplification, and sensing. For the last 15 years, the most popular FRET probes in nucleic acid studies is cyanine dyes (**Figure 2.14C**).

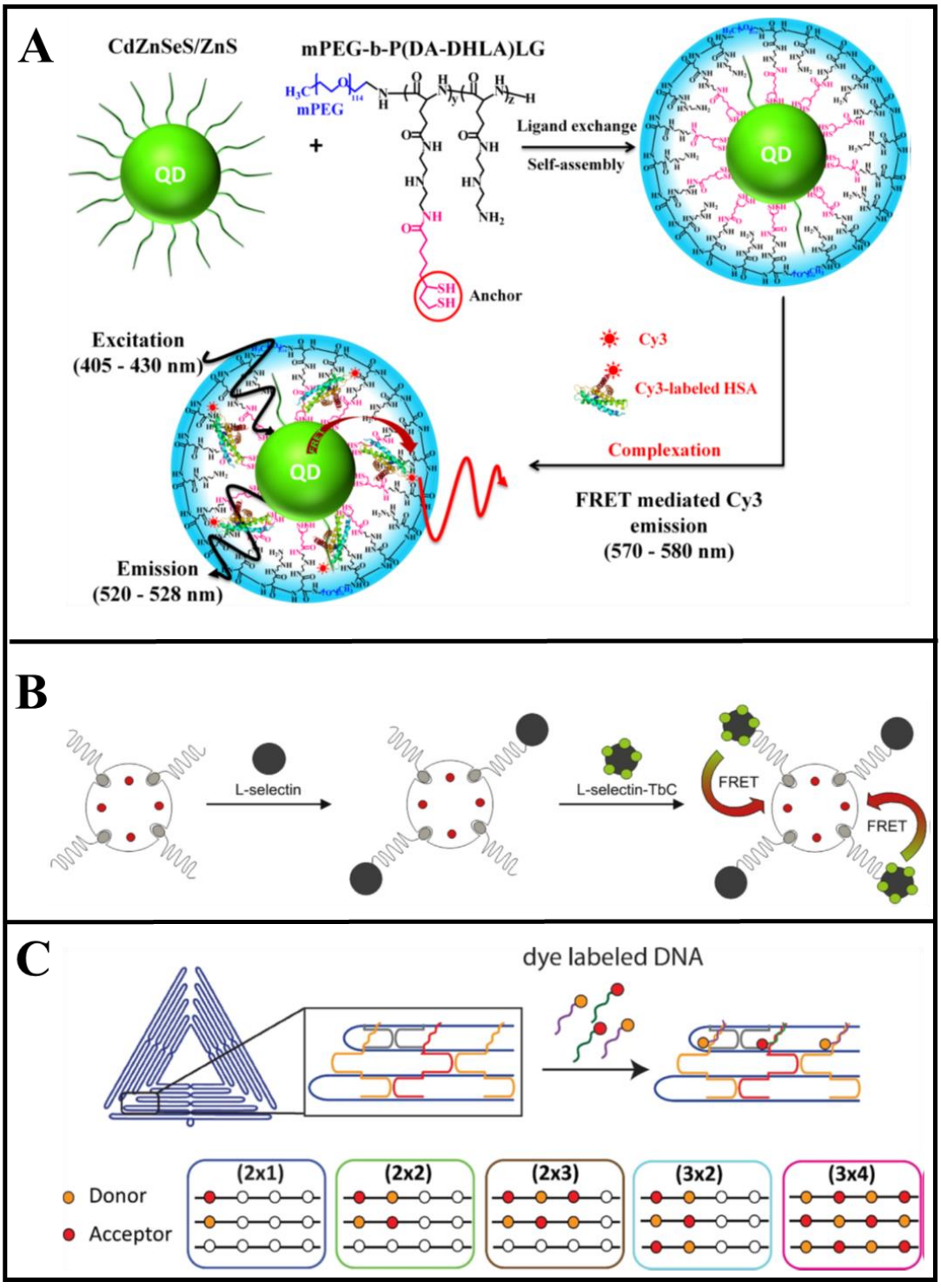

Figure 2.14. Cyanine dyes-based FRET biosensor, cyanine dyes as the acceptor with different donors.

(A) QD to Cy3 FRET sensor. (Reference [102], copyright 2016 ACS Publisher.)

(B) The L-selectin detection based on FRET from a Tb-complex to a cyanine dye. (Reference [103], copyright 2015 Elsevier Publisher.)

(C) DNA origami-based fluorescein to Cy3 FRET array. (Reference [104], copyright 2018 ACS Publisher.)

The disadvantage of organic dyes for FRET applications is their crosstalk, which results from direct acceptor excitation due to the relatively broad absorption bands of organic dyes and needs to render tedious correction of measured signals in multiplexing detection. Lifetime multiplexing can overcome this problem. It can be performed by making use of fluorophore-specific decay behavior, measured at a single excitation and a single emission wavelength to discriminate different decays. This approach has no crosstalk from different acceptors but requires sufficiently different lifetimes. Lifetime multiplexing, as well as combining spectral multiplexing can be used to realize multiplexing detection for nucleic acids detection in this thesis.

2.5 Quantum dots

Luminescent semiconductor nanocrystals, also known as quantum dots (QDs), are generally composed of atoms from groups II-VI (ZnO, ZnS, CdS, CdSe, CdTe) and III-V (GaN, GaP, GaAs, InP, InAs) elements in the periodic table and are defined as particles because of small physical dimensions between 1 and 12 nm [18]. QDs are nanometer-sized crystals with unique photochemical and photophysical properties, which are not available from either isolated molecules or bulk solids. For example, symmetrical emission spectra, high quantum yield, broad absorption spectra, good chemical, and photo-stability and size-dependent emission wavelength tunability. QDs can be covalently linked with biorecognition molecules such as peptides, antibodies, nucleic acids, or small-molecule ligands for use as biological labels. High-quality QDs are also well suited for optical encoding and multiplexing applications due to their broad excitation profiles and narrow emission spectra. QDs have been successfully used as luminescent probes with a considerable advantage over conventional organic fluorophores in many biological fields.

2.5.1 Photophysical properties

QDs have unique photophysical properties, including tunable photoluminescent emission as a function of core size and quantum confinement effects for binary combinations of semiconductors[17], [18]; broad absorption spectra with high molar extinction coefficients (10-100 times larger than those of conventional dyes) [105]; narrow symmetric PL spectra (full width at half maximum ~25-40 nm) spanning the UV to near-IR with relatively high quantum yields, large Stokes shifts and high resistance to both photobleaching and chemical degradation [106], [107]. Compared with conventional organic fluorophores (**Table 2.2**), QDs present considerable advantages, especially broadband excitation and narrow bandwidth emission are

the most important properties since they permit multiplexed analysis studies, in which more than one target are investigated simultaneously.

Table 2.2 Comparison of the properties of conventional organic fluorophores and quantum dots.

Property	Conventional organic dyes	QDs
Broadband excitation	×	√
Narrow bandwidth emission	×	√
Emit light of high intensity	Moderate	√
Available in many colors	√	√
Readily attachable to analytes	√	Moderate
Resistant to quenching	×	√
Photochemically stable	×	√
Cheap and readily available	√	×

*(Reference [108], copyright 2002 Elsevier Publisher)

The optical properties of QDs arise from interactions between electrons, holes, and their local environments. **Figure 2.15** shows the different-sized QDs and their fluorescence emission. The defining property of QD is that there is an energy gap (band-gap) between a filled continuum of electron energy states (valence band) and an empty continuum of states (conduction band). QDs absorb photons when the excitation energy exceeds the band gap. During this process, electrons are promoted from the valence band to the conduction band. The difference in energy between the discrete ground and excited states increases with increasing degree of confinement (i.e. decreasing particle size), the size of the band gap and the color of emitted light can be fine-tuned by adjusting the QD size. The composition of the material is another important parameter, which alters the energy gap of QD. QD with a diameter of 5 nm can be engineered to radiate photon between 610-800 nm by changing the construction of the alloy CdSe and Te [109], [110].

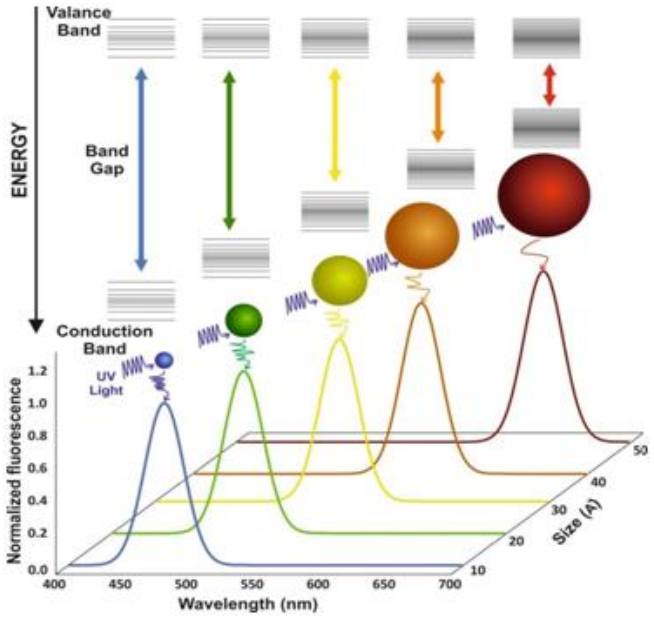

Figure 2.15. Size and composition tuning of optical emission for quantum dots. (Reference [110], copyright 2017 Med DocsCrave)

2.5.2 Bioconjugation

The conjugations of QDs with specific biological molecules are essential to their biological applications. QDs can be modified by a variety of biomolecules, including nucleic acids, antibodies, proteins, and peptides [111], [112]. In recent years, QD bioconjugation techniques have been developed very quickly [113]–[115]. There are two main approaches to immobilize biomolecules on the QD surface: covalent linking and non-covalent binding, including coupling directly to the QD surface or surface ligand coating the QD. The covalent linkage is obtained via different bioconjugation chemistry using activated functional groups at the surface of QDs. Non-covalent binding is determined by hydrophobic, electrostatic, or affinity interactions between biomolecules and the QD surface.

The most common covalent linking methods are using bifunctional groups EDC (1-ethyl-3(3-dimethylaminopropyl) carbodiimide hydrochloride) [116], DCC (dicyclohexylcarbodiimide) [117], NHS (N-hydroxy-succinimide) [118], SMCC (succinimidyl 4-N-maleimidomethyl cyclohexane-1-carboxylate) [119] to catalyze a reaction between the carboxylic acid group and amino group, generating a stable amide linkage.

Non-covalent attachment of biomolecules to the QD surface is mainly based on direct interaction, electrostatic interaction and high affinity secondary interactions. For example, metal-affinity driven coordination of polyhistidine to the metal atoms of QDs, then the

biomolecules could be coordinated to polyhistidine [120]. And the biotin-streptavidin interaction represents an extraordinary example of the molecular key lock system in life processes, and this system has become a powerful tool for bioconjugation due to their specific and high affinity interaction[121], [122].

Table 2.3 Strategies to couple various biomolecules onto QDs.

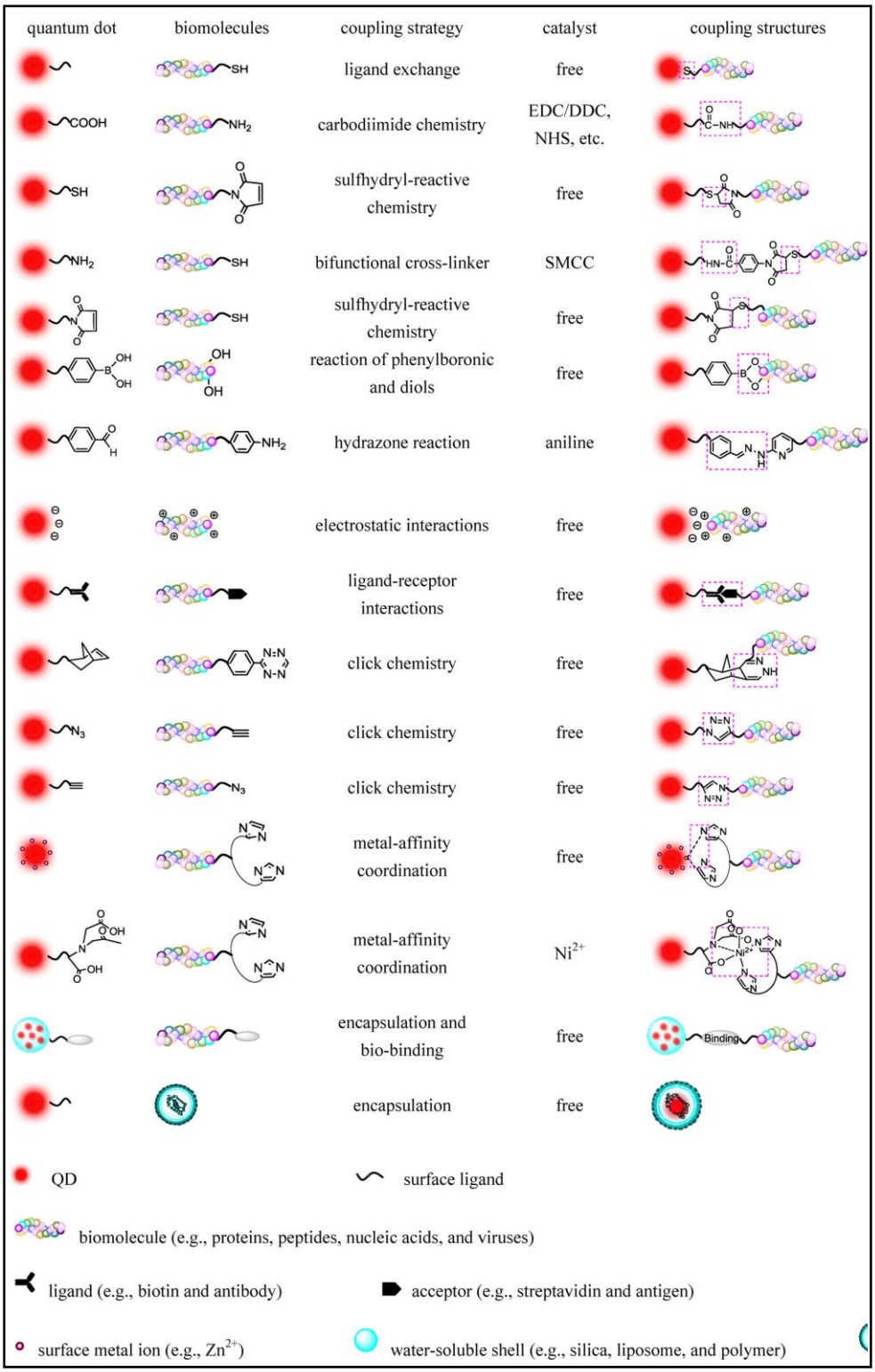

*(Reference [123], copyright 2015 ACS Publisher.)

2.5.3 QDs applications in FRET

The unique photophysical properties of QDs make them appealing as in vivo and in vitro fluorophores in a variety of biological investigations. The application of QDs for developing FRET-based biosensors provides many advantages, including high sensitivity (due to the brightness of QDs), multiplexing capability (due to the color tunability of QDs), and homogeneous assay formats (due to the biorecognition-specific FRET signal).

QDs can act as highly efficient FRET donors because of their continuously tunable emissions that can be matched to any desired acceptor, such as organic fluorophores or dyes, as well as metallic nanoparticles. Oh, et al [124] used the streptavidin-conjugated QDs as energy donors and the biotinylated AuNPs as acceptors to modulate the FRET efficiency between QDs and AuNPs. The avidin concentration can be obtained by monitoring the changes of the streptavidin-conjugated QDs fluorescence. This method exhibits a detection limit of 10 nM and it can be used for inhibition assays(**Figure 2.16A**). Zhang [6] developed a single QD-based FRET sensor combine with isothermal amplification for microRNA assays with a detection limit as low as 0.1 aM. The reaction of reporter oligonucleotides with the Cy5-labeled reporter probes and the biotinylated capture probes results in the formation of biotinylated Cy5-labeled hybrids. With the addition of streptavidin-functionalized QDs, the hybrids can be assembled on the surface of QDs to form Cy5-DNA-QD conjugates through biotin-streptavidin interactions, inducing FRET from the QD to Cy5. The counting of Cy5 fluorescence burst can be used for the measurement of target microRNAs (**Figure 2.16B**). Algar [125] developed a multifunctional QD-based concentric FRET sensor for simultaneous measurement of both protease concentration and protease activity. They labeled the thrombin-specific aptamer with a Cy3 dye for the measurement of thrombin concentration and labeled the peptide substrate with an Alexa Fluor 647 dye for thrombin activity. After the conjugation of Cy3-labeled aptamer and Alexa Fluor 647 dye-labeled peptide substrate with DHLA-PEG-coated QD524, a concentric FRET sensor is obtained with the involvement of three FRET pathways: (i) FRET with the QD as the energy donor and Cy3 as the energy acceptor, (ii) FRET with the QD as the energy donor and Alexa Fluor 647 dye as the energy acceptor, and (iii) FRET with Cy3 as the energy donor and Alexa Fluor 647 dye as the energy acceptor. The concentric FRET signals may be modulated by either thrombin-induced displacement of Cy3-labeled oligonucleotide or cleavage of the peptide substrate by thrombin. Additionally, this sensor can be used for the discrimination of active thrombin from inactive thrombin and other proteases (**Figure 2.16C**).

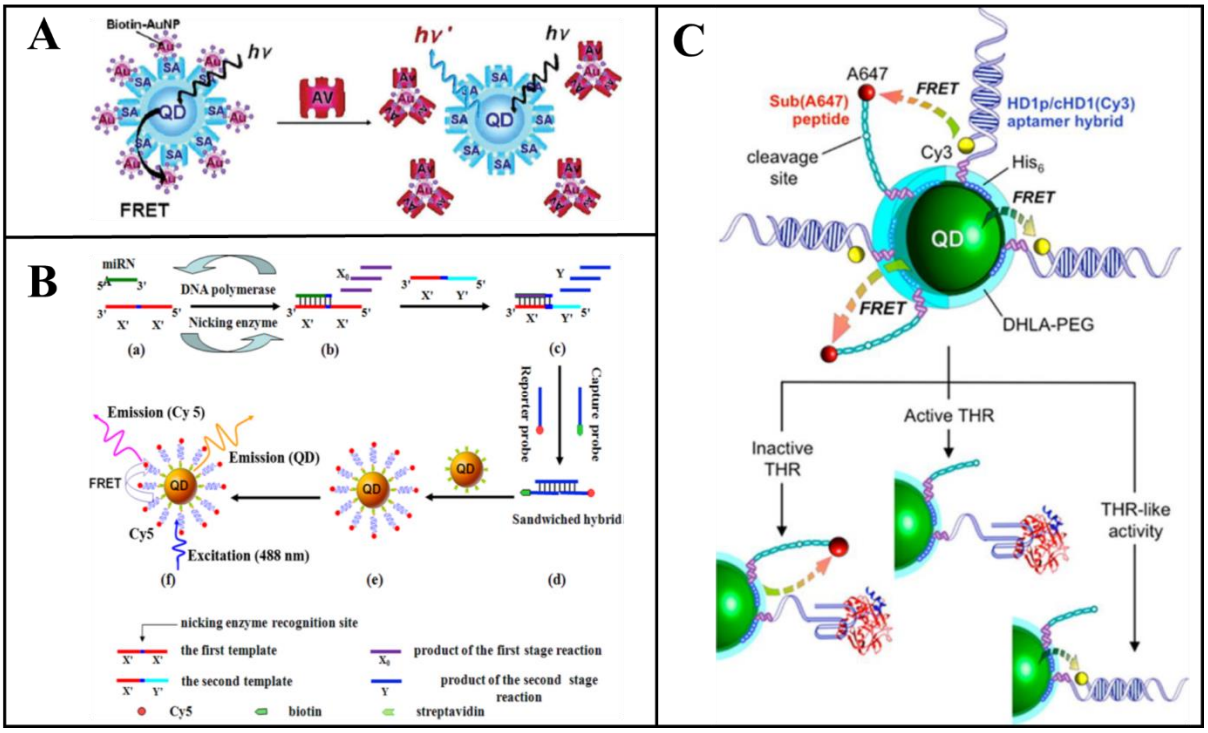

Figure 2.16. QD-based FRET biosensor QDs as the donor with different acceptors.

(A) Schematic illustration of inhibition assay method based on the PL quenching of SA-QDs by Biotin-AuNPs. (Reference [124], copyright 2005 ACS Publisher.)

(B) FRET between 605QD and Cy5 through streptavidin-biotin binding. (Reference [6], copyright 2011 ACS Publisher.)

(C) Multiplexed FRET between QD, Cy3 and Alexa Fluor 647 dye. (Reference [125], copyright 2014 ACS Publisher.)

QDs are typically not used as FRET acceptors because of their broad excitation band, which causes direct absorption of excitation light in many situations. However, they can become very effective FRET acceptors when luminescent lanthanide complexes (e.g., terbium and europium complexes) are employed as FRET donors. Lanthanides complexes with milliseconds PL decay time can be prospective FRET donors in combination with QD acceptors, providing a potentially significant increase in FRET efficiency. Time-gated detection provides extremely low background noise and a quick and simple one-step assay format[126], [127]. QDs as energy acceptors potentially offers various perspectives such as the possibility of very large Förster radii, low detection limits, and multiplex analysis in the study of interactions within very large molecules, and in the biomedical analysis by high throughput screening.

Since 2007, Hildebrandt [128] reported a highly sensitive FRET Immunoassay using LTC as donors and QDs as acceptors, our group developed a series of Tb-QD complex-based FRET

biosensors for time-resolved immunoassay clinical diagnostics, and the detection of various biomarkers (e.g., carcinoembryonic antigen, prostate-specific antigen, a fetoprotein, epidermal. growth factor receptor, and microRNAs). Moreover, the construction of a QD-based FRET biosensor with LTC as the donor and different-colored QDs as the acceptor enables the simultaneous spectral multiplex assay. Bhuckory [129] present a facile and functional QD-antibody conjugation method using three commercially available QDs with different PL maxima (605 nm, 655 nm, and 705 nm) (**Figure 2.17A**). The QD-antibody conjugates were successfully applied for FRET immunoassays against prostate specific antigen (PSA) in 50 μL serum samples using Lumi4-Tb antibody conjugates as FRET donors and time-gated PL detection. The results show that FRET based on QD acceptors is suitable for multiplexed and sensitive biomarker detection in clinical diagnostics. Qiu [8] also demonstrated the use of three different color QDs (605, 655, and 705 nm) and LTC for multiplexed detection of multiple microRNAs based on the measurement of the FRET ratio (**Figure 2.17B**). In addition, the QD can function as both the energy acceptor and the energy donor in the development of a sequential FRET sensor [130]. With the integration of the QD terbium complex-based FRET and the QD-dye-based FRET, the sequential FRET can be applied for multiplexed monitoring activities of protease and the construction of biophotonic logic devices.

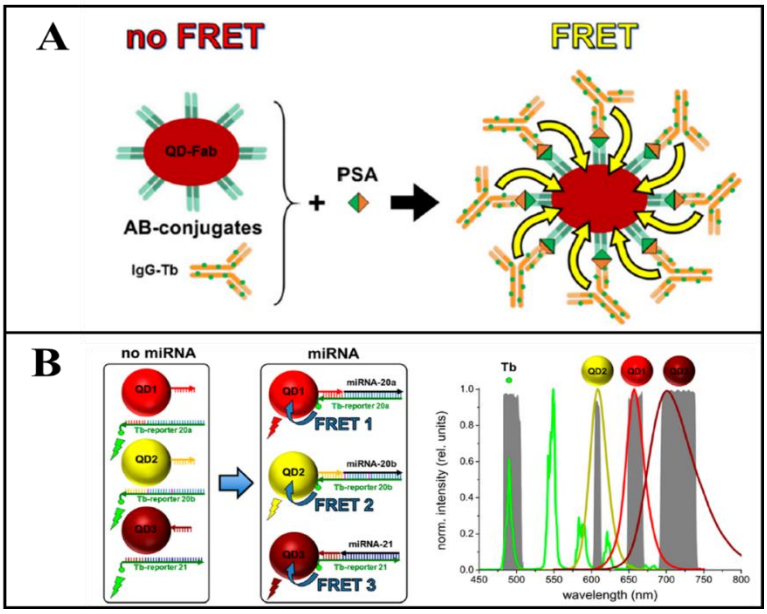

Figure 2.17. QD-based multiplexed FRET biosensor with LTC as the donor and different color QDs as the acceptors.

(A) The principle of the Tb-to-QD FRET immunoassay against PSA. (Reference [129], copyright 2016 MDPI Publisher.)

(B) The three FRET systems based on LTC to three different QDs for multiplexed microRNA detection. (Reference [8], copyright 2015 ACS Publisher.)

3. Temporal duplexing Tb-Dye HCR-FRET microRNA detection assay

3.1 Introduction

Recently, more and more FRET-based biosensors are being developed for use in nucleic acids detection and diagnosis field as a simple, rapid, and sensitive transduction mechanism[131]–[133]. In order to detect low concentration nucleic acids, many different exponential and linear nucleic acid amplification and signal amplification strategies (without the generation of new nucleic acid products) have been developed over the last few decades[134] including reverse transcription quantitative polymerase chain reaction (RT-qPCR)[135], [136], rolling circle amplification (RCA)[137], [138], and strand displacement amplification (SDA)[139][140]. Despite very high sensitivities and specificities of such techniques, they all require enzymes and in some cases RNase inhibitors[6], [141], can be quite time consuming, and may be not isothermal and exponentially amplified. One of the most simple isothermal signal amplification methods is hybridization chain reaction (HCR) because it is completely enzyme-free[142]. HCR has been widely used to construct various biosensing platforms, including the detection of DNA[143], [144], miRNA[145], [146], messenger-RNA[147], [148], proteins[149], [150], and cells[151]. HCR technologies have been significantly advanced for both multiplexed imaging and quantitation of endogenous nucleic acids.

The HCR can be further improved by attaching FRET donor-acceptor pairs to the HCR probes[132], [143], [151], [152]. With this approach, HCR amplification leads to double-stranded DNA concatemers with many donors and acceptors in close proximity. Only HCR amplification can lead to FRET because free HCR FRET probes are separated and cannot engage in energy transfer. Although HCR-FRET has been demonstrated for both imaging in cells and quantification in solution, multiplexing has not been realized and low pM limits of detection could only be accomplished by double-step amplification[153]. Merging the multiplexing capabilities of luminescent terbium complex, temporal duplexed detection of a single FRET pair, and separation-free assay format of time-gated (TG) FRET with the enzyme-free amplification of HCR has the potential to significantly advance nucleic acid biosensing.

To demonstrate the feasibility of simple and sensitive HCR nucleic acid multiplexing, we selected two different miRNAs, miR-21 and miR-20a, both of which were found to be related

to different cancers[154]. Here, we implement a Tb-dye TG-FRET pair into HCR probes to demonstrate temporally multiplexed enzyme-free quantification of two different miRNAs with a single measurement, a single excitation wavelength, and a single detection channel. Both very low LODs (down to a few hundred attomoles) and high selectivity against very homologous miRNAs (dual-nucleotide variants) demonstrated the unprecedented performance of our multiplexed HCR-TG-FRET assay.

3.2 Materials and methods

3.2.1 Materials

Lumi4-Tb-NHS (Tb) was provided by Lumiphore Inc. Cyanine5.5 NHS ester was purchased from Lumiprobe. All oligonucleotides were purchased from Eurogentec. Non-modified oligonucleotides were purified by the supplier. Cy5.5-modified oligonucleotides were purified with HPLC. All sequences and modifications of nucleic acids used in this study are summarized in Table 3.1. Both Cyanine5.5 (Lumiprobe) and Cy5.5 (GE Healthcare Cy dye used by Eurogentec for functionalization) are referred to as Cy5.5 because of their very similar photophysical properties and chemical structures. Tris(hydroxymethyl)-aminomethane, bovine serum albumin, and HEPES were purchased from Sigma-Aldrich. NaCl was purchased from Duchefa. All chemicals were used as received. Water was purified by MAXIMA (USF Elga, UK). Zeba Spin Desalting Columns (7 kDa MWCO) were purchased from Thermo Fisher Scientific.

Table 3.1. DNA and miRNA oligonucleotides used in the study (mismatches between miR-20a and miR-20b shown in red, Tb-functionalization shown in green, Cy5.5 functionalization shown in blue)

Name	Sequence 5'-3'
has-miR-20a	**UAAAGUGCUUAUAGUGCAGGUAG**
has-miR-20b	**CAAAGUGCUCAUAGUGCAGGUAG**
has-miR-21	**UAGCUUAUCAGACUGAUGUUGA**
ssDNA-20a	**TAAAGTGCTTATAGTGCAGGTAG**
ssDNA-20b	**CAAAGTGCTCATAGTGCAGGTAG**
ssDNA-21	**TAGCTTATCAGACTGATGTTGA**
Hairpin probe 1 (H1)	**CCTGCACTATAAGCACTTTATAGCCTTAAAGTGCTTATAG-Tb**
Hairpin probe 2 (H2)	**TAAAGTGCT(Cy5.5)TATAGTGCAGGCTATAAGCACTTTAAGGCTA**
Hairpin probe 3 (H3)	**Tb-CAGACTGATGTTGATAGCCTTCAACATCAGTCTGATAAGC**
Hairpin probe 4 (H4)	**AGGCTATCAACATCAGTCTGGCTTATCAGACTGATGTTGA-Cy5.5**

Tb-DNA conjugates (Hairpin probes 1 and 3) were obtained by mixing Lumi4-Tb-NHS (lyophilized product dissolved was in anhydrous DMF to a final concentration of 8 mM stock solution) in concentration excess to amino-functionalized oligonucleotides in 100 mM carbonate buffer at pH 9.0. The mixtures were incubated overnight at 4°C. The Tb-DNA conjugates were purified three times by Zeba Spin Desalting Columns (7 kDa MWCO). Complete bioconjugation of DNA with Tb (~100 %) was verified by absorbance measurements at 340 nm for Tb and 260 nm for DNA.

Dye-DNA conjugates were purchased at Eurogentec with 3'-terminal Cy5.5 (Hairpin probe 4) or prepared by mixing Cyanine5.5 NHS ester (lyophilized product dissolved in anhydrous DMF to a final concentration of 16.6 mM stock solution) in concentration excess to amino-functionalized oligonucleotides in 100 mM carbonate buffer at pH 9.0 (Hairpin probe 2). The prepared mixtures were incubated overnight at 4°C and then purified three times by Zeba Spin Desalting Columns (7 kDa MWCO). Complete bioconjugation of DNA with Cy5.5 (~100 %) was provided by Eurogentec (Hairpin probe 4) or verified by absorbance measurements at 684 nm for Cy5.5 and 260 nm for DNA (Hairpin probe 2).

Spectroscopic characterization. Absorption spectra (Lambda 35 UV/Vis System, PerkinElmer) and emission spectra (Xenius, SAFAS) for Tb and dye functionalized DNA were recorded in HEPES (100 mM, pH 7.4). All spectra are shown in **Figure 3.1**. Both Cy5.5 dyes have very similar spectra, use the same PL detection bandpass filter, and lead to almost identical Förster distances. A Förster distance (the donor-acceptor distance for which FRET is 50 % efficient) for the Tb-Cy5.5 FRET pair of R_0 = 5.8±0.2 nm was calculated using **Equation 3.1**:

$$R_0 = 0.0211(\kappa^2 \Phi_D n^{-4} J)^{1/6} \quad \text{nm} \tag{3.1}$$

An orientation factor of κ^2 = 2/3 was used because of the random orientation of donor and acceptor during the FRET time (dynamic averaging), which is well justified by the long PL lifetime of the Tb donors and their unpolarized emission (fast isotropic rotation). A refractive index of n = 1.35 (aqueous solution) was used. The Tb-centered quantum yield was Φ_D = 0.78±0.05. The spectral overlap integral J was calculated by **Equation 3.2**:

$$J = \int_{450\ nm}^{700\ nm} I_D(\lambda)\varepsilon_A(\lambda)\lambda^4 d\lambda \tag{3.2}$$

where $I_D(\lambda)$ is the emission intensity from the area-normalized (to unity) emission spectrum of the Tb donor and $\varepsilon_A(\lambda)$ is the molar absorptivity of the acceptor

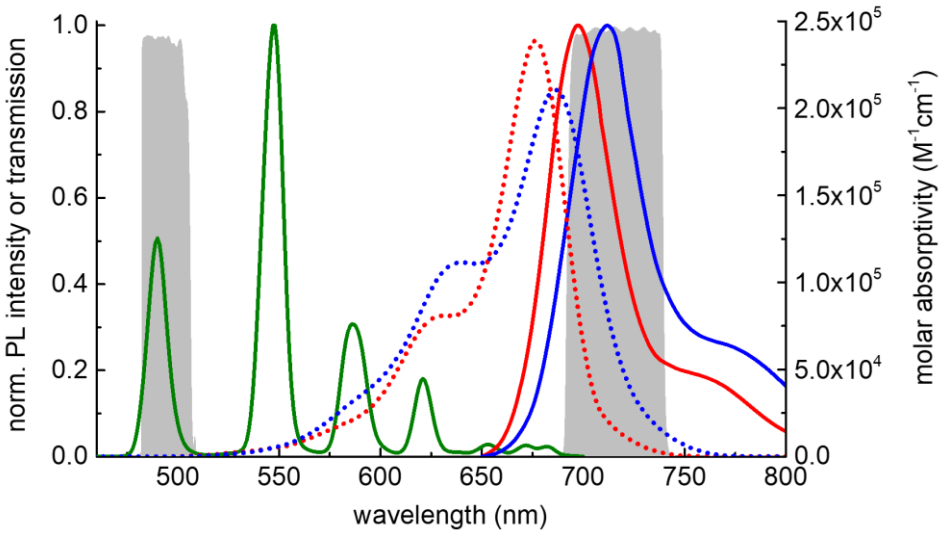

Figure 3.1. Photophysical properties of the Tb-Cy5.5 FRET pair. Absorbance spectra (dotted, right axis) and PL emission spectra (line, left axis) of Cy5.5 (red for Cy5.5 from Eurogentec and blue for Cy5.5 from Lumiprobe). PL emission spectrum of Tb (green, left axis). The absorption spectrum of Tb not shown (maximum molar absorptivity of 26,000 M^{-1} cm^{-1} at 340 nm). Transmission spectra of optical bandpass filters were 494/20 (Semrock) for the Tb detection channel and 716/40 (Semrock) for the Cy5.5 detection channel (gray, left axis).

3.2.2 HCR-FRET miRNA/ssDNA single target assays.

Stock solutions (30 nM) of hairpin probes were prepared in DNA hybridization buffer (20 mM Tris-Cl, 500 mM NaCl, 0.1% BSA, pH 8.0). Hairpin probes were heated to 95 ℃ for 2 min and then cooled down to room temperature for 2 hours to form hairpin structures. The annealed hairpin probes were stored in the refrigerator (4 ℃). For the detection of the target, 10 µL H1/H3 and 10 µL target miRNA/ssDNA at different concentrations were added into 0.5 mL Eppendorf tubes. After incubation at room temperature for 30 min, 10 µL H2/H4 were added and the mixture was further incubated for 60 min. Then, 120 µL hybridization buffer was added into the solution for obtaining a sufficient assay volume. From the total volume of 150 µL, 140 µL were transferred into black 96-well microtiter plates for miRNA/ssDNA TG-FRET assays and PL decay analysis. TG-FRET assays were performed on a clinical immunofluorescence plate reader “KRYPTOR compact plus” (Thermo Fisher Scientific) with time-gated (0.1 to 0.9 ms) PL intensity detection using optical bandpass filters (Semrock) with 494±20 nm for the Tb detection channel and 716±40 nm for the Cy5.5 detection channel. For ratiometric analysis, FRET ratios were calculated by the ratio of Cy5.5 and Tb time-gated PL intensities.

3.2.3 HCR-FRET miRNA/ssDNA duplexed assays.

30 nM hairpin probes mixtures (H1+H3 and H2+H4, respectively) in DNA hybridization buffer were heated to 95 ℃ for 2 min and then cooled down to room temperature for 2 hours to form hairpin structures. The annealed hairpin probes were stored in the refrigerator (4 ℃). The reaction process is performed as same as single target assays, then the samples were transferred into black 96-well microtiter plates for miRNA/ssDNA TG-FRET assays and PL decay analysis by a fluorescence lifetime plate reader (Edinburgh Instruments) using 4000 detection bins of 2 μs integration time and pulsed nitrogen laser (MNL 100, LTB Berlin) excitation (337.1 nm, 20 Hz). TG-FRET assays used two TG PL detection windows (TG_1: 0.1 to 1.0 ms and TG_2: 2.0 to 3.0 ms) for FRET-ratio calculation. TG PL intensities (I^{TG}) of Cy5.5 and Tb were determined at constant concentrations of hairpin probes and increasing concentrations of targets. These TG PL intensities were then used to calculate a background-subtracted FRET-ratio ($F_{\text{R-BG}}$, **Equation 3.3**) for each target concentration $c = x$.

$$F_{\text{R-BG}} = \frac{I^{TG}_{Cy5.5}(c=x)}{I^{TG}_{Tb}(c=x)} - \frac{I^{TG}_{Cy5.5}(c=0)}{I^{TG}_{Tb}(c=0)} \tag{3.3}$$

The concentration-dependent $F_{\text{R-BG}}$ values were used to determine the calibration curves for each miRNA (or ssDNA) target in each detection window. The slopes of the four linearly fitted calibration curves (z_{20a}^{TG1}, z_{21}^{TG1}, z_{20a}^{TG2}, z_{21}^{TG2}) were used to determine the concentrations in the duplexed assays that led to the concentration recovery. **Equation 3.4** was used for determining the target concentrations of miR-20a and miR-21 (or the ssDNA analogs) in the duplexed assays.

$$\begin{bmatrix} {F_{\text{R-BG}}}^1 \\ {F_{\text{R-BG}}}^2 \end{bmatrix} = \begin{bmatrix} c(\text{miR-20a}) \\ c(\text{miR-21}) \end{bmatrix} \times \begin{bmatrix} z_{20a}^{TG1} & z_{21}^{TG1} \\ z_{20a}^{TG2} & z_{21}^{TG2} \end{bmatrix} \tag{3.4}$$

where ${F_{\text{R-BG}}}^1$ and ${F_{\text{R-BG}}}^2$ are the background-subtracted FRET-ratios in TG PL detection windows TG_1 and TG_2, respectively.

3.2.4. Gel Electrophoresis

Hairpin probes H1 (0.9 μM) and H2 (0.9 μM) were heated to 95 ℃ for 2 min and cooled down slowly at room temperature for at least 2 hours to form the hairpin structure before use. 10 μL H1 and 10 μL target miRNA-20a of different concentrations were added into 0.5 mL Eppendorf tubes. After incubation at room temperature for 30 min, 10 μL H2 was added and the mixture was further incubated for 60 min. SYBR green II (Thermo Fisher) was used as DNA stain and an 8% polyacrylamide gel was prepared with 1×TBE buffer (pH 8.0). 15 μL of each sample was loaded into the lane and electrophoresis was performed on a Mini-PROTEAN Tetra

electrophoresis system (Bio-Rad) at a constant potential of 200 V for 30 min with 0.5×TBE (pH 8.0) as running buffer. The gel was then visualized under UV light (**Figure 3.3**).

3.3 Results and discussion

3.3.1 The principle of duplexed HCR-FRET

The principle of enzyme-free duplexed miRNA detection based on a single Tb-Cy5.5 FRET pair and HCR is shown in **Figure 3.2**. Hairpin probes H1 and H3 were labeled with FRET donor Tb, whereas hairpin probes H2 and H4 were labeled with FRET acceptor Cy5.5 (internally for H2 and terminally for H4). System H1/H2 was designed for miR-20a and system H3/H4 for miR-21 detection. All hairpin probes have 14 base-pair stems, 6 nucleotide loops, and 6 nucleotide sticky ends. Complementary sequences between H1 and H2 (H3 and H4) are shown in the same colors. The 6 nucleotides sticky end of H1 (H3) is complementary to the loop of H2 (H4) and the 6 nucleotides sticky end of H2 (H4) is complementary to the loop of H1 (H3). In the absence of targets, all probes are stable in hairpin structures. Thus, Tb and Cy5.5 are separated in solution (no FRET). In the presence of targets, which are complementary to H1 (H3), an unbiased strand-displacement reaction opens the hairpin H1 (H3). The newly exposed ssDNA sequence of H1 (H3) will then be able to open hairpin H2 (H4). The consequently exposed ssDNA sequence of H2 (H4) is identical to the target sequence, which triggers the HCR that forms a long double-stranded DNA (dsDNA) composed of H1 and H2 (H3 and H4). Because H1 and H2 (H3 and H4) are conjugated with Tb and Cy5.5, many of these FRET-pairs are brought into close proximity. Thus, HCR produces an amplified TG-FRET signal. Another important feature of our HCR-TG-FRET system are the different Tb-to-Cy5.5 distances in the H1/H2 and H3/H4 concatemers, respectively. Due to the internal labeling of H2 with Cy5.5, the Tb-Cy5.5 distance (d_1) in the H1/H2 HCR product is significantly closer than the one in the H3/H4 HCR product (d_2).

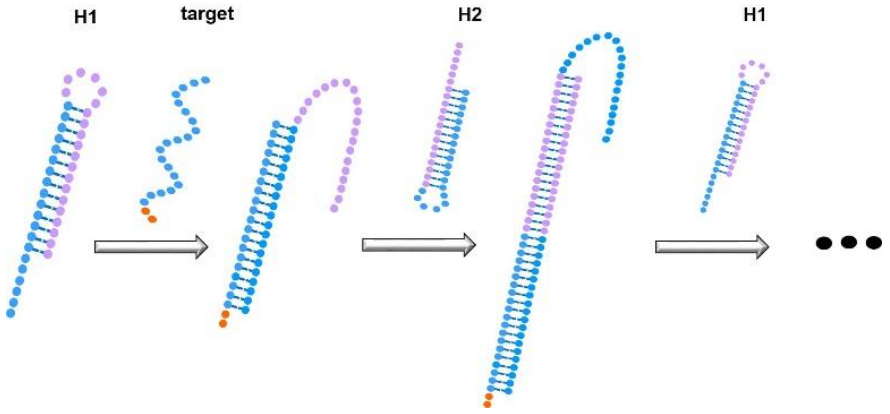

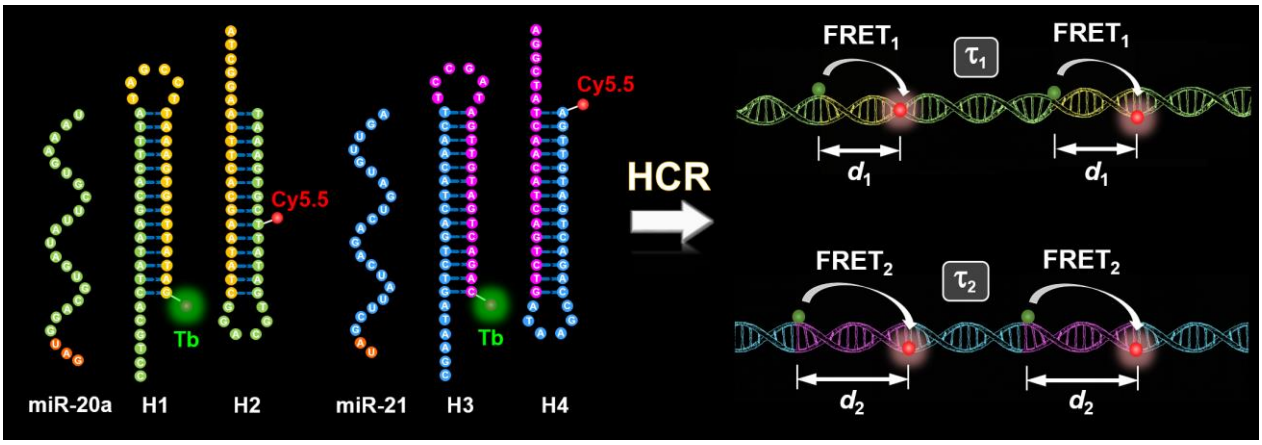

Figure 3.2. Top: The principle of the HCR process. **Bottom:** Schematic representation for duplexed (miR-20a and miR-21) detection of miRNAs using HCR-TG-FRET. Long dsDNA concatemers are shown on the right. Tb and Cy5.5 are in close proximity and can engage in FRET. The different distances in the two different HCR products (d_1 and d_2) will lead to different PL decays.

FRET efficiency (E_{FRET}) is proportional to the inverse sixth power of the distance between the donor and the acceptor, and the higher E_{FRET}, the stronger the quenching of the donor PL decay time (τ_D)[3], [46]. Thus, the longer distance d_2 will cause a lower FRET efficiency and a longer FRET-quenched donor PL decay time (τ_{DA}) compared to the shorter distance d_1. Owing to the *ca.* 10^6-fold difference between the PL lifetimes of Tb (~ms) and Cy5.5 (~ns), the FRET-sensitized lifetime of the Cy5.5 acceptor (τ_{AD}) is the same as the FRET-quenched lifetime of the Tb donor ($\tau_{AD} = \tau_{DA}$)[10]. These relations between FRET efficiency, distance, and PL decay times are summarized in **Equation 3.5** (3.5a for distance d_1 and 3.5b for distance d_2)[3], [10], [46].

$$E_{\mathrm{FRET}_1} = \frac{{R_0}^6}{{R_0}^6 + {d_1}^6} = 1 - \frac{\tau_{\mathrm{DA1}}}{\tau_{\mathrm{D}}} = 1 - \frac{\tau_{\mathrm{AD1}}}{\tau_{\mathrm{D}}} \quad (3.5a)$$

$$E_{\mathrm{FRET}_2} = \frac{{R_0}^6}{{R_0}^6 + {d_2}^6} = 1 - \frac{\tau_{\mathrm{DA2}}}{\tau_{\mathrm{D}}} = 1 - \frac{\tau_{\mathrm{AD2}}}{\tau_{\mathrm{D}}} \quad (3.5b)$$

3.3.2. MicroRNA-Specific HCR-TG-FRET

To confirm both the target-specific formation of luminescent HCR products and the different Tb-Cy5.5 donor-acceptor distances inside the two different HCR products (for miR-20a and miR-21), we performed gel electrophoresis and time-resolved PL spectroscopy. The gels (performed for miR-20a only) showed two main bands, one for the hairpin probes and another for the HCR products (**Figure 3.3**). For single hairpin probes without target (first two lanes), no HCR product could be observed and for the mixed hairpin probes (third lane), only a very

weak HCR product band appears (non-specific opening of the hairpin probes). When increasing target concentrations were added to the mixed hairpin probes, the HCR bands became clearly visible whereas the intensity of the hairpin probe bands got weaker with increasing target concentration because more H1 and H2 was consumed to form dsDNA structures (HCR products) with higher molecular weight. The formation of dsDNA structures of different lengths (different molecular weights) resulted in relatively broad smearing of the HCR bands. At the highest concentration (0.16 μM), different bands became clearly visible, indicating the formation of shorter dsDNA HCR products. The availability of many targets at such high target concentrations led to the formation of many assembly sites and a lower probability for H1 and H2 to assemble into longer structure[143][155].

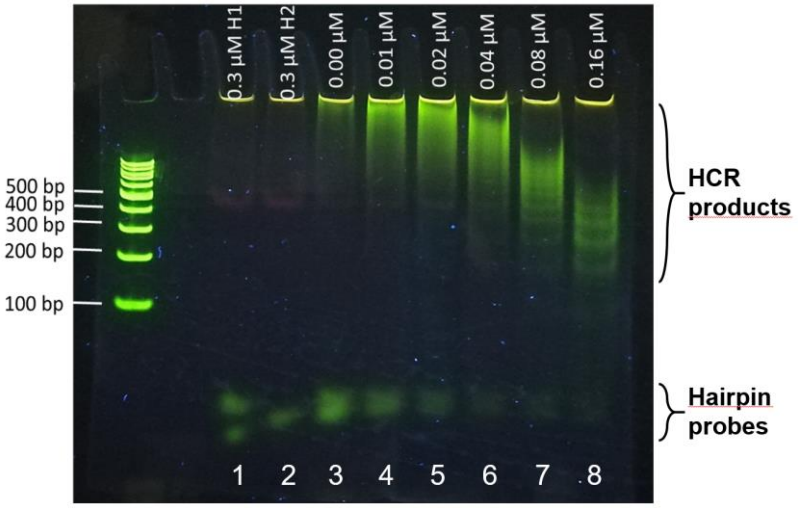

Figure 3.3. Electrophoresis gels for single hairpins (H1 in lane 1 and H2 in lane 2), mixed hairpins (H1 and H2 in lane 3), and mixed hairpins with increasing target (miR-20a) concentrations (0.01 to 0.16 μM in lanes 4 to 8). Hairpin probe bands are split due to open and closed probes.

Time-resolved PL curves of FRET-sensitized Cy5.5 at different target concentrations (between 0.01 and 0.7 nM) clearly showed the different decay times caused by the different Tb-Cy5.5 distances (**Figure 3.4**). Owing to the shorter distance, miR-20a-specific HCR products led to significantly faster decays (τ_{DA} = 360±10 μs) than the miR-21-specific HCR products (τ_{DA} = 930±50 μs). These average PL decay times resulted in FRET efficiencies of E_{FRET}(miR-20a) = 0.87±0.01 and E_{FRET}(miR-21) = 0.66±0.02, and distances of d_1 = 4.3±0.1 nm and d_2 = 5.2±0.2 nm. On the basis of a distance of ~0.33 nm between two bp within a dsDNA[156] and the 12 bp (miR-20a-specific HCR product) and 20 (miR-21-specific HCR product) Tb-Cy5.5 separation, the expected distances would be 4.0 and 6.6 nm. Taking into account the

differences in Cy5.5-DNA conjugation (internal labeling for H2 and terminal labeling for H4), the flexible linkers between the DNA and the fluorophores, and the many nicks inside the long dsDNA HCR products, these values are in relatively good agreement with the measured average distances d1 and d2. The most important property for our multiplexing approach was the significant difference between the two decay times (caused by different distances), and the exact reason for the differences in expected and measured donor-acceptor distances is of minor relevance. The decay curves for both miRNA targets also show increasing intensities with increasing target concentrations, which confirms the concentration-dependent HCR production and the possibility to use TG-FRET for miRNA quantification. The PL curves of miRNAs equivalent ssDNAs are also shown in **Figure 3.5**.

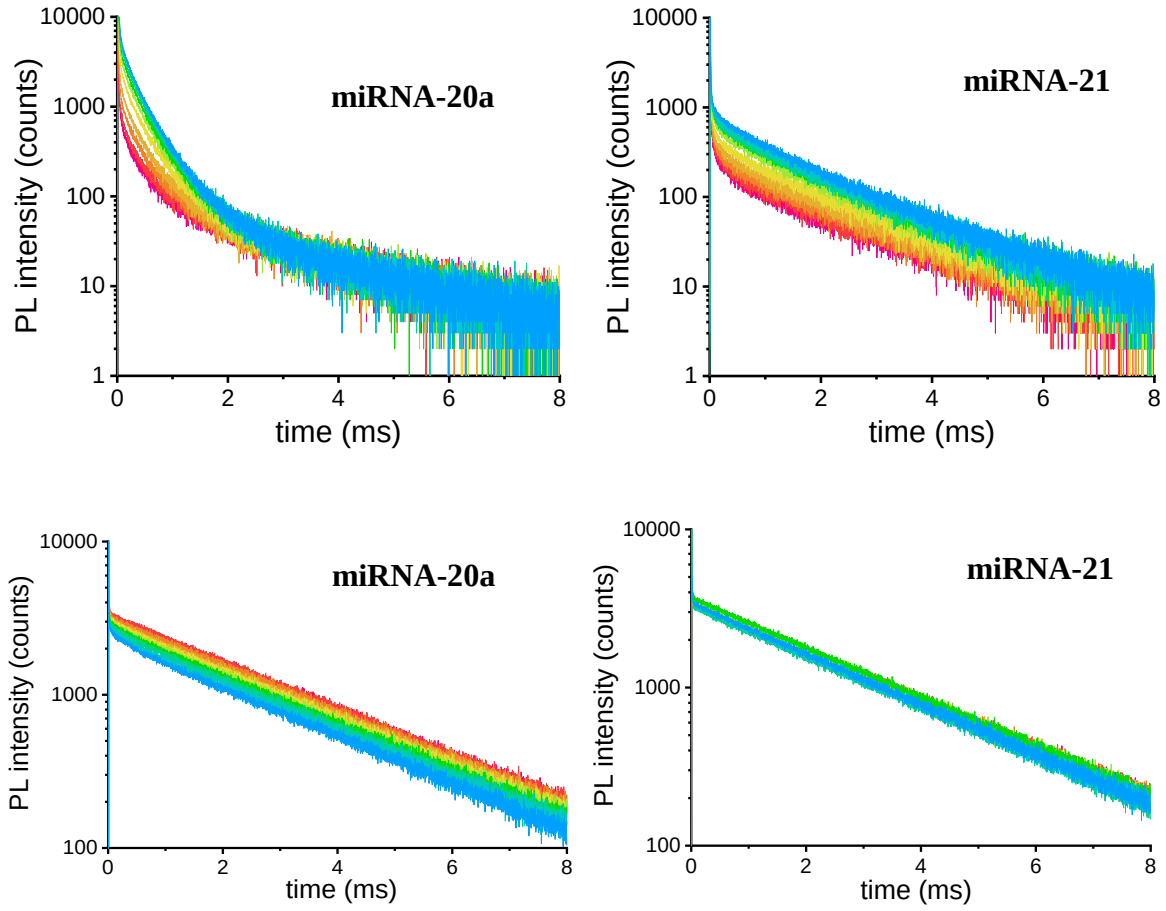

Figure 3.4. PL decay curves of the Cy5.5 FRET acceptor (top) and Tb FRET donor (bottom) for miR-20a (left) and miR-21(right) detection at increasing target concentrations (0, 0.01, 0.05, 0.1, 0.2, 0.3, 0.4, 0.5, 0.6, and 0.7 nM from pink to blue) and constant hairpin concentrations (2 nM).

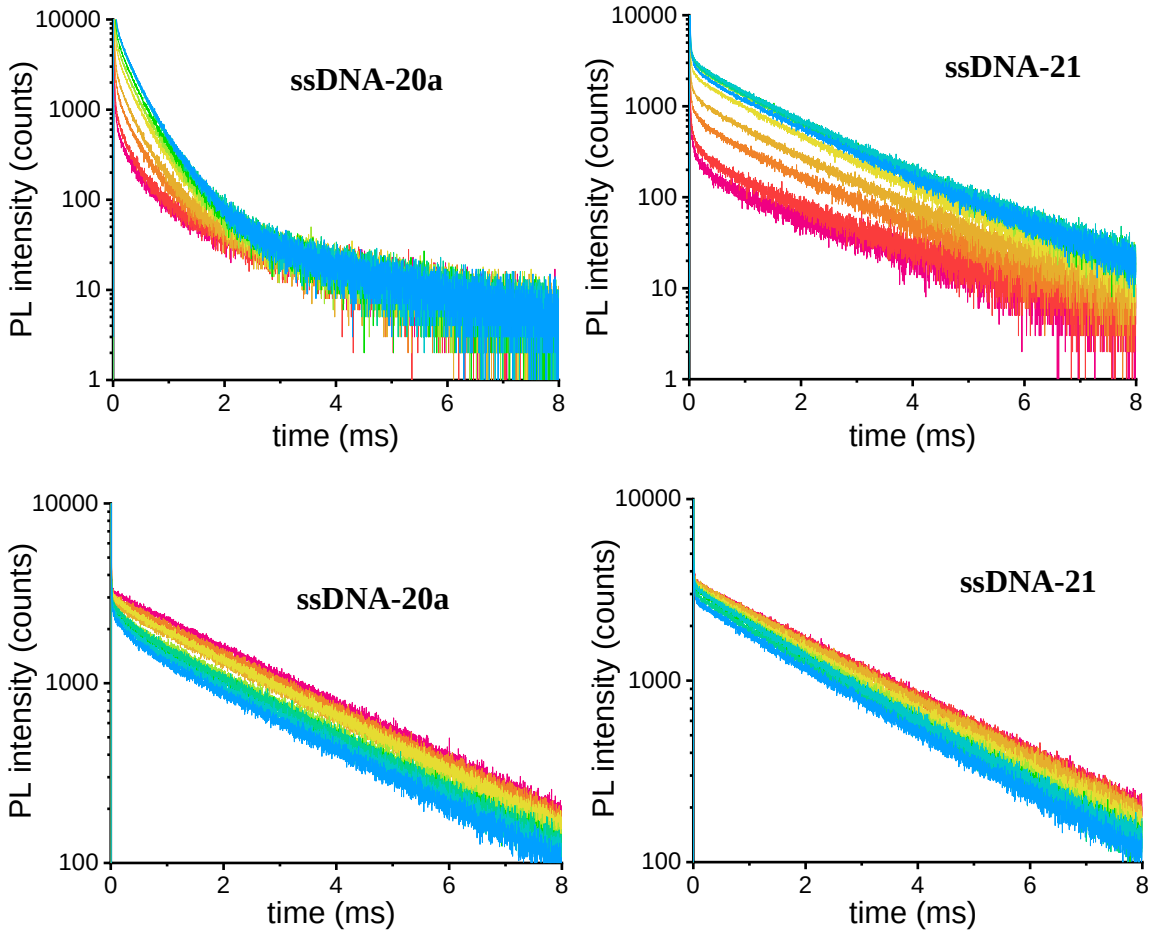

Figure 3.5. PL decay curves of the Cy5.5 FRET acceptor (top) and Tb FRET donor (bottom) for ssDNA-20a (left) and ssDNA-21 (right) detection at increasing target concentrations (0, 0.01, 0.05, 0.1, 0.2, 0.3, 0.4, 0.5, 0.6, and 0.7 nM from pink to blue) and constant hairpin concentrations (2 nM).

3.3.3 PL decay fit results and distance calculations.

Due to the better distinction of FRET-sensitized Cy5.5 PL from Tb background PL (minor contribution of Tb in the Cy5.5 detection channel due to spectral crosstalk) compared to FRET-quenched Tb PL from Tb background PL (strong initial Tb PL signal of pure Tb), only Cy5.5 acceptor decays were considered for distance estimations. Tb donor decays were also fit (see below) but led to less precise results.

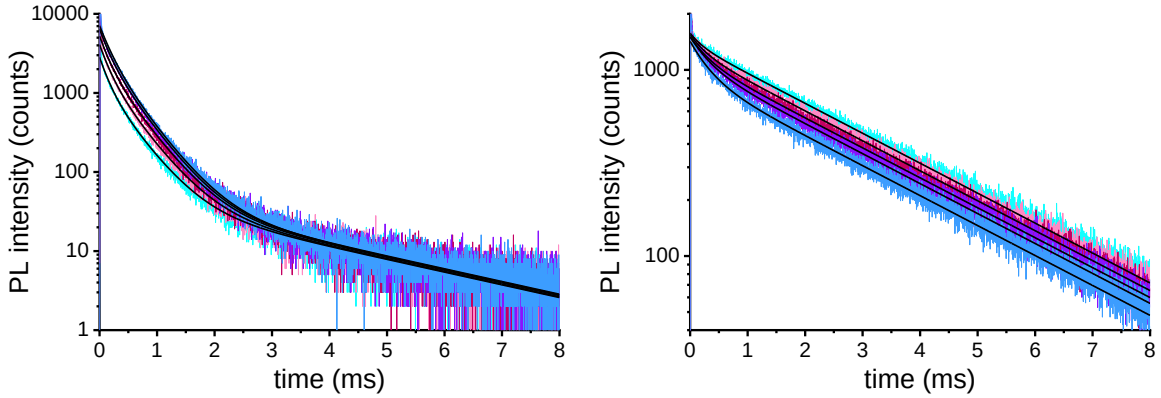

Figure 3.6 PL decay curves of Cy5.5 acceptor (left) and Tb donor (right) used for PL decay time fitting and distance calculation in the **miR-20a** HCR-TG-FRET sensor with the increasing target concentrations (0.2, 0.4, 0.6, 0.8 and 1.0 nM from light blue to blue). Black lines represent the fit results from below. Tb and Cy5.5 are situated at distances of 12 bps from each other in the HCR products of the miR-20a HCR-TG-FRET sensor.

Cy5.5 acceptor channel (3-exponential fit with a contribution of Tb at a constant PL decay time of 2.7 ms, which was fixed, whereas all other fit parameters were variable)

#	miR-20a (nM)
1	0.2
2	0.4
3	0.6
4	0.8
5	1.0
R_0 = 5.8 nm	

τ_D	A_D	τ_{AD1}	A_{AD1}	τ_{AD2}	A_{AD2}	$\langle\tau_{DA}\rangle$	E_{FRET}
2700	50	140	1482	430	1295	358	0.87
2700	51	150	2204	440	1827	363	0.87
2700	53	150	2786	440	2401	365	0.86
2700	55	150	3306	430	3071	360	0.87
2700	54	170	3827	440	3199	361	0.87
				average 1-5		**361**	**0.87**
				distance *r* (nm)		**4.3**	**4.3**

Tb donor channel (2-exponential fit with a contribution of Tb at a constant PL decay time of 2.7 ms, which was fixed, whereas all other fit parameters were variable)

#	miR-20a (nM)
1	0.2
2	0.4
3	0.6
4	0.8
5	1.0
R_0 = 5.8 nm	

τ_D	A_D	τ_{DA1}	A_{DA1}	$\langle\tau_{DA}\rangle$	E_{FRET}
2700	1387	210	188	210	0.92
2700	1263	270	283	270	0.90
2700	1158	310	346	310	0.89
2700	1078	330	429	330	0.88
2700	929	340	495	340	0.87
		average 1-5		**290**	**0.89**
		distance *r* (nm)		**4.1**	**4.2**

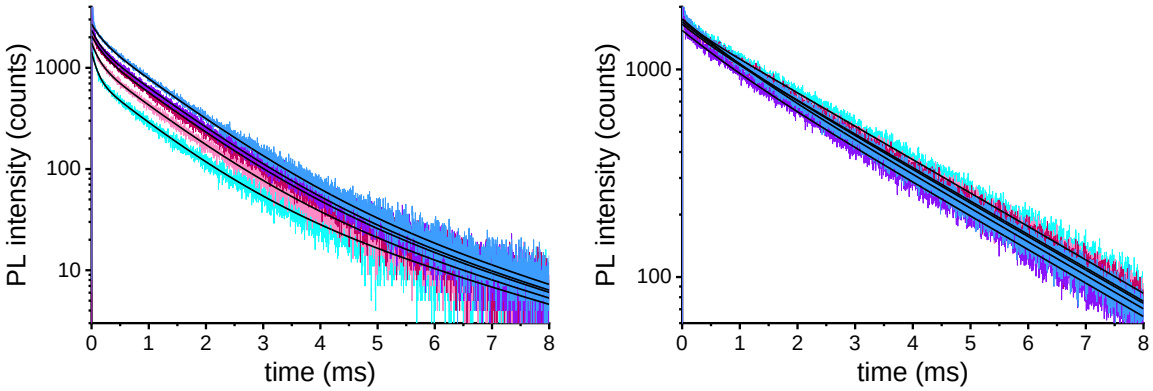

Figure 3.7. PL decay curves of Cy5.5 acceptor (left) and Tb donor (right) used for PL decay time fitting and distance calculation in the **miR-21** HCR-TG-FRET sensor with the increasing target concentrations (0.2, 0.4, 0.6, 0.8 and 1.0 nM from light blue to blue). Black lines represent the fit results from below. Tb and Cy5.5 are situated at distances of 20 bps from each other in the HCR products of the miR-20a HCR-TG-FRET sensor.

Cy5.5 acceptor channel (3-exponential fit with a contribution of Tb at a constant PL decay time of 2.7 ms, which was fixed, whereas all other fit parameters were variable)

#	miR-21 (nM)
1	0.2
2	0.4
3	0.6
4	0.8
5	1.0

τ_D	A_D	τ_{AD1}	A_{AD1}	τ_{AD2}	A_{AD2}	$<\tau_{DA}>$	E_{FRET}
2700	87	100	653	910	687	856	0.68
2700	98	130	641	960	1022	915	0.66
2700	109	170	609	990	1353	949	0.65
2700	113	150	727	1000	1517	961	0.64
2700	128	170	706	1000	1874	966	0.64
				average 1-5		**929**	**0.66**
				distance *r* (nm)		**5.2**	**5.2**

R_0 = 5.8 nm

Tb donor channel (2-exponential fit with a contribution of Tb at a constant PL decay time of 2.7 ms, which was fixed, whereas all other fit parameters were variable)

#	miR-21 (nM)
1	0.2
2	0.4
3	0.6
4	0.8
5	1.0

τ_D	A_D	τ_{DA1}	A_{DA1}	$<\tau_{DA}>$	E_{FRET}
2700	1617	320	120	320	0.88
2700	1479	560	172	560	0.79
2700	1446	750	246	750	0.72
2700	1248	880	294	880	0.67
2700	1360	850	391	850	0.69
		average 1-5		**670**	**0.75**
		distance *r* (nm)		**4.8**	**4.8**

R_0 = 5.8 nm

3.3.4 Duplexing HCR-FRET assay Development and Sensitivity.

Sensitivity and Specificity

The diagnostics performance of the miR-20a and miR-21 HCR-TG-FRET assays was evaluated on a clinical fluorescence plate reader (KRYPTOR) concerning sensitivity and specificity. The assay calibration curves (**Figure 3.8A and B**) showed linearly increasing time-gated FRET ratios (intensity ratio of Cy5.5 and Tb PL in a time window from 0.1 to 0.9 ms after the excitation pulse) with increasing concentrations from 0.005 nM to 0.3 nM for miR-20a and from 0.005 nM to 0.25 nM for miR-21. This linear dynamic range can be further increased by increasing the hairpin concentrations (**Figure 3.9**). Even higher concentration may be quantified by using the automatic dilution mode of the KRYPTOR system. The calibration curves, which show the target concentrations in the 140 µL detection volumes in the 96-well microtiter plates, revealed LODs (standard deviation was calculated for 30 independent background measurements, which contained all assay components but no miRNA target) of 2.8 pM (390 attomoles) of miR-20a and 1.7 pM (240 attomoles) of miRNA-21. The sensitivities were (1.64±0.02) x 10^{-4} F_R/pM for miR-20a and (5.7±0.1) x 10^{-5} F_R/pM for miR-21. Taking into account the rather small standard deviations (*e.g.*, background standard deviations of 1.3 x 10^{-4} F_R for miR-20a and 7.7 x 10^{-5} F_R for miR-21) and the excellent fit of the data points to the linear calibration curves, this sensitivity allows to distinguish concentration differences of a few pM over the entire dynamic concentration range. The LODs of miRNAs equivalent ssDNAs are also shown in **Figure 3.10**.

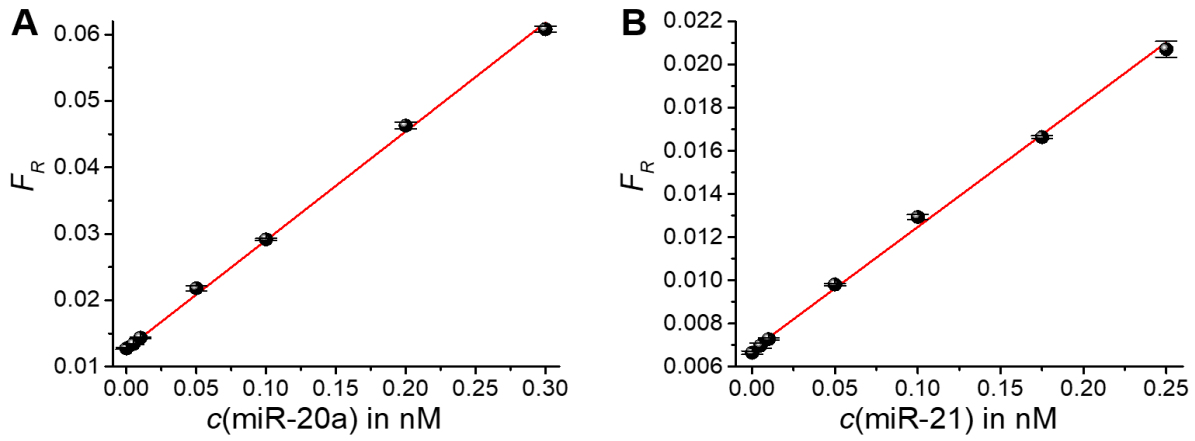

Figure 3.8. Assay calibration curves (**A** for miR-20a and **B** for miR-21) showed a linearly increasing FRET ratio over target concentration with LODs of 2.8 pM (390 attomoles) of miR-20a and 1.7 pM (240 attomoles) of miRNA-21. Error bars present standard deviations from 30 measurements for background (no target, c = 0) and 9 measurements for all other data points.

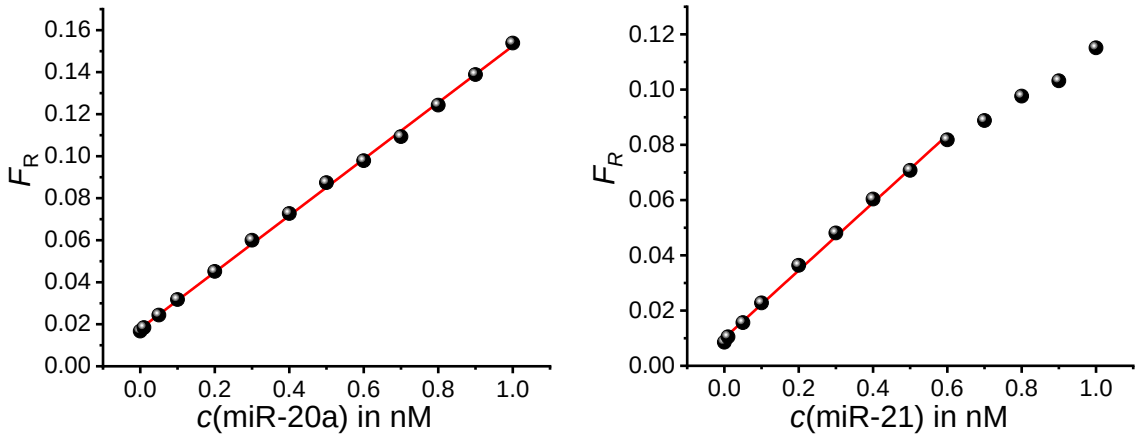

Figure 3.9. HCR-TG-FRET assay calibration curves for miR-20a (left) and miR-21 (right) at 5 nM concentrations of hairpins.

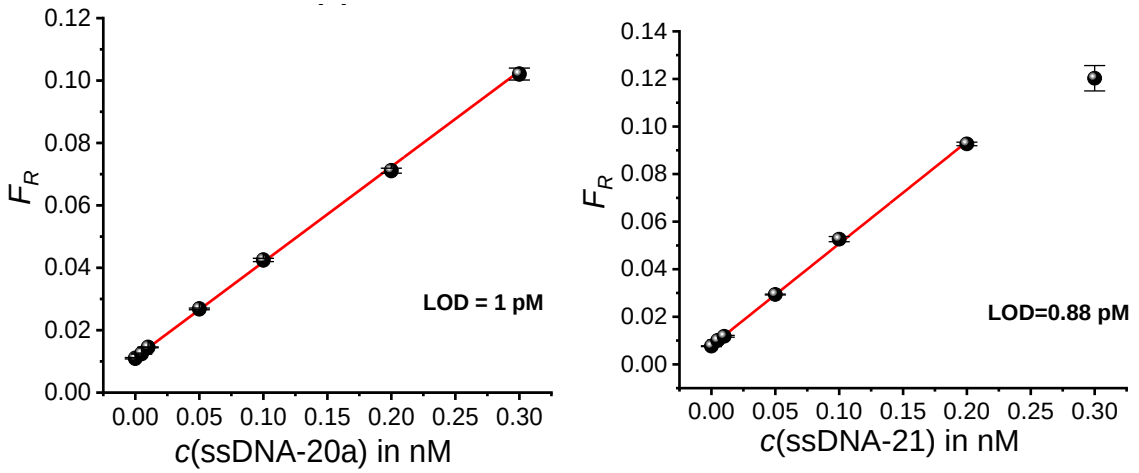

Figure 3.10. Diagnostic performance evaluation of the single **ssDNA** sensors. Assay calibration curves (**A** for ssDNA-20a and **B** for ssDNA-21) showed a linearly increasing FRET ratio over target concentration with LODs of 1.0 pM (140 attomoles) of DNA-20a and 0.88 pM (123 attomoles) of DNA-21. Error bars present standard deviations from 30 measurements for background (no target, $c = 0$) and 9 measurements for all other data points.

The target specificity of HCR-TG-FRET was evaluated for miR-20a and miR-21 (**Figure 3.11**) against each other and against miR-20b, which possesses only two nucleotide mismatches (one at the 5' terminus and the other in the center) compared to miR-20a (*cf.* **Table 3.1**). Both sensors (for miR-20a and miR-21) showed concentration-dependent increasing FRET ratios exclusively for their target, whereas the other two targets led to background signal over the entire concentration range. Only at the highest concentration of miR-20b (1 nM), the miR-20a sensor showed a minor increase in the FRET ratio compared to the background signal. Overall, HCR-TG-FRET quantification of miRNA provided excellent performance concerning sensitivity and specificity.

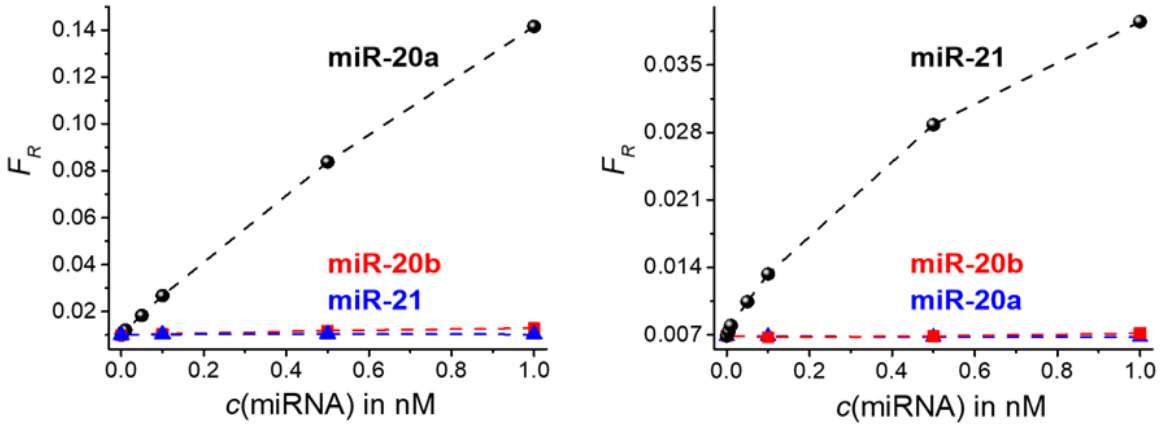

Figure 3.11. Target specificity for miR-20a (left) and miR-21(right) was demonstrated against two different miRNA targets.

Single FRET-Pair Multiplexing

TG multiplexing from a single measurement requires the efficient distinction of different TG detection windows. We selected two TG windows and recorded calibration curves for both miRNA targets (**Figure 3.12A and B**), whose slopes are required for quantification of both targets from the same sample (**Equation 3.4**). The background-corrected FRET ratios of both TG windows for both targets increased linearly until 0.15 nM for miR-20a and 0.30 nM for miR-21. Due to the faster PL decay of the Tb-Cy5.5 FRET pair in the miR-20a HCR-TG-FRET sensor, the PL intensity in the second TG window (TG_2) is almost exclusively dependent on miR-21 concentration. On the other hand, the miR-21 sensitivity in TG_2 (slope of the blue calibration curve in **Figure 3.12B**) is *ca.* four times lower than the miR-20a sensitivity in TG_1 (slope of the green calibration curve in **Figure 3.12A**). Taking into account the *ca.* two-fold lower sensitivity of miR-21 compared to miR-20a in TG_1 (slopes of the green calibration curves in **Figure 3.12A and B**), it can be expected that miR-20a can be measured with higher precision in a duplexed assay. Such considerations are important for multiplexed assay design because different targets often require different sensitivities for diagnostic evaluation.

A first experiment to demonstrate duplexed quantification of miR-20a and miR-21 from the same sample by a single measurement consisted in mixing both targets at the same increasing concentrations that were used for the single sensor assays (0 to 0.15 nM for miR-20a and 0 to 0.3 nM for miR-21). As expected, the PL decay curves presented a multiexponential convolution of the single curves and the FRET ratios increased in both TG detection windows (**Figure 3.12C**). The almost perfect overlap of the detected FRET ratios and the sum of the

single assay FRET ratios (**Figure 3.12C**, right) showed that a combination of duplexed FRET ratios and the slopes of the single assay calibration curves (**Equation 3.4**) should be applicable to simultaneously quantify different concentrations of miR-20a and miR-21 from the same sample. To verify this finding, we prepared 13 samples that contained both targets at different concentrations ranging from high miR-20a and low miR-21 to low miR-20a and high miR-21. Decay and calibration curves for DNA targets are shown in **Figure 3.14**.

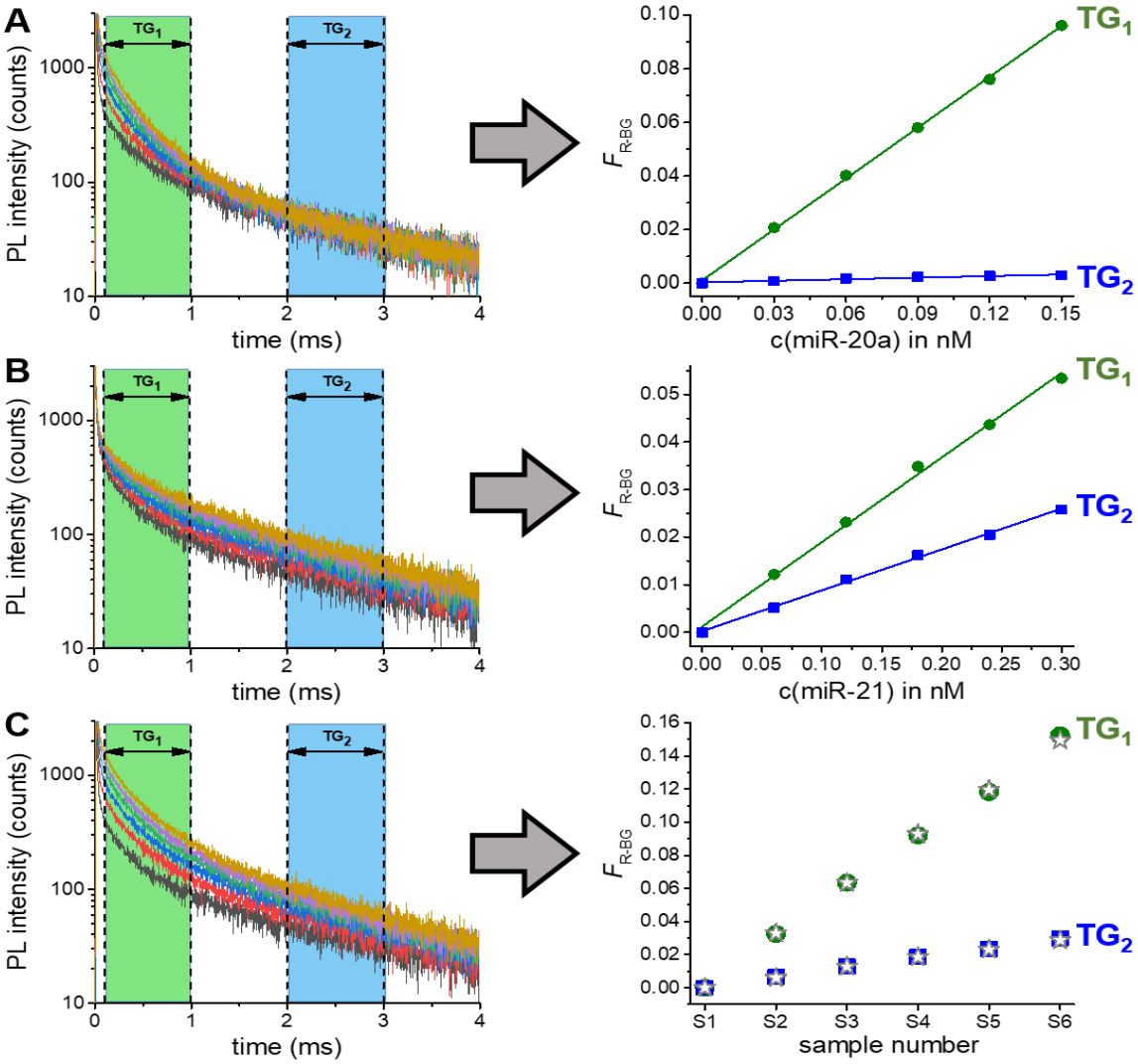

Figure 3.12. PL decay curves of FRET-sensitized Cy5.5 and corresponding FRET-ratios (right) determined from the TG PL intensities in the two TG detection windows. **A**: miR-20a, **B**: miR-21, **C**: miR-20a and miR-21. Stars in C present the mathematical sum of the FRET ratios from the single miRNA-target assays in A and B. The overlap with the measured duplexed FRET ratios shows the applicability of the calibration curves from A and B to duplexed miRNA quantification in C.

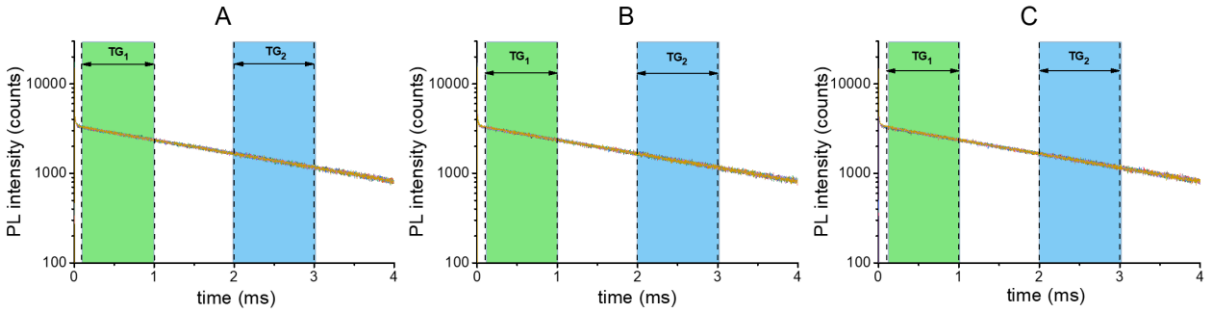

Figure 3.13. PL decay curves of Tb corresponding the Cy5.5 PL decay curves shown in Figure 3.12. **A**: miR-20a, **B**: miR-21, **C**: miR-20a and miR-21. Same concentrations as in Figure 3.12.

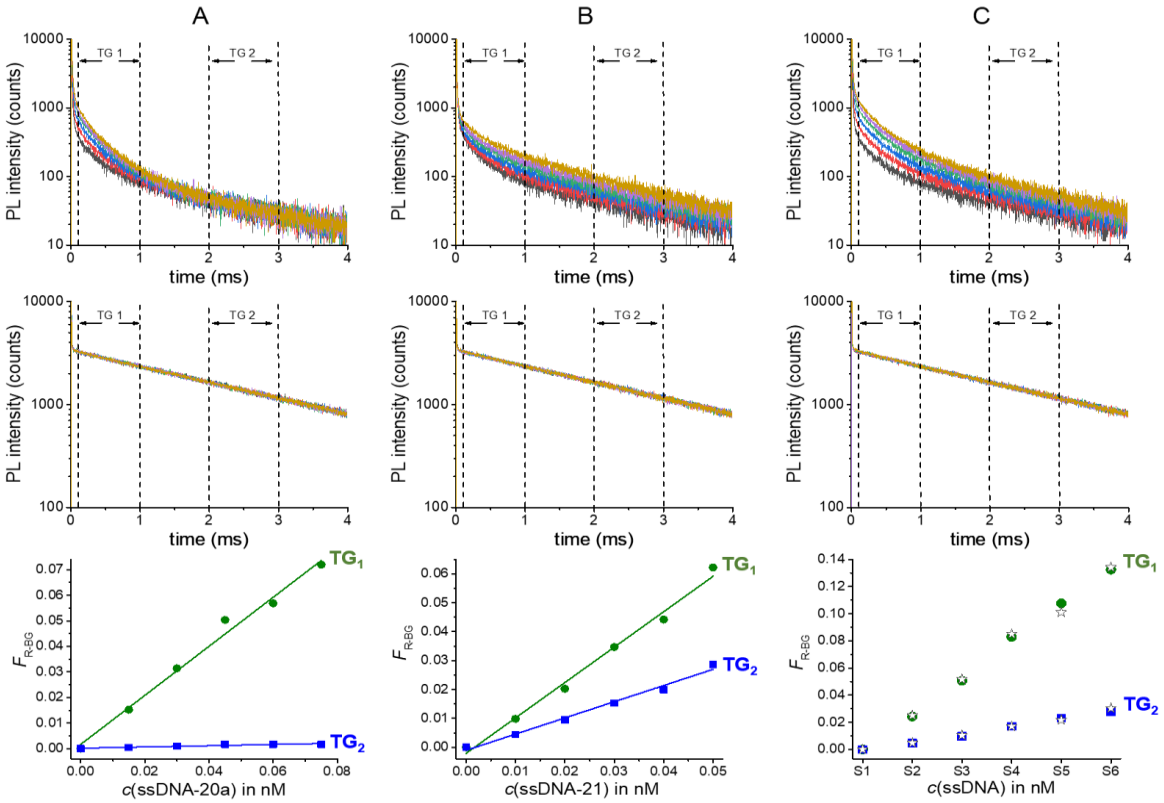

Figure 3.14. PL decay curves of FRET-sensitized Cy5.5 (top) and FRET-quenched Tb (middle), and corresponding FRET-ratios (bottom) determined from the TG PL intensities in the two TG detection windows. **A**: ssDNA-20a, **B**: ssDNA-21, **C**: ssDNA-20a and ssDNA-21. Stars in C present the mathematical sum of the FRET ratios from the single miRNA-target assays in A and B. The overlap with the measured duplexed FRET ratios shows the applicability of the calibration curves from A and B to duplexed miRNA quantification in C.

As shown in **Figure 3.15**, both miRNA targets could be quantified at varying concentrations between 30 pM and 300 pM with relatively high precision. The performance of HCR-TG-FRET was not compromised by the addition of serum (10 %) inside the sample and RNase inhibitors were not required. As expected, due to the lower sensitivity of the miR-21 sensor, the precision of miR-21 quantification was lower. However, all experimentally

determined data points are still very close to the known concentrations. Taking into account that all measured miR-21 concentrations have a slightly less steep linear correlation with the actual concentrations (as visualized by the blue dashed lines in **Figure 3.15**), this deviation may even be correctable in case a higher accuracy should be required. Duplexed detection of DNA targets in buffer is shown in **Figure 3.16**.

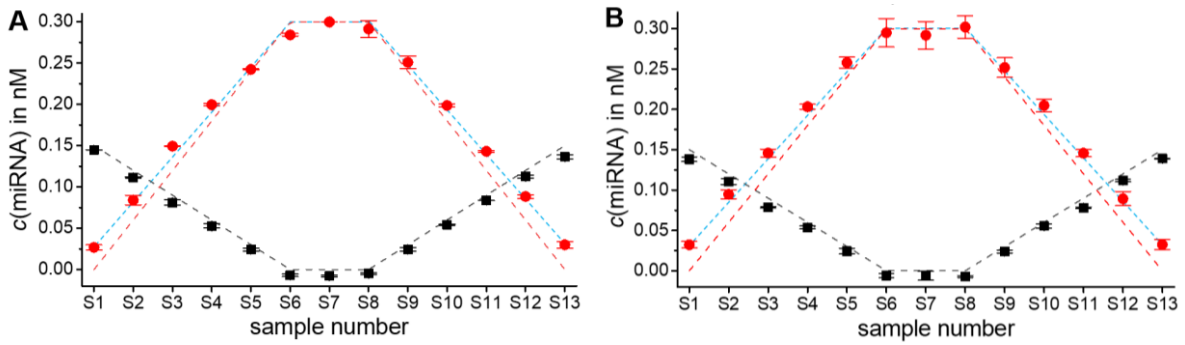

Figure 3.15. Duplexed HCR-TG-FRET quantification of miR-20a (black) and miR-21 (red) at varying concentrations in buffer (**A**) and in buffer containing 10% serum (**B**). Dashed lines represent known concentrations. Data points were determined by HCR-TG-FRET using the calibration curves from **Figure 3.12** and **Equation 3.4**. Light blue dashed shows the slope of the red data points, which may be used for further improving the precision for miR-21.

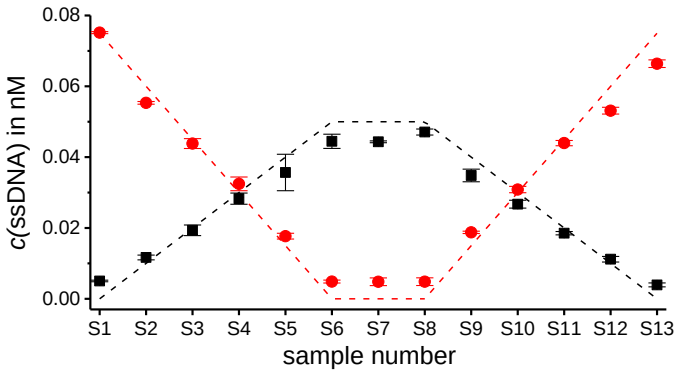

Figure 3.16. Duplexed HCR-TG-FRET quantification of ssDNA-20a (black) and ssDNA-21 (red) at varying concentrations. Dashed lines represent known concentrations. Data points were determined by HCR-TG-FRET using the calibration curves from **Figure 3.13** and **Equation 3.4**.

3.4. Conclusion

HCR is a very simple signal amplification strategy because it does not require any enzymes. Therefore, it is a frequently applied technique for sensitive nucleic acid detection. Although HCR has been significantly optimized since its first application in 2004, we showed that

simplicity, sensitivity, and multiplexing can be further improved by implementation of TG-FRET into HCR. Because FRET can only occur in the HCR product and not in the free hairpin probes, HCR-TG-FRET does not require any washing or separation steps (simplicity improvement). The TG detection of Tb donor and Cy5.5 acceptor with long PL decay times allowed for efficient suppression of sample autofluorescence and of directly excited acceptor fluorescence, which leads to high signal-to-background ratios (sensitivity improvement). Using different TG detection windows enabled multiplexed detection of different targets from the same sample by a single measurement, single excitation wavelength, and single detector (multiplexing and simplicity improvement). We applied HCR-TG-FRET to both miRNA (miR-20a and miR-21) and the analogous ssDNA targets and demonstrated very low LODs (down to 240 attomoles of miRNA and 123 attomoles of ssDNA) with high sensitivities. High specificity was verified against other targets including very homologous miRNAs (miR-20a *vs.* miR-20b). Single-measurement multiplexing was demonstrated by simultaneous quantification of miR-20a and miR-21 at different concentrations (between 30 pM and 300 pM) from the same sample with similar results for serum-free buffer and buffer containing 10% of serum without the use of RNase inhibitors. Our detailed analytical evaluation revealed the versatile and powerful diagnostic performance of HCR-TG-FRET even in challenging biological environments. Taking into account that the temporal multiplexing approach is not limited to two TG detection windows and that it can be combined with spectral distinction for higher order multiplexing, we expect that HCR-TG-FRET will become a very useful alternative to currently applied HCR approaches for advanced multiplexed nucleic acid detection both in solution and *in situ*.

Contributions

For this work, I designed the studies, performed the experiments, analyzed the data, and wrote the manuscript.

4. Spectral-temporal quadruplexing Tb-Dye RCA-FRET ssDNA detection assay

4.1 Introduction

In this chapter, I will present another nucleic acid detection method that combines the spectral-temporal quadruplexing Tb-Dye time-gated FRET (TG-FRET) with sensitivity and specificity of target-primed RCA. Although a combination of spectral and temporal multiplexing within a single biosensing technique may seem evident, an actual experimental realization is very complicated and such a method is not available. One of the main reasons is the third dimension of the intensity, which is required for quantifying the analytes. For each biological target or interaction, a three-dimensional PL biosensor must provide a specific and stable spectral-temporal signal combination that is independent of the other targets and the environment and changes its intensity as a function of target concentration. This objective becomes even more challenging when extremely low concentrations (fM-pM) of various similar targets need to be specifically quantified.

Low abundance of nucleic acids often necessitates their amplification. A well-known and highly specific isothermal amplification method is target-primed rolling circle amplification (RCA), in which a padlock-DNA circularization by ligation over DNA[157] or RNA[158] targets enables the amplification process. In contrast to PCR, target-primed RCA can be applied both *in situ*, *e.g.*, for genotyping individual DNA or mRNA molecules[159], and in solution, *e.g.*, for DNA[160] or micro-RNA (miRNA)[161] diagnostics. As FRET and the involved PL lifetimes are strongly distance dependent, RCA amplification strategies could be ideally suited for controlled PL lifetime tuning by precise adjustment of donor-acceptor distances within the amplified DNA sequence at sub-nanometer resolution. The separation-free and background-free assay format accomplished limits of detection between 40 and 570 zeptomoles (0.3 to 4.1 fM) for four different DNA targets from the same sample, using a single excitation source and only two distinct fluorescence colors.

4.2 Materials and methods

4.2.1 Nucleic acid probes and exogenous targets.

All sequences and modifications of nucleic acids are summarized in **Table 4.1**. All oligonucleotides (including Cy3.5 and Cy5.5 functionalized DNA) were purchased from Eurogentec. Non-modified DNAs were purified with cartridge gold-desalting method. Phosphate DNAs were purified with polyacrylamide gel electrophoresis. All other modified DNAs were purified with HPLC. Lumi4-Tb-NHS (Tb-NHS) was provided by Lumiphore, Inc. Tb-DNA conjugation was performed as described in **3.2.1**.

Table 4.1 Sequences and modifications of all DNA probes and targets. Sequence differences are shown in red, target-specific termini of padlock DNA shown in blue, Tb-probe-complementary sequences shown in green, and Cy3.5 and Cy5.5-probe-complementary sequences shown in orange.

Probe	Sequence 5'-3'	Modification
DNA-20a	TAAAGTGCTTATAGTGCAGGTAG	/
DNA-20b	CAAAGTGCTCATAGTGCAGGTAG	/
DNA-21	TAGCTTATCAGACTGATGTTGA	/
DNA-191	CAACGGAATCCCAAAAGCAGCTG	
padlock-20a	AAG CAC TTT AAT ATA TGA TGG TCG CAA CAA GCT CAC GGT GAT GCC GAA TTT TTC AAG AGG AAA TGT CTA CCT GCA CTA T	5′- Phosphate
padlock-20b	GAG CAC TTT GAT ATA TGA TGG ACC GCT ACG ATC AGC TGG AAT CAA GGT AAC GGA CTG AGG AAA TGT CTA CCT GCA CTA T	5′- Phosphate
padlock-21	TGA TAA GCT AAT ATA TGA TGG AAT CAA GAC AAT ATT GTT GAT GCC GAA TTT TTC AAG AGG AAA TGT TCA ACA TCA GTC	5′- Phosphate
padlock-191	TGG GAT TCC GTT GAT ATG ATC CGG CAA CGG TCG AGT GCG CAT AAT CAA GGT AAC GCA CTG AGG AAA TGT CAG CTG CTT T	5′- Phosphate
Tb probe 20a	AGCTCACGGT	5′- C3 amino
Tb probe 20b	CGATCAGCTGG	5′- C3 amino
Tb probe 21	AATCAAGACAATATTGTT	5′- C6 amino
Tb probe 191	CAACGGTCGAGTGCGCAT	5′- C3 amino
Cy3.5 probe 20a/21	GATGCCGAATTTTTCAAGAG	5′- Cy3.5
Cy5.5 probe 20a/21	GATGCCGAATTTTTCAAGAG	5′- Cy5.5
Cy3.5 probe 20b/191	AATCAAGGTAACGGACTGAG	5′- Cy3.5
Cy5.5 probe 20b/191	AATCAAGGTAACGGACTGAG	5′- Cy5.5

4.2.2 Photophysical analysis

Absorption spectra (Lambda 35 UV/Vis System, PerkinElmer) and emission spectra (FluoTime 300, PicoQuant) were recorded in HEPES buffer (100 mM, pH 7.4) and deionized water (purified by Purelab Option-Q equipped with bio-filter, ELGA LabWater) for Tb, Cy3.5, and Cy5.5 samples, respectively.

4.2.3 RCA-FRET single target assays

In a typical DNA assay, 0.75 nM padlock probe and an appropriate amount of target DNA were prepared in 20 µL *Taq* DNA ligase reaction buffer (BUFFER-1, 1× buffer components:

20 mM Tris-HCl, 25 mM potassium acetate, 10 mM magnesium acetate, 10 mM dithiothreitol, 1 mM NAD, 0.1% Triton X-100, pH 7.6) and incubated in a thermal cycler with a temperature control program (80°C for 2 min → decreased from 80°C to 22°C with a 2°C/min speed). Then 4 U of *Taq* DNA ligase (New England Biolabs) prepared in 10 µL BUFFER-1 was added to the mixture and incubated at 37°C for 1 h. Afterwards, 60 µL phi29 DNA polymerase reaction buffer (BUFFER-2, 1× buffer components: 50 mM Tris-Cl, 10 mM $MgCl_2$, 10 mM $(NH_4)_2SO_4$, 4 mM DTT, pH 7.4), which contained 5 U of phi29 DNA polymerase (New England Biolabs) and 0.5 mM dNTP (New England Biolabs), was added and incubated at 37°C for 2 h. Before termination of the polymerization process, 5 nM Tb probe and 5 nM Cy3.5 or Cy5.5 probe prepared in 60 µL hybridization buffer (BUFFER-3, 20 mM Tris-Cl, 500 mM NaCl, 0.1 % BSA, pH 8.0) were added and incubated in a thermal cycler with a temperature control program (65°C for 10 min → decreased from 65°C to 22°C with a 2°C/min speed → 22°C for 10 min). From the total reaction volume of 150 µL, 140 µL were measured in black 96-well microtiter plates on the clinical immunofluorescence plate reader KRYPTOR compact plus (Thermo Fisher Scientific) with time-gated (0.1-0.9 ms) PL intensity detection using optical bandpass filters with 494±12 nm (Semrock) for the Tb detection channel, 716±20 nm (Semrock) for the Cy5.5 detection channel and 608±4 nm (Delta) for the Cy3.5 detection channel. For ratiometric analysis, FRET-ratios were calculated by the ratio of Cy5.5 or Cy3.5 and Tb time-gated PL intensities. Trizma base, hydrochloric acid (HCl) and bovine serum albumin (BSA) were purchased from Sigma-Aldrich. NaCl was purchased from Duchefa. All chemicals were used as received.

4.2.4 Temporal duplexing of DNA-20a and DNA-21

The duplexed assay contained two different padlock probes (same amounts as single sensors), *Taq* DNA ligase (double amounts of single sensors), phi29 DNA polymerase and dNTP (same amounts as single sensors), two different Tb probes (same amounts as single sensors) and Cy5.5 probe (double amounts of single sensors). 140 µL were measured in black 96-well microtiter plates on a fluorescence plate reader (Edinburgh Instruments) using 4000 detection bins of 2 µs integration time and nitrogen laser (MNL 100, LTB Berlin) excitation (337.1 nm, 20 Hz) and using optical bandpass filters with 494±12 nm for the Tb detection channel and 716±20 nm for the Cy5.5 detection channel.

4.2.5 Spectral-temporal multiplexing of DNA-20a, DNA-21, DNA-20b, and DNA-191

The quadruplexed assay contained four different padlock probes (same amounts as single sensors), *Taq* DNA ligase (quadruple amounts of single sensors), phi29 DNA polymerase and dNTP (double amounts of single sensors), four different Tb probes (same amounts as single sensors), Cy3.5 probe (double amounts of single sensors) and Cy5.5 probe (double amounts of single sensors). 140 µL were measured in black 96-well microtiter plates on a fluorescence plate reader (Edinburgh Instruments) using 4000 detection bins of 2 µs integration time and nitrogen laser (MNL 100, LTB Berlin) excitation (337.1 nm, 20 Hz) and using optical bandpass filters with 494±12 nm for the Tb detection channel, 608±4 nm for the Cy3.5 detection channel and 716±20 nm for the Cy5.5 detection channel.

4.3 Results and discussion

4.3.1 The principle of multiplexed RCA-FRET

The principle of multiplexed RCA-FRET is shown in **Figure 4.1**. First, a DNA target is specifically hybridized by the two ends of a linear probe DNA (padlock DNA) that circularizes upon target recognition. Then, the padlock nick is ligated over the target splint, which makes the target a primer for a polymerase to synthesize complementary DNA around the circular probe DNA. After each round, the previously synthesized DNA strand is displaced, which leads to a long ssDNA concatemer. As the repetitive sequence of this long RCA product is known (by the design of the padlock), FRET-donor (Tb) and FRET-acceptor (Cy3.5 or Cy5.5) DNA probes can be designed to hybridize at desired positions within the concatemer and thereby at defined but distinct donor-acceptor distances (R). Due to the strong distance-dependence of the FRET efficiency ($\sim R^{-6}$), different values of R lead to different PL decays of the FRET-quenched donors and FRET-sensitized acceptors (the closer the distance the faster the decay).[3], [46] These different PL decays can then be used for straightforward temporal multiplexing by time-gated PL intensity detection. The use of two different acceptors (Cy3.5 and Cy5.5) for the same Tb donor allows for spectral multiplexing with a single excitation wavelength. In principle, x distinct spectral signals and y distinct temporal signals can be combined to $x \cdot y$ distinct signals in solution or x^y distinct signals if the different RCA products are spatially separated (*e.g.*, *in-situ* imaging). Such higher-order multiplexing has the potential to significantly advance the detection of multiple targets from a single sample. Another advantage is the separation-free format of RCA-FRET because FRET is not possible for Tb and dye DNA probes that are free in solution (not hybridized to the RCA product). Finally, the ratiometric detection of time-gated

PL intensities of dye and Tb leads to very precise (low coefficients of variation) signal quantification.

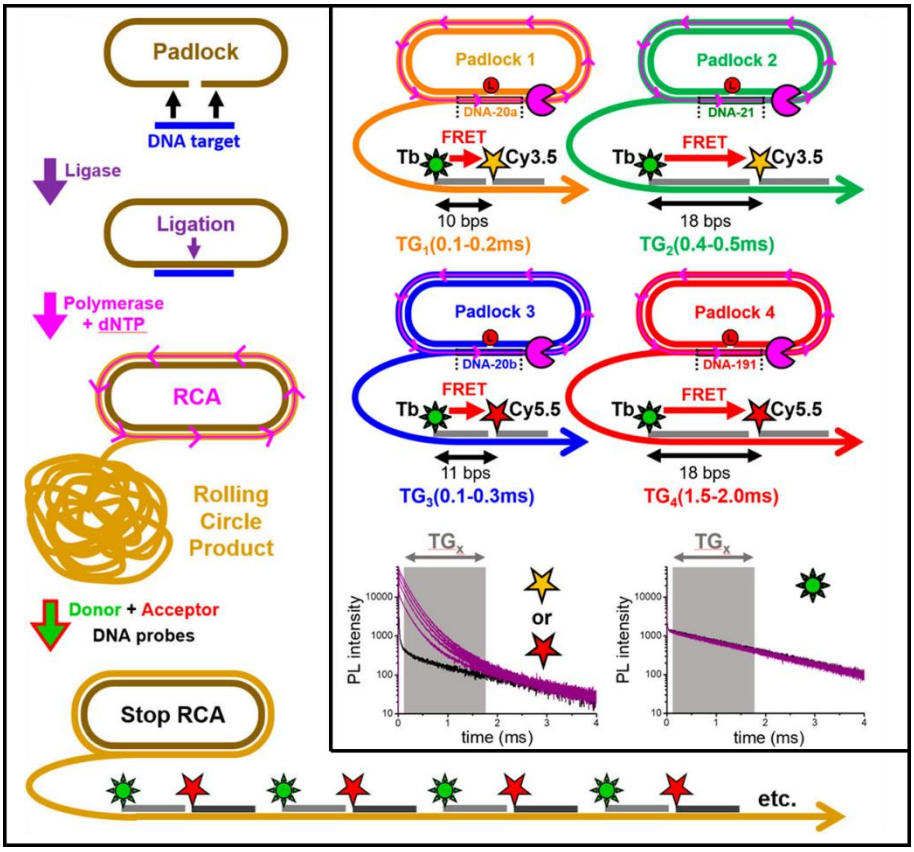

Figure 4.1. Each DNA target is recognized by the terminal sequences of a specific padlock probe. After this hybridization step, a ligase (Taq DNA ligase) closes the padlock nick over the target splint, which transfers the target into a primer for subsequent DNA synthesis (by phi29 DNA polymerase and dNTP, a mixture of the four deoxyribonucleotides). DNA amplification by RCA is performed at 37 °C for 2 h, and the resulting rolling circle product is labeled (specific hybridization) by Tb-donor and dye-acceptor DNA probes. Combining the same Tb donor with two different dye acceptors (Cy3.5 and Cy5.5) and hybridizing the DNA probes at different distances (bps: base pairs) inside of the target specific RCA products provides four distinguishable signals (two distinct time-gated detection windows TG1-TG4 for two different colors) in the two Cy3.5 and Cy5.5 detection channels. Ratiometric TG-FRET measures the FRET-ratio of the FRET-sensitized dye PL intensity (left) and FRET quenched Tb PL intensity (right) within a specific time window after pulsed excitation (to suppress autofluorescence). Black/purple decay curves present signals without/with a target. The FRET-sensitized dye-acceptor intensity strongly increases with increasing target concentration, whereas the overall Tb-donor signal is not significantly quenched (because also free Tb DNA probes in solution emit PL).

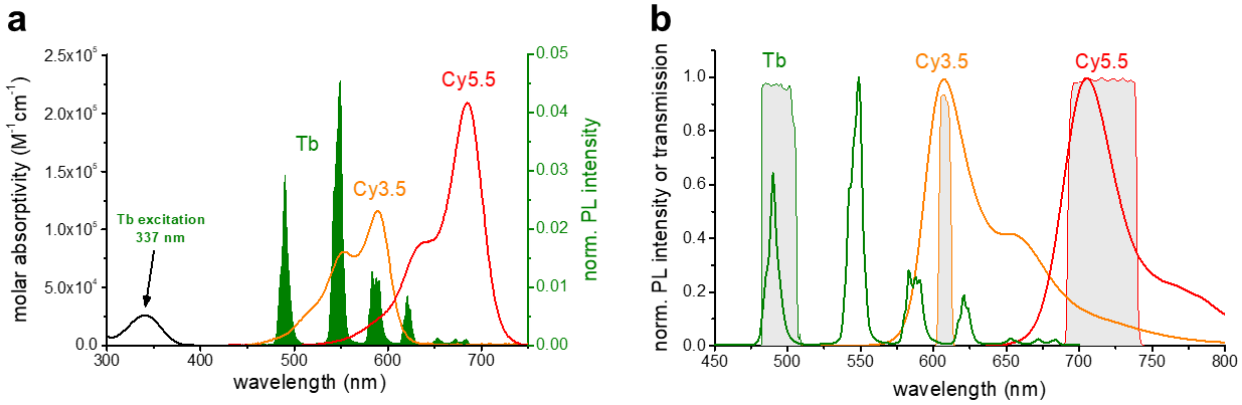

Figure 4.2. (a) Spectra of Tb absorption (black) and emission (green) that partly overlaps with the absorption of Cy3.5 (orange) and Cy5.5 (red). (b) Emission spectra of Tb (green), Cy3.5 (orange), and Cy5.5 (red). Optical bandpass filter transmission spectra, which represent the detection channels for Tb, Cy3.5, and Cy5.5, are shown in gray.

Absorption/emission spectra of donor LTC, acceptor Cy3.5 and Cy5.5 are shown in **Figure 4.2.** Förster distances (the donor-acceptor distance for which FRET is 50 % efficient) of R_0(Cy3.5) = 6.5 ± 0.3 nm and R_0(Cy5.5) = 5.8 ± 0.2 nm were calculated using **Equation 4.1**. The orientation factor κ^2 was taken as 2/3 because of the random orientation of donor and acceptor during the FRET time (dynamic averaging), which is well justified by the long PL lifetime of the Tb donors and the unpolarized emission (fast isotropic rotation). The refractive index was $n = 1.35$ (aqueous buffer solution). The Tb-centered quantum yield was $\Phi_D = 0.80 \pm 0.05$. The overlap integral J was calculated by **Equation 4.2** where $I_D(\lambda)$ is the emission intensity from the area-normalized (to unity) emission spectrum of Tb donor and $\varepsilon_A(\lambda)$ is the molar absorptivity of the acceptor.

$$R_0 = 0.02108\left(\kappa^2 \Phi_D n^{-4} J\right)^{1/6} \text{nm} \tag{4.1}$$

$$J = \int_{475\text{ nm}}^{700\text{ nm}} I_D(\lambda)\varepsilon_A(\lambda)\lambda^4 \, \mathrm{d}\lambda \tag{4.2}$$

4.3.2 Spectral-temporal multiplexing RCA-FRET assay development

Sensitivity

As a representative system for multiplexed nucleic acid detection, we selected four different short ssDNAs (DNA-20a, DNA-20b, DNA-21, and DNA-191), which are the DNA-equivalents of the micro-RNAs hsa-mir-20a/20b/21/191, all of which have been found to be related to breast cancer.[154], [162]–[164] Because target-primed RCA via padlock probes was already applied

for longer DNA as well as RNA targets,[157], [159] our short ssDNA-based detection is in principle transferable to other nucleic acids. To evaluate the sensitivity and versatility of RCA-FRET, we quantified the four DNAs at concentrations between 1 and 250 fM and with two different TG-FRET donor/acceptor pairs (Tb/Cy3.5 and Tb/Cy5.5). All eight RCA-FRET sensors showed a linear signal-over-concentration behavior within the tested concentration range (**Figure 4.3** and **Figure 4.4**), which allowed for the distinction of even very similar concentrations, and LODs between 40 and 570 zeptomoles (0.3 to 4.1 fM) of DNA. For statistical analysis and the estimation of LODs, all samples were prepared 3 times and measured in triplicates (n = 9) apart from the zero-concentration samples (without DNA targets), which were prepared 10 times and measured in triplicates (n = 30).

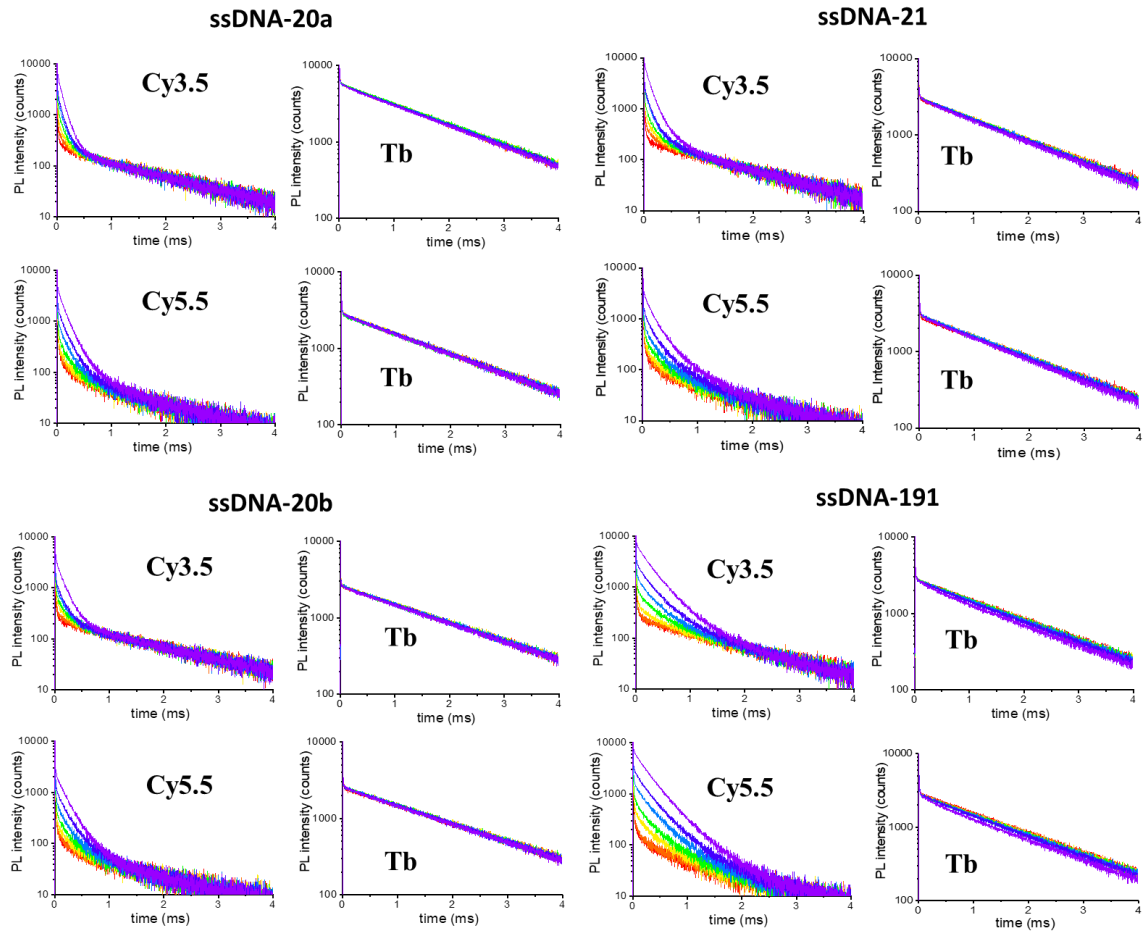

Figure 4.3. PL decay curves measured in the Tb and the dye detection channels for the different DNA targets with increasing concentrations (0, 0.01, 0.025, 0.05, 0.075, 0.1, 0.25 pM). FRET-sensitized dye PL is more obvious than FRET-quenched Tb PL. This is caused by the fact that long-lived dye PL can only be generated by FRET (very low background), whereas the Tb PL is already long-lived (high background).

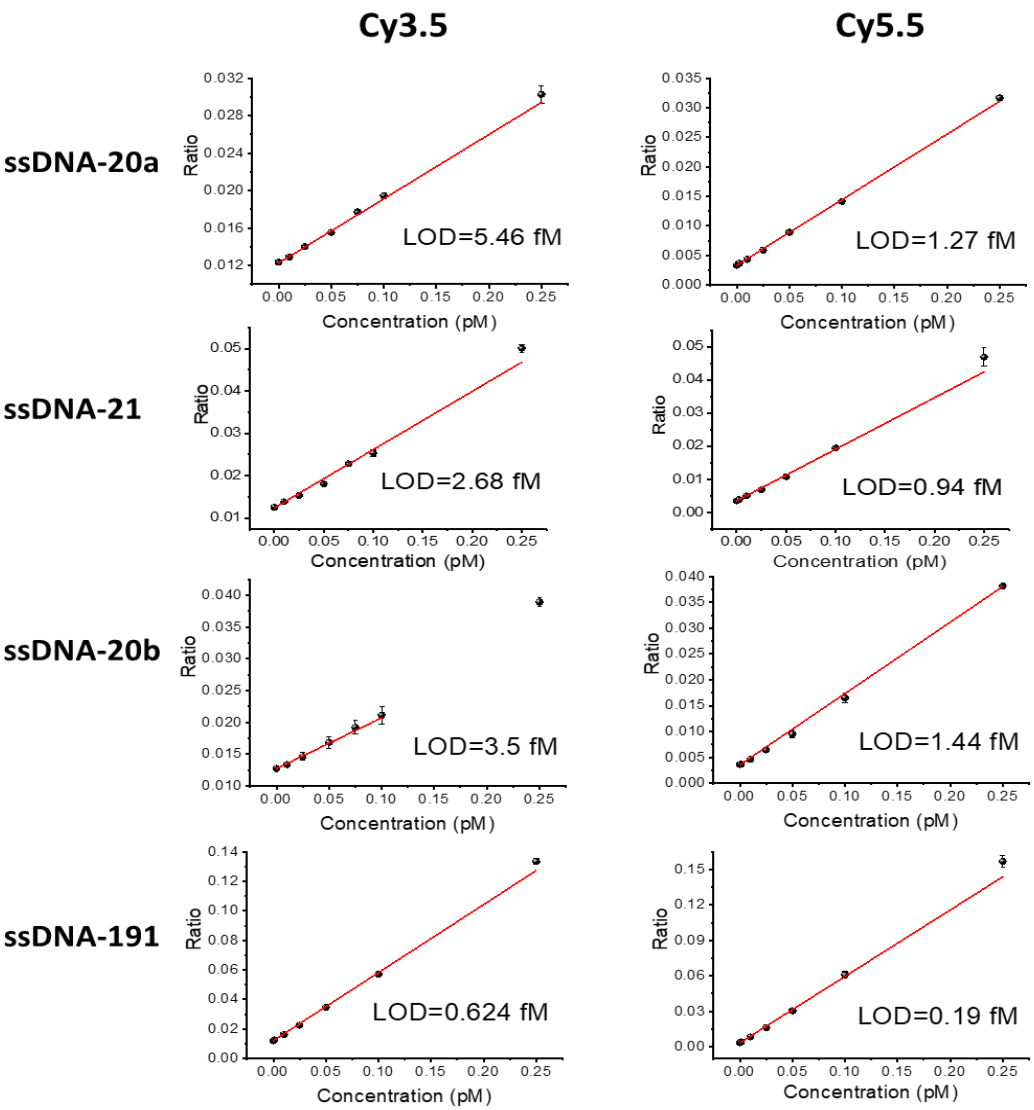

Figure 4.4. RCA-FRET assay calibration curves for four different DNA targets with Cy3.5 or Cy5.5 as FRET acceptor. LODs were 4.1±0.6 fM (Cy3.5) and 1.3±0.2 fM (Cy5.5) for DNA-20a, 2.8±0.4 fM (Cy3.5) and 1.1±0.2 fM (Cy5.5) for DNA-20b, 2.5±0.4 fM (Cy3.5) and 1.2±0.2 fM (Cy5.5) for DNA-21, and 0.8±0.1 fM (Cy3.5) and 0.3±0.1 fM (Cy5.5) for DNA-191.

Specificity

For specificity testing, DNA-20a and DNA-20b had only two nucleotide variations, from which one was at the 5'-terminus. All four sensors provided specificity solely to their respective targets without non-specific background signals from the other three DNAs and with increasing FRET signals over a concentration range of more than three orders of magnitude (**Figure 4.5**).

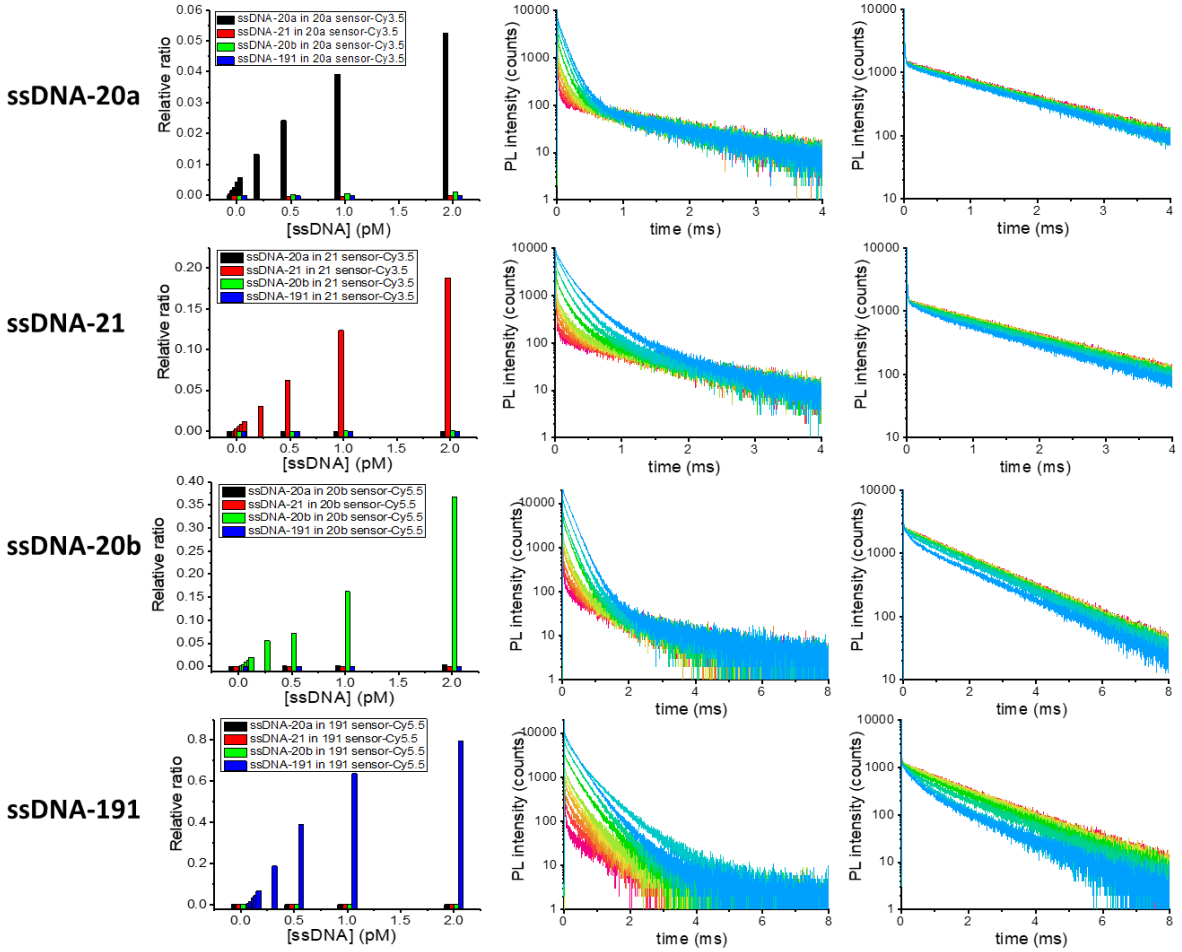

Figure 4.5. Broad dynamic concentration range (0 fM to 2 pM) and high specificity of RCA-FRET demonstrated by the distinction of each DNA target against the other three DNAs. For DNA-20a and DNA-21 the FRET pair Tb/Cy3.5 and for DNA-20b and DNA-191 the FRET pair Tb/Cy5.5 were used.

Temporal duplexing of DNA-20a and DNA-21

To verify the sensitivity and selectivity, temporal duplexing (2-plex) of DNA-20a and DNA-21 were performed. We prepared 13 samples with varying concentrations of DNA-20a and DNA-21, and all samples were prepared 2 times and measured once (n=2). **Figure 4.6** shows that the measured concentrations were in excellent agreement with the actual target concentrations.

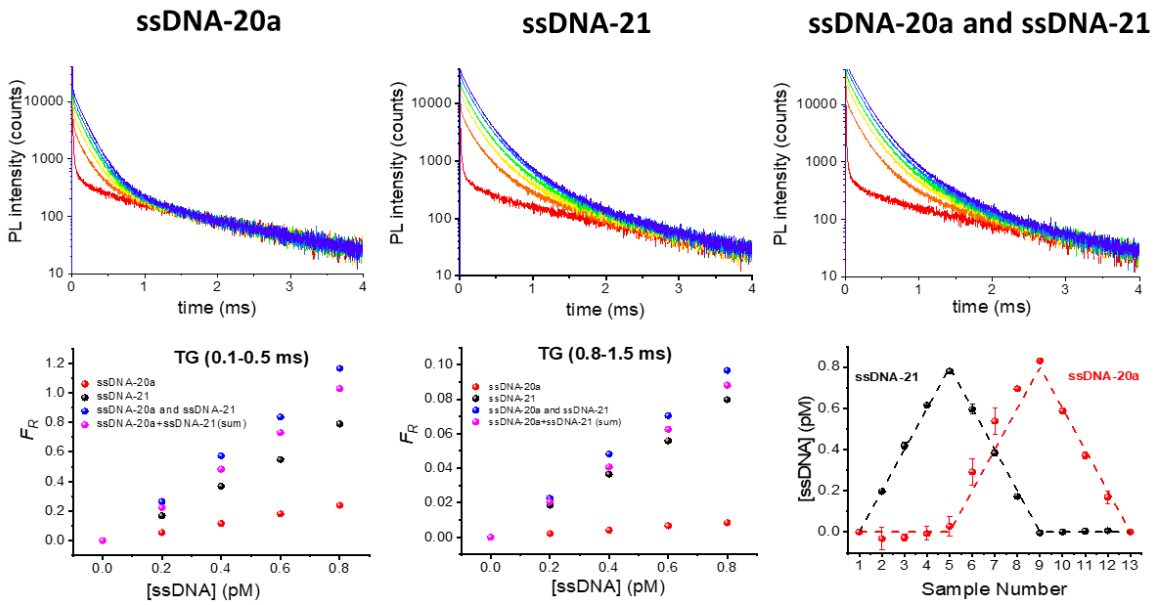

Figure 4.6. PL decay curves (top), calibration curves (bottom left), and recovery tests (bottom right) of varying concentrations of DNA-21, and DNA-20a from 13 different samples using temporal TG-FRET multiplexing. Dotted lines represent known concentrations; data points represent RCA-FRET measurements.

Spectrotemporal multiplexing of DNA-20a, DNA-21, DNA-20b, and DNA-191.

Multiplexing from a single sample is highly important to simultaneously measure various targets, to reduce sample volume and reagents, and to increase the measurement throughput. We have previously shown that Tb-to-dye TG-FRET can be used for efficient and sensitive color multiplexing in immunoassays[16] and miRNA assays (three targets)[7][8] and for temporal multiplexing of two different miRNAs shown in Chapter 3. However, neither the combination of these two concepts into higher-order spectral-temporal TG-FRET multiplexing from a single sample, nor the detection of extremely low concentrations (fM-pM) of biomolecules has been realized. Following the RCA-FRET concept from **Figure 4.1**, we designed four different padlocks and six different FRET probes (four Tb probes and two dye probes), which allowed us to place the two different FRET-pairs at distinct distances within the target-specific RCPs. This, in turn, led to distinct PL decay curves (**Figure 4.7**) due to the different FRET efficiencies. The different decay curves show the contribution of each target into the Cy3.5 (left) or Cy5.5 (right) detection channels and were used to calculate the calibration curves in **Figure 4.8a**. All PL signals were generated by using a single excitation source because the same Tb donor was used in all cases.

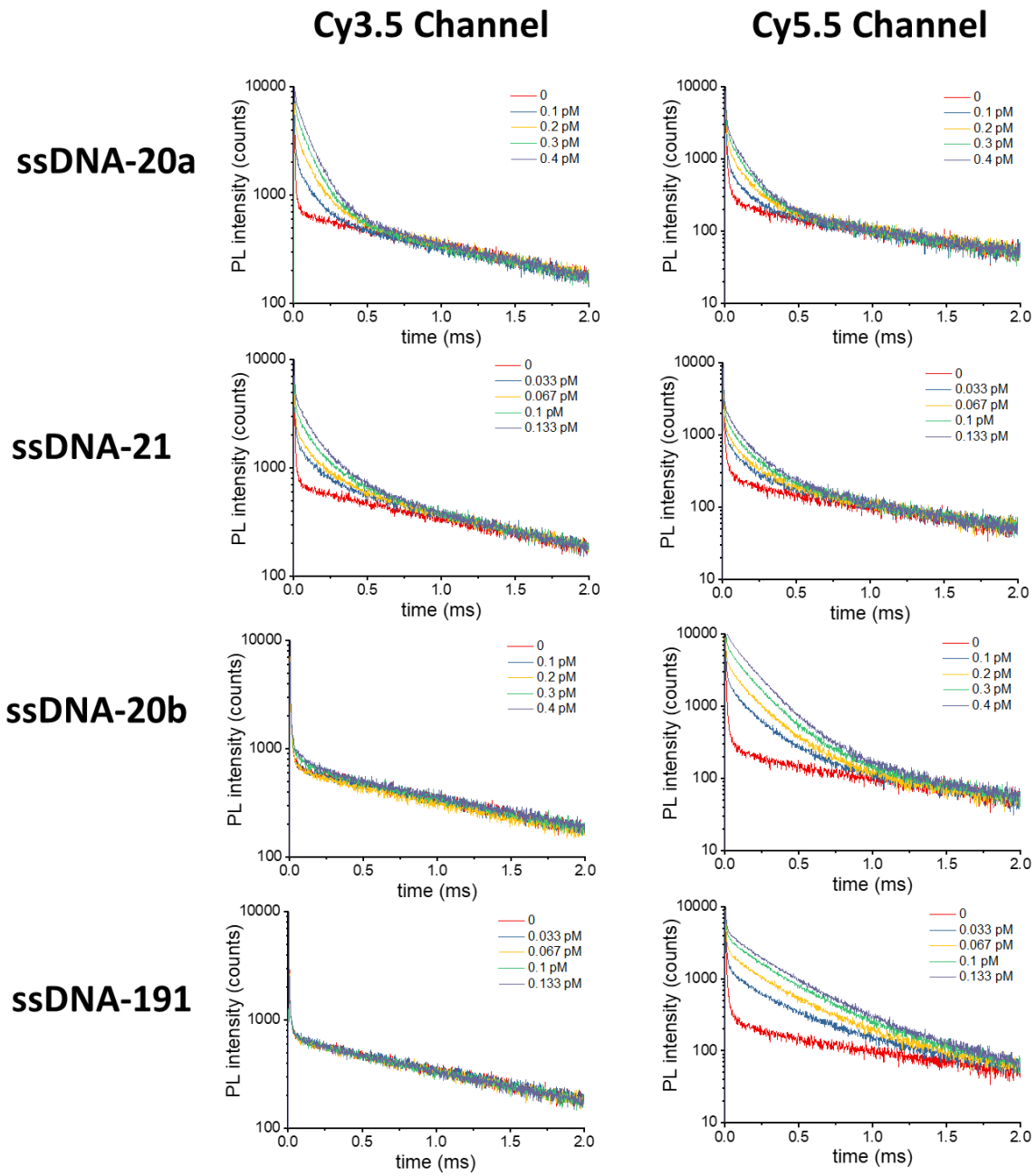

Figure 4.7. PL decay curves of the dye detection channels for calibration of spectrotemporal TG-FRET multiplexing. The assays contained all four probe-systems presented in Table.

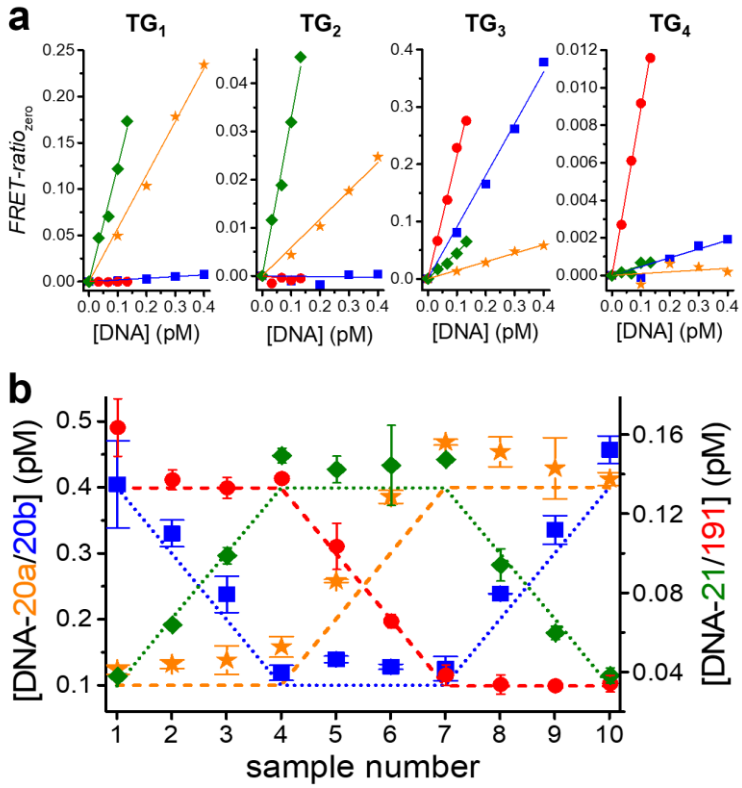

Figure 4.8. (a) Contributions of the different RCA-FRET signals (*FRET-ratio*$_{zero}$) to the different time-gated detection windows. The calibration curves (lines) were used to calculate the concentrations for the 4-fold TG-FRET multiplexed assays (see Supporting Information for mathematical treatment). (b) Recovery of varying concentrations of DNA-20a, 20b, 21, and 191 from 10 different samples using spectrotemporal TG-FRET multiplexing. Dotted lines represent known concentrations; data points represent RCA-FRET measurements.

Mathematical treatment of multiplexed signal deconvolution.

TG PL intensities (I^{TG}) of the Cy3.5/Cy5.5 acceptors and the Tb donor were determined in their specific time windows (from the corresponding PL decay curves). These TG PL intensities were then used to calculate a background-subtracted FRET-ratio (*FRET-ratio*$_{zero}$) for each target concentration $c = x$:

$$FRET\text{-}ratio_{\text{zero}} = \frac{I_{dye}^{TG}(c=x)}{I_{Tb}^{TG}(c=x)} - \frac{I_{dye}^{TG}(c=0)}{I_{Tb}^{TG}(c=0)} \tag{4.3}$$

The concentration-dependent *FRET-ratio*$_{zero}$ values were used to determine the calibration curves for each DNA target in each detection window (**Figure 4.6** for temporal TG-FRET 2-plex assays and **Figure 4.8a** for spectrotemporal TG-FRET 4-plex assays).

- ***2-plex (DNA-20a and DNA-21) temporal TG-FRET using a single Tb/Cy5.5 FRET pair:***

The slopes of the four linearly fitted calibration curves ($z_{20a}^{TG_A}$, $z_{21}^{TG_A}$, $z_{20a}^{TG_B}$, $z_{21}^{TG_B}$) from **Figure 4.6** (bottom left) were used to determine the concentrations in the duplexed assay that led to the

concentration recovery in **Figure 4.6** (bottom right) by solving the following equation for the concentrations *c*(DNA-20a) and *c*(DNA-21). *FRET-ratio*$^{A}_{zero}$ and *FRET-ratio*$^{B}_{zero}$ were the *FRET-ratio*$_{zero}$ values from the two TG detection windows (TG_A and TG_B) in the 2-plex assay.

$$\begin{bmatrix} \textit{FRET-ratio}^{A}_{zero} \\ \textit{FRET-ratio}^{B}_{zero} \end{bmatrix} = \begin{bmatrix} c(\text{DNA-20a}) \\ c(\text{DNA-21}) \end{bmatrix} \times \begin{bmatrix} z_{20a}^{TG_A} & z_{21}^{TG_A} \\ z_{20a}^{TG_B} & z_{21}^{TG_B} \end{bmatrix} \quad (4.4)$$

Figure 4.6 (bottom right) shows the selective, sensitive, and accurate recovery of DNA-20a and DNA-21 at varying sub-picomolar concentrations from thirteen different samples.

- ***4-plex (DNA-20a, DNA-20b, DNA-21, DNA-191) spectrotemporal TG-FRET using a Tb/Cy3.5 and a Tb/Cy5.5 FRET pair***

Due to negligible spectral crosstalk of Cy5.5 into the Cy3.5 channel (**Figure 4.2**), the two TG channels for the Tb/Cy3.5 FRET pair (TG_1 and TG_2) contained PL signals only for DNA-20 and DNA-21 (**Figure 4.7**). Therefore, a similar method to the one from duplexing (*vide supra*) could be used to determine the concentrations *c*(DNA-20a) and *c*(DNA-21). In this case, the slopes ($z_{20a}^{TG_1}$, $z_{21}^{TG_1}$, $z_{20a}^{TG_2}$, $z_{21}^{TG_2}$) of the four linearly fitted calibration curves for DNA-20a and DNA-21 from **Figure 4.8a** were used to determine the concentrations:

$$\begin{bmatrix} \textit{FRET-ratio}^{1}_{zero} \\ \textit{FRET-ratio}^{2}_{zero} \end{bmatrix} = \begin{bmatrix} c(\text{DNA-20a}) \\ c(\text{DNA-21}) \end{bmatrix} \times \begin{bmatrix} z_{20a}^{TG_1} & z_{21}^{TG_1} \\ z_{20a}^{TG_2} & z_{21}^{TG_2} \end{bmatrix} \quad (4.5)$$

Due to significant spectral crosstalk of Cy3.5 into the Cy5.5 channel (**Figure 4.2**), the two TG channels for the Tb/Cy5.5 FRET pair (TG_3 and TG_4) contained PL signals for all targets (DNA-20, DNA-21, DNA-20b, and DNA-191 – **Figure 4.8a**). This means that the slopes ($z_{20a}^{TG_3}$, $z_{21}^{TG_3}$, $z_{20b}^{TG_3}$, $z_{191}^{TG_3}$, $z_{20a}^{TG_4}$, $z_{21}^{TG_4}$, $z_{20b}^{TG_4}$, $z_{191}^{TG_4}$) of all eight linearly fitted calibration curves for DNA-20a, DNA-21, DNA-20b, and DNA-191 from **Figure 4.8a** needed to be taken into account to determine the concentrations of DNA-20b and DNA-191. Because the concentrations *c*(DNA-20a) and *c*(DNA-21) were determined by the Tb/Cy3.5 FRET-pair (*vide supra*), they could be used in combination with $z_{20a}^{TG_3}$, $z_{21}^{TG_3}$, $z_{20a}^{TG_4}$, and $z_{21}^{TG_4}$ (note that $z_{20a}^{TG_4} = 0$ because the contribution of DNA-20a in TG_4 is negligible – cf. **Figure 4.8a**) to subtract the contribution of these two targets in TG_3 and TG_4:

$$\Delta\textit{FRET-ratio}^{3}_{zero} = \textit{FRET-ratio}^{3}_{zero} - z_{20a}^{TG3}c(\text{DNA-20a}) - z_{21}^{TG3}c(\text{DNA-21}) \quad (4.6)$$

$$\Delta\textit{FRET-ratio}^{4}_{zero} = \textit{FRET-ratio}^{4}_{zero} - z_{21}^{TG4}c(\text{DNA-21}) \quad (4.7)$$

These corrected *FRET-ratio*$_{zero}$ values can then be used to determine the missing concentrations *c*(DNA-20b) and *c*(DNA-191) in combination with the slopes $z_{20b}^{TG_3}$, $z_{191}^{TG_3}$, $z_{20b}^{TG_4}$, and $z_{191}^{TG_4}$:

$$\begin{bmatrix} \Delta FRET\text{-}ratio^{3}_{\text{zero}} \\ \Delta FRET\text{-}ratio^{4}_{\text{zero}} \end{bmatrix} = \begin{bmatrix} c(\text{DNA-20b}) \\ c(\text{DNA-191}) \end{bmatrix} \times \begin{bmatrix} Z_{20b}^{TG_3} & Z_{191}^{TG_3} \\ Z_{20b}^{TG_4} & Z_{191}^{TG_4} \end{bmatrix} \quad (4.8)$$

Equation 4.5 and **Equation 4.6** were used for the recovery of the concentrations of the four DNA targets in the 10 different samples in **Figure 4.8b**.

4.4 Conclusion

In conclusion, RCA-FRET is the first method that can combine spectral and temporal multiplexing into higher-order multiplexed and highly sensitive detection of nucleic acids. It can be performed by straightforward procedures on commercially available time-resolved fluorescence plate readers and is adaptable to other RCA approaches and probably to any other DNA-amplification strategy that uses hybridization of fluorescent probes. RCA-FRET provided LODs down to 40 zeptomoles (300 aM) of DNA, which presents an improvement of more than four orders of magnitude compared to non-amplified TG-FRET detection of the same targets. Spectral-temporally multiplexed detection (from the same sample) of four different DNA targets in the 40 to 500 fM concentration range was accomplished by using only two different FRET-pairs and one excitation wavelength. These target concentrations were three orders of magnitude lower compared to spectral multiplexing of three DNA targets with three different FRET pairs.[7] This first demonstration of spectrotemporal multiplexing quantified only four DNAs by combining two spectral and two temporal components, but the use of TG-FRET with five different acceptors and three different time-gated windows would allow for 15-fold multiplexing from a single liquid sample or 125-fold multiplexing for imaging (**Figure 4.9**). Although such extensions are beyond the current scope, our future research will investigate the experimental limits of spectrotemporal multiplexing and the adaption of RCA-FRET to *in-situ* imaging in cells. The versatility, specificity, and sensitivity of isothermal RCA-FRET for higher-order multiplexed quantification of nucleic acids at extremely low concentrations are ideally suited to advance many fundamental and applied biological studies. Because no other technology can combine such technological versatility with accuracy and simplicity of application, we believe that RCA-FRET will be of high value both in research and diagnostics, and provide new insights about the role of DNA or RNA in biological functions and diseases.

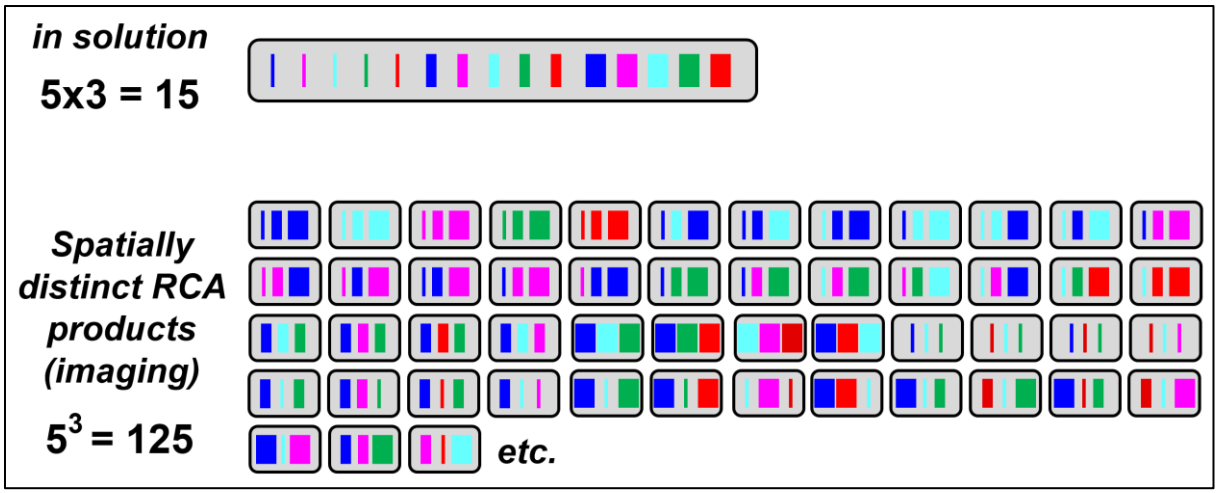

Figure 4.9. High-order spectrotemporal multiplexing capabilities using five different colors and three different time gates. Top: in solution. Bottom: With spatially distinct RCA products, *e.g.*, for imaging in cells.

Contributions

For this work, I performed the experiments, analyzed the data, and wrote part of the manuscript.

5. Temporal multiplexing Tb-QD FRET for QD-DNA conformation analysis

5.1. Introduction

The development and application of DNA-nanoparticle conjugates for advanced chemical and biological sensing is a continuously growing field of research[110],[164]–[166]. Understanding the conformation and function of nucleic acids attached to nanosurfaces under physiological conditions is of paramount importance for the design of useful and versatile analytical tools with specific and sensitive target recognition. QDs are among the most often applied nanoparticles for DNA-nanobiotechnology because their chemical and photophysical stability and outstanding fluorescence properties can be used for both investigating the DNA-nanosurface interaction and developing robust and sensitive biosensors[112], [168]–[170]. In particular, the combination with FRET opens the possibility for scrutinizing distance-dependence and orientation of DNA-nanoparticle systems and for developing and optimizing DNA-hybridization biosensors with exceptional analytical properties[171], [172].

The most interesting aspect of DNA-nanotechnology is its simplicity of constructing single- or double-stranded structures out of only four types of bases, which allows for placing energy transfer donors and acceptors at defined distances with single nucleotide (nt) sensitivity. Such flexibility in adapting donor-acceptor distances is not only useful for optimizing the energy transfer for each specific donor-acceptor pair with the aim of highest possible sensitivity. It can also be exploited to tune the photoluminescence (PL) decays for temporal optical multiplexing[173]–[175], which presents a powerful extension to the commonly used color multiplexing. Although DNA distances can be extended nt per nt, there remain important limitations both for very short and very long FRET distances. Conjugating donor and acceptor to the respective 3’ and 5’ ends of complementary ssDNA strands usually leads to very close distances (0 nt) upon hybridization and a concomitant FRET efficiency close to 100 %, which cannot be used for quantitatively analyzing donor-acceptor distances. Longer distances are mainly affected by the FRET distance limit (close to 0 % FRET efficiency), which is approximately 10 nm for efficient FRET pairs. Molecular FRET rulers were shown to be functional between ca. 5 and 9 nm with dye-dye and QD-dye pairs (polyproline distance

adjustment)[3] and between ca. 4 and 10 nm with Tb-dye pairs (dsDNA distance adjustment)[173]. A detailed analysis of many distances and the resulting conformations over a long DNA strand conjugated to a QD under physiological conditions (in aqueous solution at low concentrations) would significantly improve the understanding of how DNA orients and behaves on nanoparticle surfaces, which, in turn, would provide important information for designing DNA-nanoparticle-based biosensors.

In the study, we analyzed the conformation of a 31 nt long DNA, attached via a 5' modified peptide-His_6 sequence (peptide-DNA) to a QD, when different Tb-conjugated complementary DNA probes hybridized at distances between 0 and 26 nt from the 5' end of QD-conjugated DNA by Tb-QD temporal multiplexed FRET and biomolecular modeling (**Figure 5.1**). Our results show that Tb-to-QD distances of up to 14 nm (center-to-center) can be precisely quantified using FRET theory with a dynamically averaged orientation and fitting the FRET-sensitized QD PL decay curves. In ssDNA conformation, the distance increase was linear with ~0.15 nm/nt and the orientation of the DNA was between vertical (or perpendicular) and parallel (or tangential) attachment to the QD surface. In dsDNA conformation, the distance increase was also linear but with ~0.31 nm/nt and the orientation of the DNA was in almost perfect agreement with vertical attachment to the QD surface. All 11 conformations (0, 2, 4, 6, 10, and 14 nt for "3'-FRET" on ssDNA and 10, 14, 18, 22, and 26 nt for "5'FRET" on dsDNA) showed distinct PL decay curves and DNA-concentration-dependent time-gated FRET ratios that demonstrated the feasibility of quantitative DNA biosensing at many different Tb-QD distances for temporal multiplexing. Our results show that, despite the relatively large nanoparticle dimensions, QD-DNA conjugates can be used as precise nanometric FRET rulers over long distances and that all of the applied distances between *ca.* 7 and 14 nm can be used for quantitative DNA analysis in a low nM concentration range.

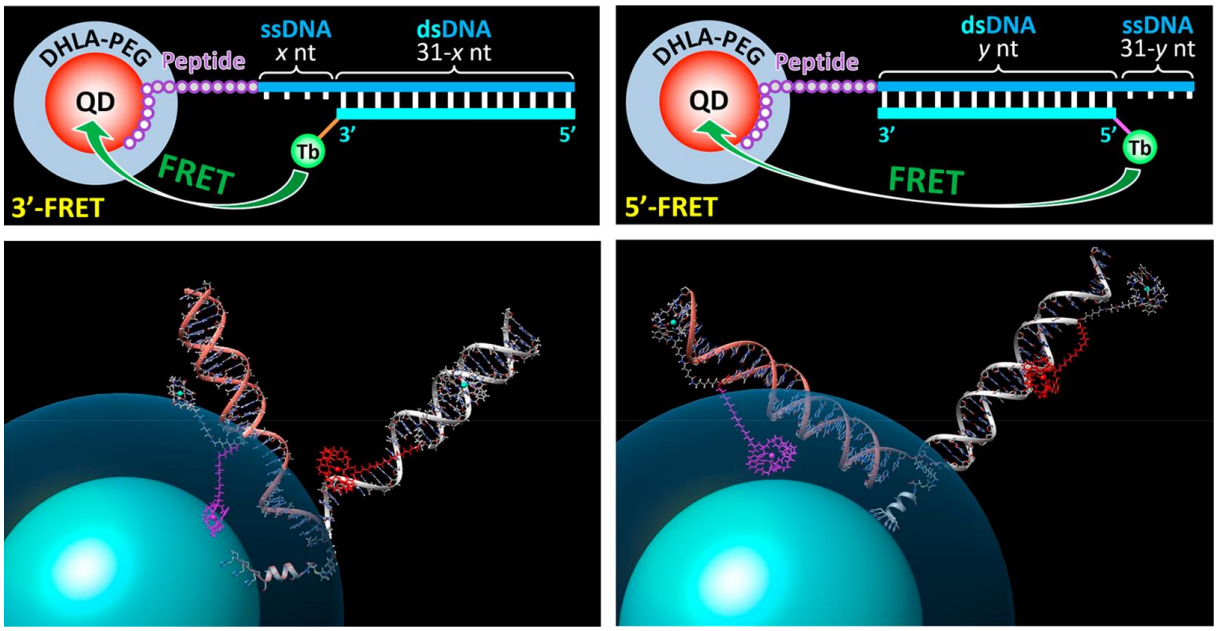

Figure 5.1. Top: All QD-DNA systems consisted of the same 31 nt long ssDNA (dark blue) that was appended (via a crosslinker at the 5' end) to a 10 amino acid peptide sequence and a His_6 for self-assembly to the QD625 surface. Different DNA probes (cyan) conjugated with Tb on their 3' or 5' ends were used to investigate the conformation of 0 to 14 nt long ssDNA appended to 31 to 17 nt long dsDNA (3'FRET, left) and 10 to 26 nt long dsDNA appended to 21 to 5 nt long ssDNA (5'-FRET, right) by Tb-to-QD FRET. Schematic presentation not to scale. **Bottom:** Biomolecular modeling was used to calculate Tb-to-QD distance ranges in parallel (orange) and vertical (gray) DNA-surface attachment configurations. Due to the short peptide sequence and crosslinker after the His_6, the DNA is situated outside the DHLA-PEG coating (dark blue) on the QD (cyan). Flexible molecular linkers between Tb and DNA led to an additional distance variation as visualized by two extreme Tb positions for each DNA. The left image shows a 14 nt 3'-FRET configuration. The right image shows a 22 nt 5'-FRET configuration.

5.2 Materials and methods

5.2.1 Materials

Lumi4-Tb-NHS was provided by Lumiphore Inc. (Berkeley, CA, USA). 625 nm emitting proprietary CdSe/ZnS QDs were provided by Invitrogen by Life Technologies (Carlsbad, CA) and functionalized with dihydrolipoic acid-appended poly(ethylene glycol) (PEG, MW~750) ligands in house. Peptide-oligonucleotides was synthesized by Biosynthesis (Lewisville, Texas, USA). All other modified oligonucleotides were purified with HPLC from Eurogentec (Liège, Belgium). All sequences and modifications of nucleic acids used in this study are summarized in **Table 5.1**. Tris(hydroxymethyl)-aminomethane, bovine serum albumin, and HEPES were purchased from Sigma-Aldrich (St. Louis, MO, USA). NaCl was purchased from Duchefa

(Netherlands). All chemicals were used as received. Water was purified by MAXIMA (USF Elga, UK). Zeba Spin Desalting Columns (7 kDa MWCO) were purchased from Thermo Fisher Scientific (Nîmes, France). Tb-DNA conjugation was performed as described above.

Table 5.1. DNA oligonucleotides used in the study

	Sequence 5'-3'	Modification	Tb/DNA ratio
Tb-DNA (for 0 base)	CTACCTGCACTATGAGCACTTTGTCGAGCTA	3′- C_6 amino	0.79
Tb-DNA (for 2 base ssDNA)	CTACCTGCACTATGAGCACTTTGTCGAGC	3′- C_6 amino	0.88
Tb-DNA (for 4 base ssDNA)	CTACCTGCACTATGAGCACTTTGTCGA	3′- C_6 amino	0.75
Tb-DNA (for 6 base ssDNA)	CTACCTGCACTATGAGCACTTTGTC	3′- C_6 amino	0.77
Tb-DNA (for 10 base ssDNA)	CTACCTGCACTATGAGCACTT	3′- C_6 amino	0.97
Tb-DNA (for 14 base ssDNA)	CTACCTGCACTATGAGC	3′- C_6 amino	0.82
Tb-DNA (for 10 bps dsDNA)	TGTCGAGCTA	5′- C_3 amino	0.85
Tb-DNA (for 14 bps dsDNA)	ACTTTGTCGAGCTA	5′- C_3 amino	0.81
Tb-DNA (for 18 bps dsDNA)	GAGCACTTTGTCGAGCTA	5′- C_3 amino	0.71
Tb-DNA (for 22 bps dsDNA)	CTATGAGCACTTTGTCGAGCTA	5′- C_3 amino	0.84
Tb-DNA (for 26 bps dsDNA)	TGCACTATGAGCACTTTGTCGAGCTA	5′- C_3 amino	0.90
Peptide-DNA	TAGCTCGACAAAGTGCTCATAGTGCAGGTAG	5′- H6SLGAAAGSGC-SMCC-amino	/

5.2.2 Spectroscopic characterization

Absorption spectra (Lambda 35 UV/vis System, PerkinElmer) and emission spectra (for Tb: FluoTime 300, PicoQuant; for QD625: Xenius, SAFAS) were recorded in 100 mM HEPES buffer (pH 7.4) for Tb and in 100 mM Na-tetraborate + 0.1 M NaCl buffer (pH 8.5) for QD625.

5.2.3 Tb-QD FRET assays

All FRET assays were prepared in DNA hybridization buffer and contained 50 µL of Tb-DNA and 50 µL of 625 nm DHLA capped QD at constant concentrations to which 50 µL of peptide-oligonucleotides at different concentrations were added. The single sensor assays contained 20 nM of Tb, 0.5 nM of QD and increasing concentrations of peptide-oligonucleotides (from 0 nM to 10 nM), and all samples were prepared once. After sample preparation, they were incubated in black 96-well microtiter plates for 30 min at room temperature (22 °C) with an optimal working volume of 150 µL. PL decay curves were acquired on a fluorescence plate reader (Edinburgh Instruments) using 4000 detection bins of 2 µs integration time and nitrogen laser (MNL 100, LTB Lasertechnik Berlin) excitation (337.1 nm, 20 Hz). Optical transmission filter (Semrock) bandpass wavelengths were 494 ± 20 nm for the Tb detection channel and 640 ± 14 nm for the QD625 detection channel. FRET ratio was used as the DNA hybridization assay detection signal, the FRET ratios are calculated by dividing the intensity of QD625 by the intensity of Tb in the time-gated window (0.1 to 2 ms). Calibration curves show the increasing time-gated PL FRET ratios with increasing peptide-DNA.

5.3. Results and discussion

5.3.1 Photophysical properties of Tb and QD and R_0 calculation

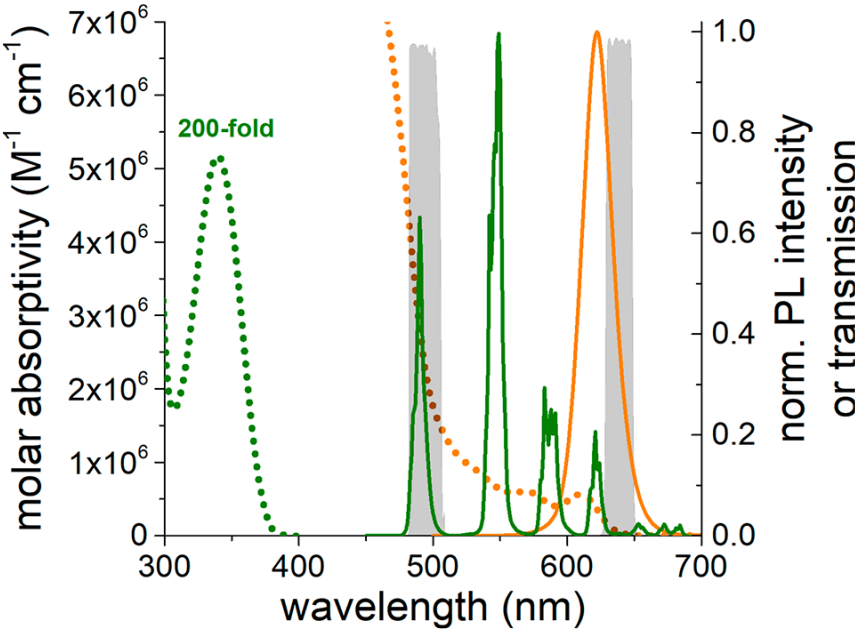

Figure 5.2. Absorption (dotted) and PL emission (solid) spectra of Tb (green) and QD625 (orange) and filter transmission spectra (gray) used for Tb donor and QD acceptor time-resolved PL detection.

A Förster distance (the donor-acceptor distance for which FRET is 50 % efficient) of R_0 = 10.3 nm was calculated using the following equation:

$$R_0 = 0.02108(\kappa^2 \Phi_D n^{-4} J)^{1/6} \quad \text{nm} \qquad (5.1)$$

The orientation factor κ^2 was taken as 2/3 because of the random orientation of donor and acceptor during the FRET time (dynamic averaging), which is well justified by the long PL lifetime of the Tb donors and the unpolarized emission (fast isotropic rotation). The refractive index was n = 1.35 (aqueous solution). The Tb-centered quantum yield was Φ_D = 0.81 ± 0.05. The overlap integral J was calculated by the following equation:

$$J = \int_{450\ nm}^{650\ nm} I_D(\lambda)\varepsilon_A(\lambda)\lambda^4 d\lambda \qquad (5.2)$$

where $I_D(\lambda)$ is the emission intensity from the area-normalized (to unity) emission spectrum of Tb donor and $\varepsilon_A(\lambda)$ is the molar absorptivity of the acceptor. The spectra are shown in **Figure 5.2**.

5.3.2 FRET DNA-Conjugates

The FRET pair consisted of a Lumi4-Tb donor (Tb) and a DHLA-PEG (dihydrolipoic acid-appended poly(ethylene glycol)-coated Qdot625 acceptor (QD625). As shown in **Figure 5.2**, pulsed UV light (337.1 nm) efficiently excites both Tb and QD625, leading to four main Tb PL bands between 450 and 650 nm and one QD PL band around 625 nm. Owing to the large difference of PL lifetimes (ms *vs.* ns), the initially excited QDs decay quickly to their ground states and become available as FRET acceptors for the long-lifetime Tb donors, which leads to FRET-quenched Tb PL and FRET-sensitized QD-PL with the same PL decay times ($\tau_{DA} = \tau_{AD}$). The well-overlapping Tb PL and QD absorption (**Figure 5.2**) resulted in a Förster distance (donor-acceptor distance for which FRET is 50 % efficient) of R_0 = 10.3 nm (see **Equations 5.1** and 5.**2** and Materials and Methods section for details). For minimal spectral crosstalk between the Tb and QD, PL decays were measured at 494±20 nm for Tb and 640±14 nm for QD625 (see **Figure 5.2** for filter transmission spectra).

The main 31 nt long DNA strand (see **Table 5.1** for sequences of all DNA used in our study) was attached via metal-affinity mediated self-assembly to the Zn-rich surface of QD625[176], [177]. The His_6 was appended to 10 additional amino acids (SLGAAAGSGC) and a crosslinker that extended the DNA slightly beyond the DHLA-PEG coating on the QD625 surface (cf. **Figure 5.1** bottom), such that the conformational freedom of the DNA was not restrained. The Tb donor was brought into FRET proximity of the QD by hybridization of different Tb-DNA probes to the main QD-DNA strand. The distance between the first nt on the 5' end of peptide-DNA and the Tb (on the 3' or 5' end depending on the configuration) was adjusted in 11 different configurations between 0 and 26 nt, which resulted in Tb distances of 0 to 14 ssDNA bases and 10 to 26 dsDNA base pairs after the peptide extension from the QD (cf. **Figure 5.1**).

5.3.3 PL decay curves and fit results of Tb and QD for Tb-QD-DNA configurations with 0, 2, 4, 6, 10 and 14 bases ssDNAs, and 10, 14, 18, 22, 26 bases dsDNAs separation.

All PL decay curves were fit using multi-exponential intensity decay functions with a starting time point for the fit of t_0, which corresponds to a short delay between the start of the actual PL decay and the start of the fit (due to very strong background fluorescence in the short time range, the fits usually start after a few tens of µs as indicated above each fit result table). The PL intensity decay is defined by the following equation:

$$I = \sum_i A_{i-Fit} \exp\left(-\frac{t-t_0}{\tau_i}\right) = \sum_i A_i \exp\left(-\frac{t}{\tau_i}\right) \quad (5.3)$$

Fast software from Edinburgh instruments was used for fitting all decay curves. As the actual decay starts before t_0, the amplitudes ($A_{i\text{-Fit}}$), which are used to calculate average PL lifetimes, need to be corrected using the following equation:

$$A_{i-Fit} \exp\left(-\frac{t-t_0}{\tau_i}\right) = A_i \exp\left(-\frac{t}{\tau_i}\right) \implies A_i = A_{i-Fit} \exp\left(-\frac{t_0}{t}\right) \quad (5.4)$$

Because all decay curves (in particular those from the Tb donor detection channel) contain a certain amount of unquenched Tb decay, this "pure Tb" decay time (τ_D) was used as a fixed decay time in the multiexponential fit functions. τ_D was determined for each set of experiments (in the Tb-donor channel and the QD-acceptor channel) by fitting the decay for a sample in which only Tb-DNA was present. τ_D (in ms) was also used to determine the Tb-centered PL quantum yield ($\Phi_{Tb} = \tau_D$ /3.45 ms; 3.45 ms is the Tb lifetime for Φ_{Tb}= 1), which is the quantum yield that needs to be used for calculating the Förster distance individually for each DNA system. Tb donor decays were fit by a three-exponential function (with τ_i corresponding to τ_D, τ_{DA1}, and τ_{DA2}) from **Figure 5.3** to **5.9** and by a two-exponential function (with τ_i corresponding to τ_D and τ_{DA1}) from **Figure 5.10** to **5.13**, whereas QD acceptor decays were fit with a quadruple-exponential function (with τ_i corresponding to τ_D, τ_{AD1}, τ_{AD2}, and τ_{AD3}).

For Tb donor decays, the amplitude averaged decay time $\langle\tau_{DA}\rangle$ was used as FRET decay time to calculate the Tb-QD distance *r*.

$$\langle\tau_{DA}\rangle = \frac{\sum A_i\tau_i}{\sum A_i} \quad (5.5)$$

with τ_i corresponding to the FRET-quenched PL decay times τ_{DA1} and τ_{DA2} (the pure Tb decay with τ_D is not taken into account).

$$r = R_0 \left(\frac{\langle\tau_{DA}\rangle}{\tau_D - \langle\tau_{DA}\rangle}\right)^{1/6} \quad (5.6)$$

The FRET efficiency was calculated by:

$$E_{FRET} = \frac{{R_0}^6}{{R_0}^6 + r^6} = 1 - \frac{\langle\tau_{DA}\rangle}{\tau_D} \quad (5.7)$$

For the QD acceptor, the amplitude averaged decay time $\langle\tau_{AD}\rangle$ was used as FRET decay time to calculate the Tb-QD distance *r*. The amplitudes A_i must be corrected by the FRET rates ($k_{FRET\text{-}i}$) to take into account the FRET-efficiency dependent excitation of the acceptors:

$$k_{FRET-i} = \frac{1}{\tau_{ADi}} - \frac{1}{\tau_D} \tag{5.8}$$

and

$$\langle \tau_{AD} \rangle = \sum \left(\frac{(A_i / k_{FRET-i})}{\sum (A_i / k_{FRET-i})} \tau_i \right) \tag{5.9}$$

with τ_i corresponding to the FRET-sensitized PL decay times τ_{AD2}, and τ_{AD3} (the pure Tb decay with τ_D and the very short QD-background decay with τ_{AD1} are not taken into account).

The Tb-QD distance *r* was then calculated by:

$$r = R_0 \left(\frac{\langle \tau_{AD} \rangle}{\tau_D - \langle \tau_{AD} \rangle} \right)^{1/6} \tag{5.10}$$

The FRET efficiency was calculated by:

$$E_{FRET} = \frac{{R_0}^6}{{R_0}^6 + r^6} = 1 - \frac{\langle \tau_{AD} \rangle}{\tau_D} \tag{5.11}$$

Due to the relatively low FRET efficiencies for the configurations with long Tb-QD donor-acceptor distances (18, 22, and 26 dsDNAs separation) the QD acceptor decay fits from **Figure 5.11** to **5.13** required further adjustment of the fit parameters. Here, the amplitude of pure Tb decay (from spectral crosstalk in the acceptor channel) was fixed to the following value:

$$A_D = \frac{A_{A0} A_{DA0}}{A_{D0}} \tag{5.12}$$

where $A_{A0}$is the amplitude of the pure Tb decay curve in the QD detection channel and A_{DA0} and A_{D0} are the amplitudes of the Tb decay curves in the Tb detection channel, in the presence and in the absence of peptide-DNA, respectively.

Figures 5.3 to **5.13** show the PL decay curves (and fitted curves) in the Tb donor and QD acceptor channels for all DNA systems (0, 2, 4, 6, 10 and 14 ssDNAs, and 10, 14, 18, 22, 26 dsDNAs). The corresponding fit results (all decay times given in μs) are given directly below the Figures.

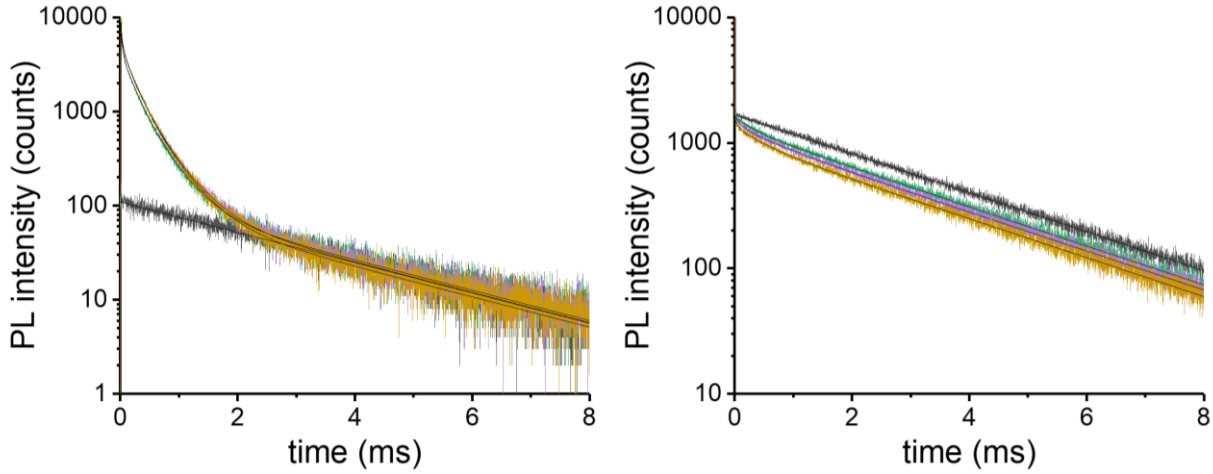

Figure 5.3. The PL decay curves of QD acceptor (left) and Tb donor (right) situated at **0 base** distances from each other. Black: pure Tb (some Tb luminescence is also visible in the acceptor detection channel due to spectral crosstalk); green: 6 nM peptide-DNA; purple: 8.0 nM peptide-DNA; yellow: 10.0 nM peptide-DNA. Black lines represent the fit results from below.

Fit results (all decay times in µs):

Donor Channel R_0 = 10.3 nm Fitted from t_0 = 0.02 ms to t = 8 ms

Sample		Tb background		FRET parameter				averaged results	
		fixed	free	free	free	free	free		
#	Peptide conc./nM	τ_D	A_D	τ_{DA1}	A_{DA1}	τ_{DA2}	A_{DA2}	$\langle\tau_{DA}\rangle$	E_{FRET}
1	Tb alone	2800	1669	D in the absence of A (mono-exponential)					
2	6.0	2800	1284	230	230	860	121	450	0.84
3	8.0	2800	1170	110	229	630	225	370	0.87
4	10.0	2800	1037	57	231	510	311	320	0.89
average 2-4		2800		130		670		380	0.86
distance r (nm)				6.2		8.5		7.6	7.6

Maximum errors: $\Delta\langle\tau_{DA}\rangle$ = 70 µs (19 %) Δr = 0.3 nm (4 %)

Acceptor channel R_0 = 10.3 nm Fitted from t_0 = 0.05 to t = 6 ms

Sample		Tb background		QD background			FRET parameter						averaged results	
		fixed	free	free	free	free	free	free	free	free	free	free		
#	Peptide conc./nM	τ_D	A_D	τ_{DA1}	A_{DA1}	k_{FRET-1}	τ_{DA2}	A_{DA2}	k_{FRET-2}	τ_{DA3}	A_{DA3}	k_{FRET-3}	$\langle\tau_{AD}\rangle$	E_{FRET}
1	Tb alone	2700	111	D in the absence of A (mono-exponential)										
2	6.0	2700	116	27	4283	0.0367	190	2506	0.0049	420	1799	0.0020	336	0.88
3	8.0	2700	110	43	1833	0.0229	190	2964	0.0049	440	2072	0.0019	350	0.87
4	10.0	2700	99	29	4240	0.0341	200	3050	0.0046	440	1974	0.0019	347	0.88
average 2-4		2700		33			193			433			344	0.88
distance r (nm)				4.9			6.7			7.8			7.4	7.4

Maximum errors: $\Delta\langle\tau_{DA}\rangle$ = 8 µs (3 %) Δr = 0.1 nm (2 %)

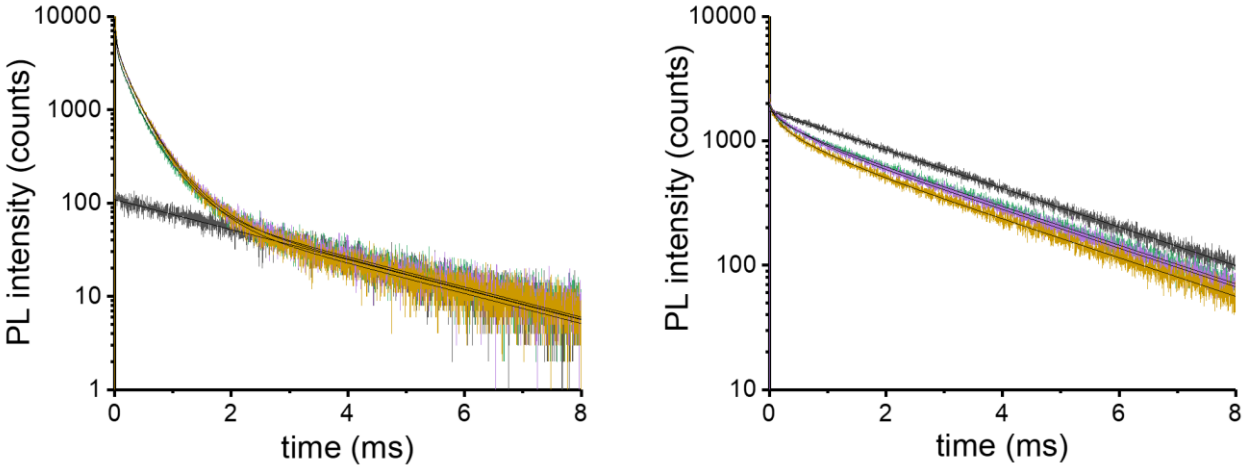

Figure 5.4. The PL decay curves of QD acceptor (left) and Tb donor (right) situated at **2 bases ssDNA** distances from each other. Black: pure Tb (some Tb luminescence is also visible in the acceptor detection channel due to spectral crosstalk); green: 6 nM peptide-DNA; purple: 8.0 nM peptide-DNA; yellow: 10.0 nM peptide-DNA. Black lines represent the fit results from below.

Fit results (all decay times in µs):

Donor Channel R_0 = 10.3 nm Fitted from t_0 = 0.02 ms to t = 8 ms

Sample		Tb background		FRET parameter				averaged results	
		fixed	free	free	free	free	free		
#	Peptide conc./nM	τ_D	A_D	τ_{DA1}	A_{DA1}	τ_{DA2}	A_{DA2}	$\langle\tau_{DA}\rangle$	E_{FRET}
1	Tb alone	2800	1960	D in the absence of A (mono-exponential)					
2	6.0	2800	1237	89	328	600	365	360	0.87
3	8.0	2800	1169	81	367	580	507	370	0.87
4	10.0	2800	979	130	478	680	458	400	0.86
average 2-4		2800		100		620		380	0.87
distance r (nm)				5.9		8.4		7.6	7.6

Maximum errors: $\Delta\langle\tau_{DA}\rangle$ = 20 µs (5 %) Δr = 0.1 nm (2 %)

Acceptor channel R_0 = 10.3 nm Fitted from t_0 = 0.05 to t = 6 ms

Sample		Tb background		QD background			FRET parameter						averaged results	
		fixed	free	free	free	free	free	free	free	free	free	free		
#	Peptide conc./nM	τ_D	A_D	τ_{DA1}	A_{DA1}	k_{FRET-1}	τ_{DA2}	A_{DA2}	k_{FRET-2}	τ_{DA3}	A_{DA3}	k_{FRET-3}	$\langle\tau_{AD}\rangle$	E_{FRET}
1	Tb alone	2700	115	D in the absence of A (mono-exponential)										
2	6.0	2700	116	36	3902	0.0270	220	3378	0.0042	480	2121	0.0017	377	0.87
3	8.0	2700	115	33	4632	0.0303	240	4676	0.0038	500	2708	0.0016	389	0.86
4	10.0	2700	103	34	4426	0.0294	240	4709	0.0038	500	2891	0.0016	393	0.86
average 2-4		2700		34			233			493			386	0.86
distance r (nm)				5.0			6.9			8.0			7.6	7.6

Maximum errors: $\Delta\langle\tau_{DA}\rangle$ = 9 µs (3 %) Δr = 0.1 nm (2 %)

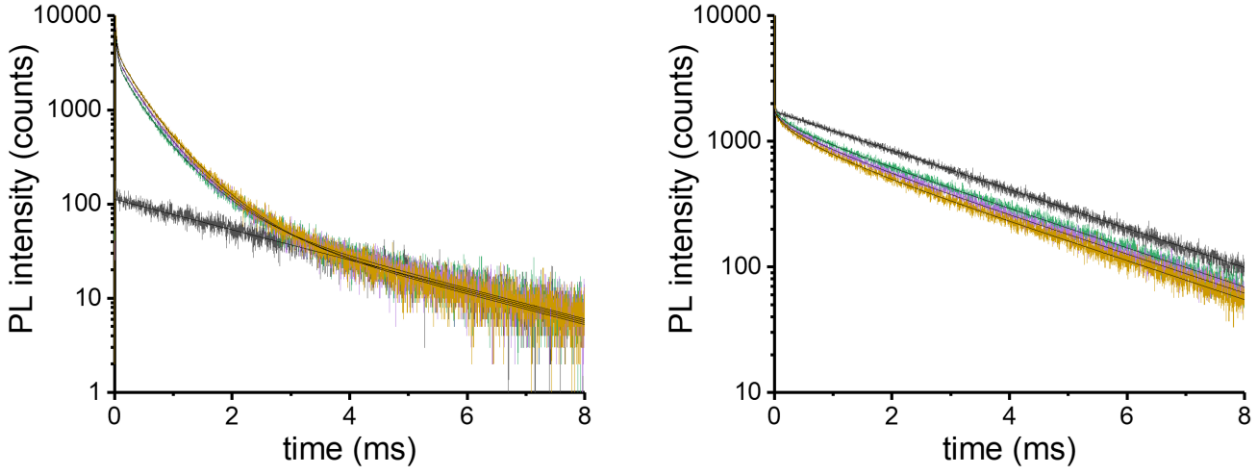

Figure 5.5. The PL decay curves of QD acceptor (left) and Tb donor (right) situated at **4 bases ssDNA** distances from each other. Black: pure Tb (some Tb luminescence is also visible in the acceptor detection channel due to spectral crosstalk); green: 6 nM peptide-DNA; purple: 8.0 nM peptide-DNA; yellow: 10.0 nM peptide-DNA. Black lines represent the fit results from below.

Fit results (all decay times in µs):

Donor Channel R_0 = 10.3 nm Fitted from t_0 = 0.02 ms to t = 8 ms

Sample		Tb background		FRET parameter				averaged results	
		fixed	free	free	free	free	free		
#	Peptide conc./nM	τ_D	A_D	τ_{DA1}	A_{DA1}	τ_{DA2}	A_{DA2}	$\langle\tau_{DA}\rangle$	E_{FRET}
1	Tb alone	2800	1673	D in the absence of A (mono-exponential)					
2	6.0	2800	1203	220	264	960	244	580	0.79
3	8.0	2800	1077	120	283	780	374	500	0.82
4	10.0	2800	955	140	318	750	442	490	0.83
average 2-4		2800		160		830		520	0.81
distance r (nm)				6.5		8.9		8.1	8.1

Maximum errors: $\Delta\langle\tau_{DA}\rangle$ = 60 µs (11 %) Δr = 0.1 nm (2 %)

Acceptor channel R_0 = 10.3 nm Fitted from t_0 = 0.05 to t = 6 ms

Sample		Tb background		QD background			FRET parameter						averaged results	
		fixed	free	free	free	free	free	free	free	free	free	free		
#	Peptide conc./nM	τ_D	A_D	τ_{DA1}	A_{DA1}	k_{FRET-1}	τ_{DA2}	A_{DA2}	k_{FRET-2}	τ_{DA3}	A_{DA3}	k_{FRET-3}	$\langle\tau_{AD}\rangle$	E_{FRET}
1	Tb alone	2700	114	D in the absence of A (mono-exponential)										
2	6.0	2700	117	30	4868	0.0326	250	1679	0.0036	580	1672	0.0014	490	0.83
3	8.0	2700	107	26	7049	0.0379	280	2080	0.0032	610	1702	0.0013	502	0.82
4	10.0	2700	102	32	4865	0.0312	280	2292	0.0032	610	2001	0.0013	507	0.82
average 2-4		2700		29			270			600			499	0.82
distance r (nm)				4.8			7.1			8.3			8.0	8.0

Maximum errors: $\Delta\langle\tau_{DA}\rangle$ = 9 µs (2 %) Δr = 0.1 nm (2 %)

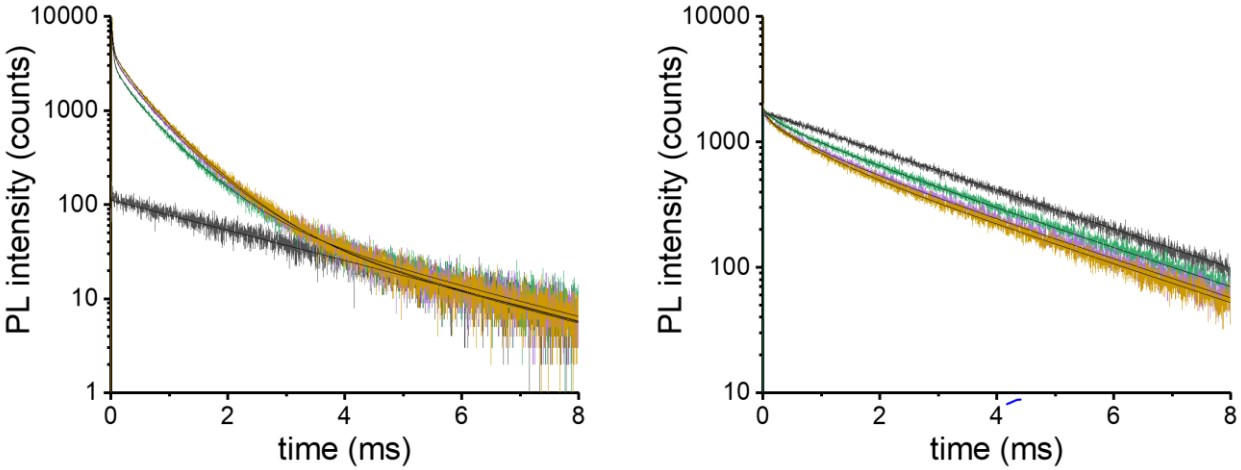

Figure 5.6. The PL decay curves of QD acceptor (left) and Tb donor (right) situated at **6 bases ssDNA** distances from each other. Black: pure Tb (some Tb luminescence is also visible in the acceptor detection channel due to spectral crosstalk); green: 6 nM peptide-DNA; purple: 8.0 nM peptide-DNA; yellow: 10.0 nM peptide-DNA. Black lines represent the fit results from below.

Fit results (all decay times in µs):

Donor Channel R_0 = 10.3 nm Fitted from t_0 = 0.02 ms to t = 8 ms

Sample		Tb background		FRET parameter				averaged results	
		fixed	free	free	free	free	free		
#	Peptide conc./nM	τ_D	A_D	τ_{DA1}	A_{DA1}	τ_{DA2}	A_{DA2}	$\langle\tau_{DA}\rangle$	E_{FRET}
1	Tb alone	2800	1824	D in the absence of A (mono-exponential)					
2	6.0	2800	1219	180	248	990	359	660	0.76
3	8.0	2800	993	210	255	930	449	670	0.76
4	10.0	2800	908	100	350	810	596	550	0.80
average 2-4		2800		160		910		630	0.78
distance r (nm)				6.5		9.1		8.4	8.4

Maximum errors: $\Delta\langle\tau_{DA}\rangle$ = 60 µs (13 %) Δr = 0.3 nm (4 %)

Acceptor channel R_0 = 10.3 nm Fitted from t_0 = 0.05 to t = 6 ms

Sample		Tb background		QD background			FRET parameter						averaged results	
		fixed	free	free	free	free	free	free	free	free	free	free		
#	Peptide conc./nM	τ_D	A_D	τ_{DA1}	A_{DA1}	k_{FRET-1}	τ_{DA2}	A_{DA2}	k_{FRET-2}	τ_{DA3}	A_{DA3}	k_{FRET-3}	$\langle\tau_{AD}\rangle$	E_{FRET}
1	Tb alone	2700	114	D in the absence of A (mono-exponential)										
2	6.0	2700	125	25	6963	0.0396	260	1246	0.0035	670	1872	0.0011	597	0.79
3	8.0	2700	109	34	3807	0.0292	310	1704	0.0029	710	2111	0.0011	619	0.78
4	10.0	2700	106	25	7008	0.0398	270	1761	0.0033	690	2545	0.0011	613	0.78
average 2-4		2700		28			280			690			609	0.78
distance r (nm)				4.8			7.1			8.5			8.3	8.3

Maximum errors: $\Delta\langle\tau_{DA}\rangle$ = 10 µs (2 %) Δr = 0.1 nm (2 %)

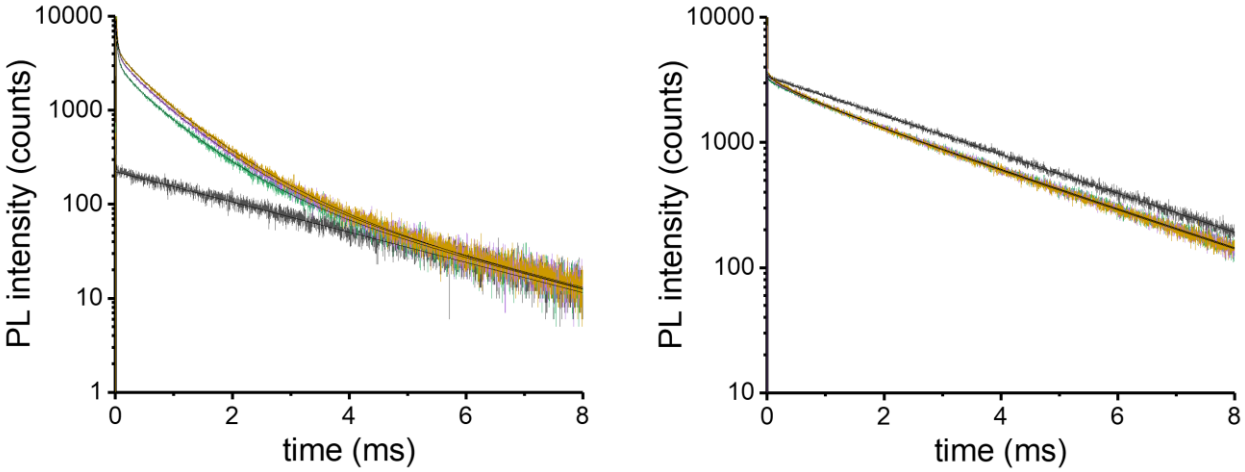

Figure 5.7. The PL decay curves of QD acceptor (left) and Tb donor (right) situated at **10 bases ssDNA** distances from each other. Black: pure Tb (some Tb luminescence is also visible in the acceptor detection channel due to spectral crosstalk); green: 6 nM peptide-DNA; purple: 8.0 nM peptide-DNA; yellow: 10.0 nM peptide-DNA. Black lines represent the fit results from below.

Fit results (all decay times in µs):

Donor Channel R_0 = 10.3 nm Fitted from t_0 = 0.02 ms to t = 8 ms

Sample		Tb background		FRET parameter				averaged results	
		fixed	free	free	free	free	free		
#	Peptide conc./nM	τ_D	A_D	τ_{DA1}	A_{DA1}	τ_{DA2}	A_{DA2}	$\langle\tau_{DA}\rangle$	E_{FRET}
1	Tb alone	2800	3366	D in the absence of A (mono-exponential)					
2	6.0	2800	2516	140	235	990	526	730	0.74
3	8.0	2800	2482	110	361	1000	676	690	0.75
4	10.0	2800	2446	99	388	940	809	670	0.76
average 2-4		2800		120		980		700	0.75
distance r (nm)				6.1		9.3		8.6	8.6

Maximum errors: $\Delta\langle\tau_{DA}\rangle$ = 30 µs (5 %) Δr = 0.1 nm (2 %)

Acceptor channel R_0 = 10.3 nm Fitted from t_0 = 0.05 to t = 6 ms

Sample		Tb background		QD background			FRET parameter						averaged results	
		fixed	free	free	free	free	free	free	free	free	free	free		
#	Peptide conc./nM	τ_D	A_D	τ_{DA1}	A_{DA1}	k_{FRET-1}	τ_{DA2}	A_{DA2}	k_{FRET-2}	τ_{DA3}	A_{DA3}	k_{FRET-3}	$\langle\tau_{AD}\rangle$	E_{FRET}
1	Tb alone	2700	226	D in the absence of A (mono-exponential)										
2	6.0	2700	240	30	4728	0.0330	240	921	0.0038	790	2163	0.0009	739	0.74
3	8.0	2700	250	30	5411	0.0330	290	1088	0.0031	800	2650	0.0009	746	0.73
4	10.0	2700	240	29	5810	0.0341	340	1443	0.0026	850	2693	0.0008	776	0.72
average 2-4		2700		30			290			813			754	0.73
distance r (nm)				4.8			7.2			8.9			8.7	8.7

Maximum errors: $\Delta\langle\tau_{DA}\rangle$ = 22 µs (3 %) Δr = 0.1 nm (2 %)

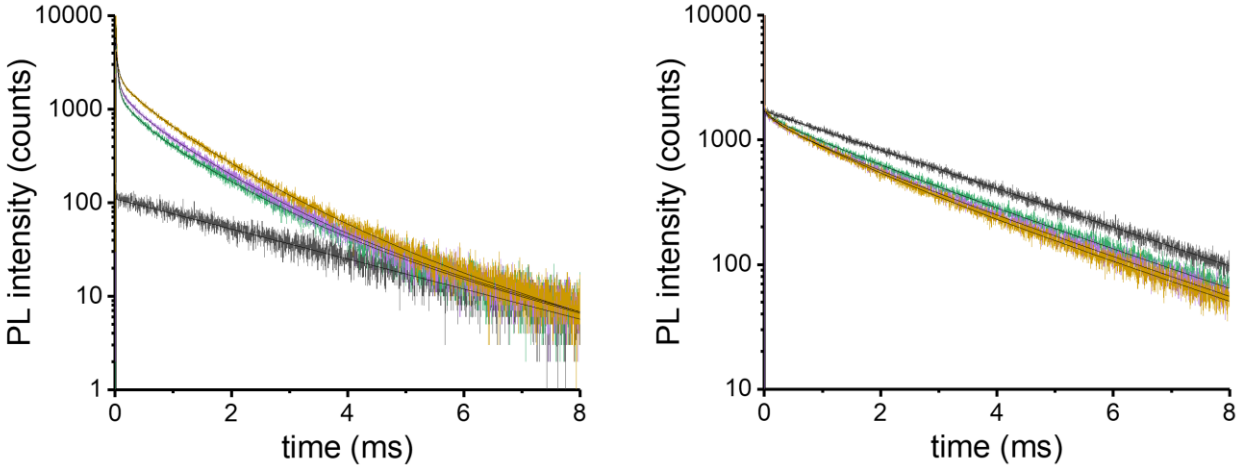

Figure 5.8. The PL decay curves of QD acceptor (left) and Tb donor (right) situated at **14 bases ssDNA** distances from each other. Black: pure Tb (some Tb luminescence is also visible in the acceptor detection channel due to spectral crosstalk); green: 6 nM peptide-DNA; purple: 8.0 nM peptide-DNA; yellow: 10.0 nM peptide-DNA. Black lines represent the fit results from below.

Fit results (all decay times in µs):

Donor Channel R_0 = 10.3 nm Fitted from t_0 = 0.02 ms to t = 8 ms

Sample		Tb background		FRET parameter				averaged results	
		fixed	free	free	free	free	free		
#	Peptide conc./nM	τ_D	A_D	τ_{DA1}	A_{DA1}	τ_{DA2}	A_{DA2}	$\langle\tau_{DA}\rangle$	E_{FRET}
1	Tb alone	2800	1730	D in the absence of A (mono-exponential)					
2	6.0	2800	1103	180	143	1300	427	1020	0.64
3	8.0	2800	949	270	210	1300	478	990	0.65
4	10.0	2800	869	180	229	1200	624	930	0.67
average 2-4		2800		210		1270		**980**	0.65
distance r (nm)				6.8		10.0		**9.3**	9.3

Maximum errors: $\Delta\langle\tau_{DA}\rangle$ = 50 µs (6 %) Δr = 0.1 nm (2 %)

Acceptor channel R_0 = 10.3 nm Fitted from t_0 = 0.05 to t = 6 ms

Sample		Tb background		QD background			FRET parameter						averaged results	
		fixed	free	free	free	free	free	free	free	free	free	free		
#	Peptide conc./nM	τ_D	A_D	τ_{DA1}	A_{DA1}	k_{FRET-1}	τ_{DA2}	A_{DA2}	k_{FRET-2}	τ_{DA3}	A_{DA3}	k_{FRET-3}	$\langle\tau_{AD}\rangle$	E_{FRET}
1	Tb alone	2700	112	D in the absence of A (mono-exponential)										
2	6.0	2700	122	31	5003	0.0323	280	592	0.0032	1000	816	0.0006	909	0.68
3	8.0	2700	125	31	4910	0.0324	250	662	0.0036	990	1052	0.0007	915	0.67
4	10.0	2700	114	44	2954	0.0226	390	821	0.0022	1100	1261	0.0006	1001	0.64
average 2-4		2700		35			307			1030			**941**	0.66
distance r (nm)				5.0			7.3			9.4			**9.2**	9.2

Maximum errors: $\Delta\langle\tau_{DA}\rangle$ = 60 µs (7 %) Δr = 0.1 nm (2 %)

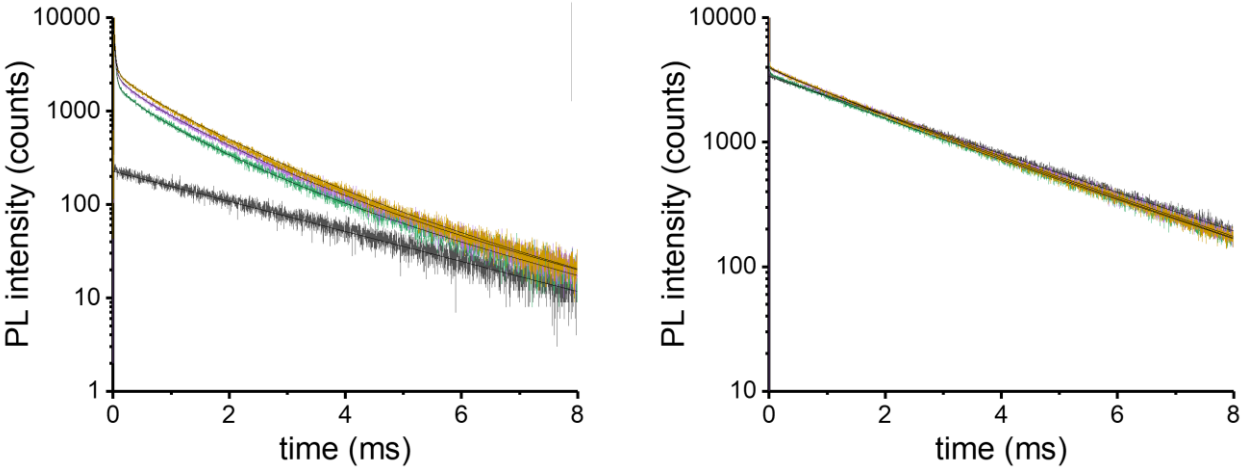

Figure 5.9. The PL decay curves of QD acceptor (left) and Tb donor (right) situated at **10 bps dsDNA** distances from each other. Black: pure Tb (some Tb luminescence is also visible in the acceptor detection channel due to spectral crosstalk); green: 6 nM peptide-DNA; purple: 8.0 nM peptide-DNA; yellow: 10.0 nM peptide-DNA. Black lines represent the fit results from below.

Fit results (all decay times in µs):

Donor Channel R_0 **= 10.3 nm** **Fitted from** t_0 **= 0.02 ms to** t **= 8 ms**

Sample		Tb background		FRET parameter				averaged results	
		fixed	free	free	free	free	free		
#	Peptide conc./nM	τ_D	A_D	τ_{DA1}	A_{DA1}	τ_{DA2}	A_{DA2}	$\langle\tau_{DA}\rangle$	E_{FRET}
1	Tb alone	2800	3373	D in the absence of A (mono-exponential)					
2	6.0	2800	2893	26	294	1300	627	890	0.68
3	8.0	2800	2978	380	162	1500	807	1310	0.53
4	10.0	2800	2919	85	145	1300	1009	1150	0.59
average 2-4		2800		160		1370		**1120**	0.60
distance r (nm)				6.5		10.2		**9.6**	9.6

Maximum errors: $\Delta\langle\tau_{DA}\rangle$ **= 190 µs (17 %)** Δr **= 0.5 nm (6 %)**

Acceptor channel R_0 **= 10.3 nm** **Fitted from** t_0 **= 0.05 to** t **= 6 ms**

Sample		Tb background		QD background			FRET parameter						averaged results	
		fixed	free	free	free	free	free	free	free	free	free	free		
#	Peptide conc./nM	τ_D	A_D	τ_{DA1}	A_{DA1}	k_{FRET-1}	τ_{DA2}	A_{DA2}	k_{FRET-2}	τ_{DA3}	A_{DA3}	k_{FRET-3}	$\langle\tau_{AD}\rangle$	E_{FRET}
1	Tb alone	2700	230	D in the absence of A (mono-exponential)										
2	6.0	2700	320	26	7911	0.0384	280	551	0.0032	1100	1150	0.0006	1038	0.63
3	8.0	2700	366	24	9950	0.0420	230	631	0.0040	1100	1570	0.0006	1054	0.62
4	10.0	2700	352	31	5761	0.0316	350	611	0.0025	1200	1746	0.0005	1147	0.59
average 2-4		2700		27			287			1133			**1080**	0.61
distance r (nm)				4.8			7.2			9.7			**9.5**	9.5

Maximum errors: $\Delta\langle\tau_{DA}\rangle$ **= 67 µs (7 %)** Δr **= 0.2 nm (3 %)**

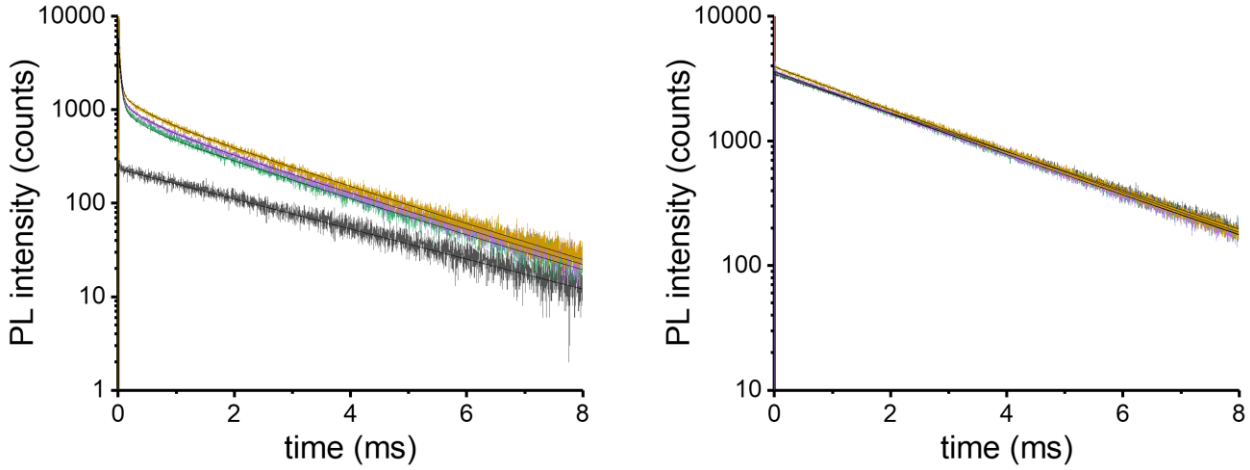

Figure 5.10. The PL decay curves of QD acceptor (left) and Tb donor (right) situated at **14 bps dsDNA** distances from each other. Black: pure Tb (some Tb luminescence is also visible in the acceptor detection channel due to spectral crosstalk); green: 6 nM peptide-DNA; purple: 8.0 nM peptide-DNA; yellow: 10.0 nM peptide-DNA. Black lines represent the fit results from below.

Fit results (all decay times in µs):

Donor Channel R_0 = 10.3 nm Fitted from t_0 = 0.02 ms to t = 8 ms

Sample		Tb background		FRET parameter		averaged results	
		fixed	free	free	free		
#	Peptide conc./nM	τ_D	A_D	τ_{DA1}	A_{DA1}	$\langle\tau_{DA}\rangle$	E_{FRET}
1	Tb alone	2800	3391	D in the absence of A (mono-exponential)			
2	6.0	2800	2982	1800	570	1800	0.36
3	8.0	2800	2875	1900	738	1900	0.32
4	10.0	2800	3032	1800	895	1800	0.36
average 2-4		2800		1830		1830	0.35
distance r (nm)				11.4		11.4	11.5

Maximum errors: $\Delta\langle\tau_{DA}\rangle$ = 70 µs (4 %) Δr = 0.3 nm (3 %)

Acceptor channel R_0 = 10.3 nm Fitted from t_0 = 0.05 to t = 6 ms

Sample		Tb background		QD background			FRET parameter						averaged results	
		fixed	free	free	free	free	free	free	free	free	free	free		
#	Peptide conc./nM	τ_D	A_D	τ_{DA1}	A_{DA1}	k_{FRET-1}	τ_{DA2}	A_{DA2}	k_{FRET-2}	τ_{DA3}	A_{DA3}	k_{FRET-3}	$\langle\tau_{AD}\rangle$	E_{FRET}
1	Tb alone	2700	237	D in the absence of A (mono-exponential)										
2	6.0	2700	236	37	3832	0.0267	400	377	0.0021	1900	493	0.0002	1814	0.35
3	8.0	2700	228	36	4227	0.0274	460	411	0.0018	2000	580	0.0001	1919	0.31
4	10.0	2700	240	33	4860	0.0299	410	490	0.0021	1900	764	0.0002	1826	0.35
average 2-4		2700		35			423			1933			1853	0.34
distance r (nm)				5.0			7.7			11.8			11.5	11.5

Maximum errors: $\Delta\langle\tau_{DA}\rangle$ = 66 µs (4 %) Δr = 0.2 nm (2 %)

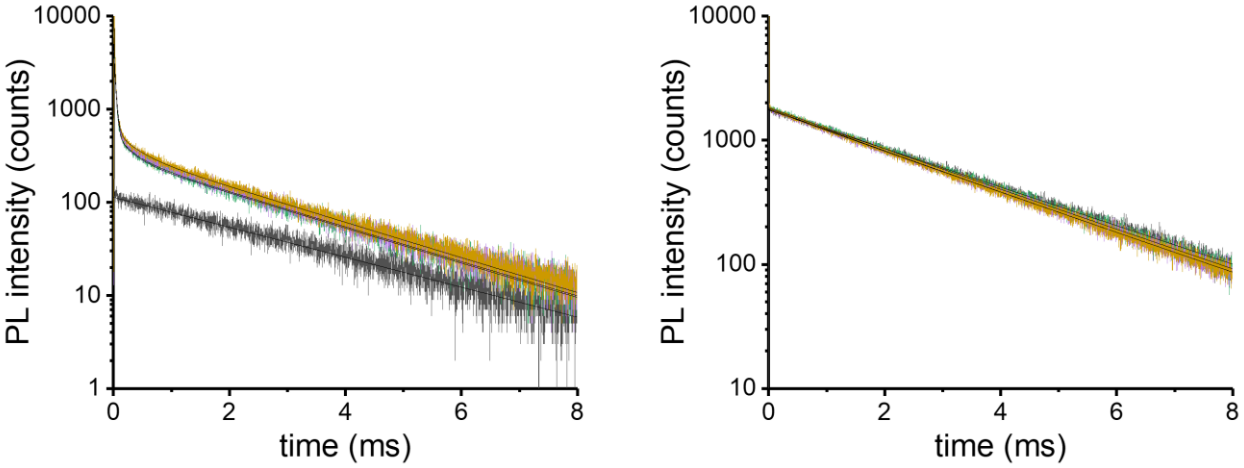

Figure 5.11. The PL decay curves of QD acceptor (left) and Tb donor (right) situated at **18 bps dsDNA** distances from each other. Black: pure Tb (some Tb luminescence is also visible in the acceptor detection channel due to spectral crosstalk); green: 6 nM peptide-DNA; purple: 8.0 nM peptide-DNA; yellow: 10.0 nM peptide-DNA. Black lines represent the fit results from below.

Fit results (all decay times in µs):

Donor Channel R_0 **= 10.3 nm** **Fitted from** t_0 **= 0.02 ms to** t **= 8 ms**

Sample		Tb background		FRET parameter		averaged results	
		fixed	free	free	free		
#	Peptide conc./nM	τ_D	A_D	τ_{DA1}	A_{DA1}	$<\tau_{DA}>$	E_{FRET}
1	Tb alone	2800	1748	D in the absence of A (mono-exponential)			
2	6.0	2800	1526	1900	305	1900	0.32
3	8.0	2800	1414	1900	355	1900	0.32
4	10.0	2800	1431	1800	369	1800	0.36
average 2-4		2800		1870		1870	0.33
distance r (nm)				11.6		11.6	11.6

Maximum errors: $\Delta<\tau_{DA}>$ **= 70 µs (4 %)** Δr **= 0.2 nm (2 %)**

Acceptor channel R_0 **= 10.3 nm** **Fitted from** t_0 **= 0.05 to** t **= 6 ms**

Sample		Tb background		QD background			FRET parameter						averaged results	
		fixed	fixed	free	free	free	free	free	free	free	free	free		
#	Peptide conc./nM	τ_D	A_D	τ_{DA1}	A_{DA1}	k_{FRET-1}	τ_{DA2}	A_{DA2}	k_{FRET-2}	τ_{DA3}	A_{DA3}	k_{FRET-3}	$<\tau_{AD}>$	E_{FRET}
1	Tb alone	2700	112	D in the absence of A (mono-exponential)										
2	6.0	2700	100	30	872	0.0330	290	200	0.0031	2100	208	0.0001	2035	0.27
3	8.0	2700	93	29	925	0.0345	290	211	0.0031	2100	237	0.0001	2040	0.27
4	10.0	2700	94	32	874	0.0309	330	209	0.0027	2100	260	0.0001	2039	0.27
average 2-4		2700		30			303			2100			2038	0.27
distance r (nm)				4.9			7.2			12.4			12.1	12.1

Maximum errors: $\Delta<\tau_{DA}>$ **= 3 µs (1 %)** Δr **= 0.1 nm (1 %)**

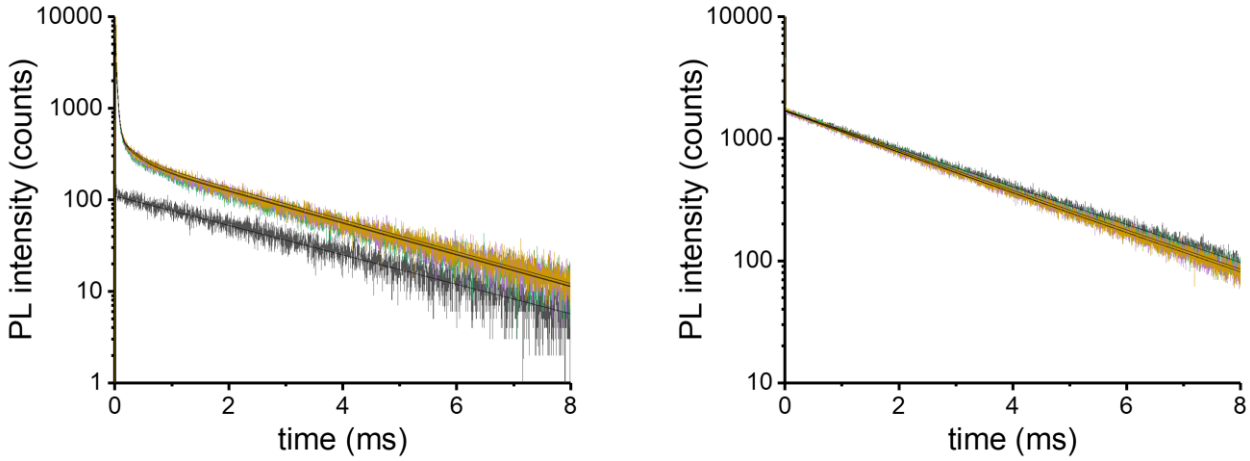

Figure 5.12. The PL decay curves of QD acceptor (left) and Tb donor (right) situated at **22 bps dsDNA** distances from each other. Black: pure Tb (some Tb luminescence is also visible in the acceptor detection channel due to spectral crosstalk); green: 6 nM peptide-DNA; purple: 8.0 nM peptide-DNA; yellow: 10.0 nM peptide-DNA.

Fit results (all decay times in µs):

Donor Channel R_0 = 10.3 nm Fitted from t_0 = 0.02 ms to t = 8 ms

Sample		Tb background		FRET parameter		averaged results	
		fixed	free	free	free		
#	Peptide conc./nM	τ_D	A_D	τ_{DA1}	A_{DA1}	$<\tau_{DA}>$	E_{FRET}
1	Tb alone	2800	1690	D in the absence of A (mono-exponential)			
2	6.0	2800	1349	2100	366	2100	0.25
3	8.0	2800	1320	1900	362	1900	0.32
4	10.0	2800	1312	1900	393	1900	0.32
average 2-4		2800		1970		1970	0.30
distance r (nm)				11.9		11.9	11.9

Maximum errors: $\Delta<\tau_{DA}>$ = 130 µs (7 %) Δr = 0.5 nm (5 %)

Acceptor channel R_0 = 10.3 nm Fitted from t_0 = 0.05 to t = 6 ms

Sample		Tb background		QD background			FRET parameter						averaged results	
		fixed	fixed	free	free	free	free	free	free	free	free	free		
#	Peptide conc./nM	τ_D	A_D	τ_{DA1}	A_{DA1}	k_{FRET-1}	τ_{DA2}	A_{DA2}	k_{FRET-2}	τ_{DA3}	A_{DA3}	k_{FRET-3}	$<\tau_{AD}>$	E_{FRET}
1	Tb alone	2700	112	D in the absence of A (mono-exponential)										
2	6.0	2700	89	27	6773	0.0367	250	280	0.0036	2400	164	0.0001	2342	0.16
3	8.0	2700	88	31	4902	0.0319	290	248	0.0031	2400	187	0.0001	2347	0.16
4	10.0	2700	87	30	5326	0.0330	290	264	0.0031	2400	194	0.0001	2346	0.16
average 2-4		2700		29			277			2400			2345	0.16
distance r (nm)				4.8			7.1			13.9			13.5	13.5

Maximum errors: $\Delta<\tau_{DA}>$ = 3 µs (1 %) Δr = 0.1 nm (1 %)

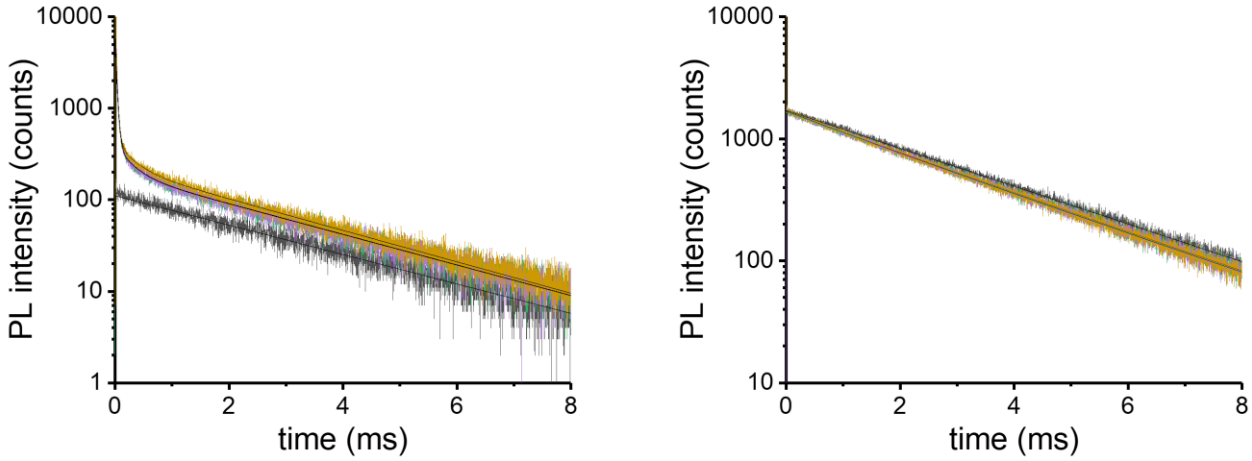

Figure 5.13. The PL decay curves of QD acceptor (left) and Tb donor (right) situated at **26 bps dsDNA** distances from each other. Black: pure Tb (some Tb luminescence is also visible in the acceptor detection channel due to spectral crosstalk); green: 6 nM peptide-DNA; purple: 8.0 nM peptide-DNA; yellow: 10.0 nM peptide-DNA.

Fit results (all decay times in µs):

Donor Channel R_0 = 10.3 nm Fitted from t_0 = 0.02 ms to t = 8 ms

Sample		Tb background		FRET parameter		averaged results	
		fixed	free	free	free		
#	Peptide conc./nM	τ_D	A_D	τ_{DA1}	A_{DA1}	$\langle\tau_{DA}\rangle$	E_{FRET}
1	Tb alone	2800	1708	D in the absence of A (mono-exponential)			
2	6.0	2800	1368	1900	286	1900	0.32
3	8.0	2800	1348	1900	304	1900	0.32
4	10.0	2800	1353	1700	334	1700	0.39
average 2-4		2800		1830		1830	0.35
distance r (nm)				11.4		11.4	11.5

Maximum errors: $\Delta\langle\tau_{DA}\rangle$ = 130 µs (7 %) Δr = 0.3 nm (3 %)

Acceptor channel R_0 = 10.3 nm Fitted from t_0 = 0.05 to t = 6 ms

Sample		Tb background		QD background			FRET parameter						averaged results	
		fixed	fixed	free	free	free	free	free	free	free	free	free		
#	Peptide conc./nM	τ_D	A_D	τ_{DA1}	A_{DA1}	k_{FRET-1}	τ_{DA2}	A_{DA2}	k_{FRET-2}	τ_{DA3}	A_{DA3}	k_{FRET-3}	$\langle\tau_{AD}\rangle$	E_{FRET}
1	Tb alone	2700	113	D in the absence of A (mono-exponential)										
2	6.0	2700	92	30	4548	0.0330	280	202	0.0032	2500	103	0.00004	2507	0.10
3	8.0	2700	90	29	5518	0.0341	280	209	0.0032	2500	107	0.00004	2444	0.13
4	10.0	2700	89	29	4581	0.0341	290	221	0.0031	2400	138	0.00006	2409	0.14
average 2-4		2700		29			283			2467			2453	0.12
distance r (nm)				4.8			7.2			14.4			14.3	14.3

Maximum errors: $\Delta\langle\tau_{DA}\rangle$ = 54 µs (3 %) Δr = 0.4 nm (3 %)

Table 5.2. Tb-to-QD center-to-center distances (r) and FRET-efficiencies (E_{FRET}) as calculated by the lifetime fits (**Figure 5.3** to **Figure 5.13**) and the equations in **5.3.3**.

Construct	QD ACCEPTOR CHANNEL				Tb DONOR CHANNEL			
	r (nm)	Δr (nm)	E_{FRET}	ΔE_{FRET}	r (nm)	Δr (nm)	E_{FRET}	ΔE_{FRET}
0 nt 3'FRET	7.4	0.1	0.88	0.01	7.6	0.3	0.86	0.03
2 nt 3'FRET	7.6	0.1	0.86	0.02	7.6	0.1	0.86	0.02
4 nt 3'FRET	8	0.1	0.82	0.02	8.1	0.1	0.81	0.02
6 nt 3'FRET	8.3	0.1	0.79	0.02	8.4	0.3	0.77	0.08
10 nt 3'FRET	8.7	0.1	0.73	0.03	8.6	0.1	0.75	0.03
14 nt 3'FRET	9.2	0.1	0.66	0.03	9.3	0.1	0.65	0.03
10 nt 5'FRET	9.5	0.2	0.62	0.06	9.6	0.5	0.60	0.15
14 nt 5'FRET	11.5	0.2	0.34	0.05	11.4	0.3	0.35	0.07
18 nt 5'FRET	12.1	0.1	0.28	0.02	11.6	0.2	0.33	0.05
22 nt 5'FRET	13.5	0.1	0.16	0.01	11.9	0.5	0.30	0.11
26 nt 5'FRET	14.3	0.4	0.12	0.04	11.4	0.3	0.35	0.07

5.3.4 Time-Resolved Tb-to-QD FRET DNA-Nanoruler and Distance Modeling.

For all 11 configurations, PL decays of both the Tb donor and the QD625 acceptor were measured in a time range between 0 and 8 ms (**Figures 5.3** to **5.13**). To distinguish between FRET and non-FRET contributions (from non-quenched Tb and directly excited QDs) and to be able to analyze various independent PL decay curves, the concentrations of Tb-DNA and QD625 were kept constant (20 nM Tb-DNA and 0.5 nM QD625) whereas the concentration of the peptide-appended main DNA was varied (0, 2, 4, 6, 8, 10, and 20 nM). This strategy provided one background and six independent FRET measurements per configuration and a proof-of-concept system for a quantitative (signal over concentration) DNA hybridization assay. **Figure 5.14** shows representative QD625 PL decays for all configurations at constant concentrations of 20 nM peptide-DNA (PL decays for both Tb and DQ625 at different peptide-DNA concentrations are shown in **Figures 5.3** to **5.13**). As expected from FRET theory, the increasing Tb-to-QD distances led to increasing FRET-sensitized lifetimes of the PL decays, all of which can be readily distinguished without lifetime fitting of the curves. Such fine-tuning of PL decay curves via displacement of the Tb donor by only a few nt demonstrates the high distance sensitivity of FRET and the possibility to extend nanoparticle-based temporal multiplexing beyond two distinct PL decays[173].

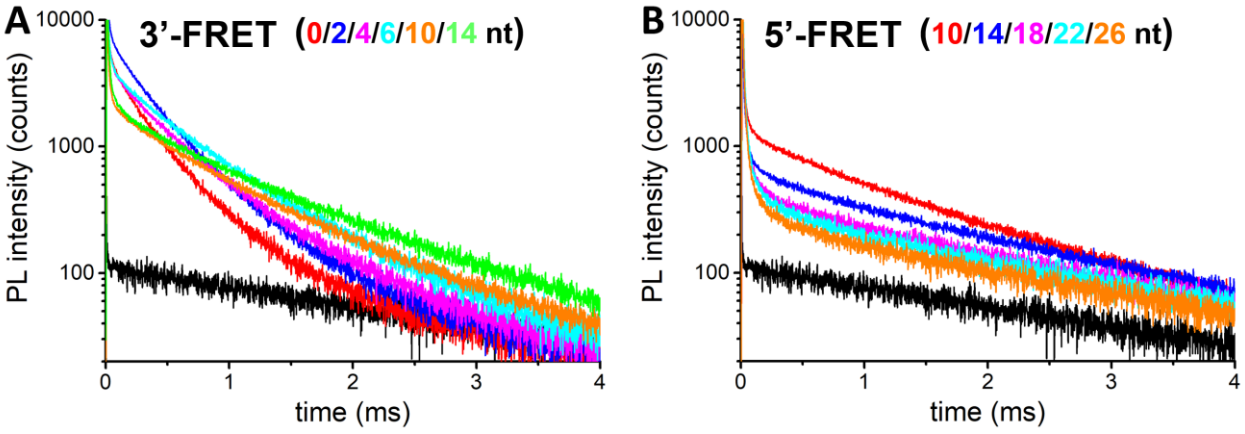

Figure 5.14. QD625 PL decay curves of the different FRET configurations (**A**: ssDNA or 3'-FRET, **B**: dsDNA or 5'-FRET) shown in **Figure 5.1**. Concentrations of peptide-DNA were 20 nM for all curves. PL decay curves of different concentrations for both Tb and QD625 are shown in **Figures 5.3** to **5.13**. Black curves present spectral crosstalk of Tb (only Tb-DNA without peptide-DNA and QD625) inside the QD625 detection channel.

In order to understand the orientation of the ssDNA and dsDNA on the nanoparticle surface and the distance tunability or sensitivity (distance per nt) in these two open and hybridized configurations, we fitted the decay curves for three peptide-DNA concentrations (6, 8, and 10 nM) for both FRET-sensitized QD625 PL and FRET-quenched Tb PL. All PL curves showed multiexponential decays (**Equations 5.3** and **5.4**), which consist of a monoexponential contribution from unquenched Tb (τ_D = 2.75±0.05 ms, from Tb that do not participate in FRET) and a multiexponential contribution from FRET owing to a Tb-to-QD distance distribution caused by the flexibility of the DNA and the linker between Tb and DNA (cf. **Figure 5.1 bottom**). Although the single FRET-sensitized PL lifetimes (τ_{AD}) of QD625 and FRET-quenched PL lifetime (τ_{DA}) of Tb are the same, the average FRET-sensitized acceptor lifetime must be corrected by the FRET rates of each single component (**Equations 5.8** and **5.9**). The average FRET lifetimes ($<\tau_{AD}>$ and $<\tau_{DA}>$) can then be used to calculate the average Tb-to-QD distance (**Equations 5.6** and **5.10**) and FRET efficiencies **(Equations 5.7** and **5.11**). Due to the much weaker PL background of unquenched Tb in the QD acceptor detection channel (cf. **Figures 5.3** to **5.13**), this channel usually provides better fitting results[173][178]. Tb-to-QD distances were also calculated by biomolecular modeling. Closest and furthest distances for both parallel and vertical orientation of the peptide-DNA on the QD625 surface were calculated (**Table 5.3**).

Table 5.3A: Minimum (near) and maximum (far) Tb-to-QD distances for DNA attached vertically or parallel to the QD surface as calculated from biomolecular modeling

Construct	QD radius (nm)	QD-DHLA-PEG radius (nm)	vertical		parallel		vertical		parallel	
			distance from surface		distance from surface		distance from center		distance from center	
			near	far	near	far	near	far	near	far
0 nt 3'FRET	4.65	6.02	0.9	3.9	0.5	5.3	5.5	8.6	5.1	9.9
2 nt 3'FRET	4.65	6.02	0.9	5.1	0.8	5.1	5.5	9.7	5.4	9.8
4 nt 3'FRET	4.65	6.02	1.5	6.2	0.8	3.9	6.2	10.8	5.4	8.6
6 nt 3'FRET	4.65	6.02	2.8	7	1.2	5.3	7.4	11.7	5.9	10
10 nt 3'FRET	4.65	6.02	3.6	7.8	0.8	5.6	8.2	12.4	5.4	10.3
14 nt 3'FRET	4.65	6.02	4.8	9.2	0.7	4.2	9.4	13.9	5.4	8.8
10 nt 5'FRET	4.65	6.02	2.9	7.1	0.2	4	7.6	11.8	4.8	8.7
14 nt 5'FRET	4.65	6.02	4.9	9	0.2	5.6	9.5	13.7	4.8	10.2
18 nt 5'FRET	4.65	6.02	5.4	9.6	0.9	5	10.1	14.3	5.5	9.7
22 nt 5'FRET	4.65	6.02	6.6	11.7	1.6	6.5	11.2	16.4	6.3	11.2
26 nt 5'FRET	0	0	0	0	0	0	0	0	0	0

Table 5.3B: Average Tb-to-QD center-to-center distances as calculated from the minimum and maximum values of **Table 5.3A**.

Construct	vertical		parallel	
	average distance from center (nm)	ERROR (nm)	average distance from center (nm)	ERROR (nm)
0 nt 3'FRET	7.1	1.6	7.5	2.4
2 nt 3'FRET	7.6	2.1	7.6	2.2
4 nt 3'FRET	8.5	2.3	7.0	1.6
6 nt 3'FRET	9.6	2.2	8.0	2.1
10 nt 3'FRET	10.3	2.1	7.9	2.5
14 nt 3'FRET	11.7	2.3	7.1	1.7
10 nt 5'FRET	9.7	2.1	6.8	2.0
14 nt 5'FRET	11.6	2.1	7.5	2.7
18 nt 5'FRET	12.2	2.1	7.6	2.1
22 nt 5'FRET	13.8	2.6	8.8	2.5
26 nt 5'FRET	0.0	0.0	0.0	0.0

The average theoretical distances and the FRET distances (calculated from QD625 acceptor PL decays – the Tb donor PL results, which are very similar to the QD acceptor results for shorter distances but deviate for longer distances, are shown in **Figure 5.16**) of all configurations are shown in **Figure 5.15**. For both configurations (single and double-stranded) the FRET results show a linearly increasing Tb-to-QD distance with the number of bases. With 0.31 nm per base pair, the dsDNA distance increase is approximately twice as large as the one of ssDNA (0.15 nm per base). While the dsDNA distance is in very good agreement with the

literature (~0.33 nm length per base pair)[179] and confirms the excellent long-range precision of our FRET nanoruler, the one for ssDNA is relatively short compared to previous studies. In a single-molecule FRET approach, Murphy *et al*. investigated a similar ssDNA-dsDNA system, which contained a Cy3 donor on the 3' end of ssDNA and a Cy5 acceptor on the 5' end of a 18 nt long ssDNA probe that was hybridized to the ssDNA and attached via a 3'-biotin functionalization to a streptavidin-coated microscope slide[180]. At similar buffer conditions (12 ~ 20 mM Tris, pH 8.0, 400 mM NaCl) they found ssDNA lengths of 4.4, 5.0, 5.3, 5.6, 6.0, and 7.1 nm for 10, 15, 17, 23, 27, and 40 nt lengths of poly dT ssDNA, respectively. These values correspond to 0.44, 0.33, 0.31, 0.24, 022, and 0.18 nm per base and taking into account that our ssDNA lengths varied between 0 and 14 nt, a distance above 0.33 nm per base would have been expected from the single-molecule FRET study. On the other hand, our ssDNA had a variable sequence whereas the single-molecule study investigated poly dT ssDNA. Moreover, the conditions of a DNA attached to a nanoparticle (on the ssDNA end) in solution could be quite different from a DNA attached to a microscopy slide (on the dsDNA end). Taking into account the almost perfect linearity determined by 5 different lengths over 14 nt and the relatively good agreement with the model data (**Figure 5.15A**), it can be assumed that the value of 0.15 nm per base is realistic for our QD-DNA system. This unexpectedly short distance also shows the necessity of measuring the actual DNA conformation on a nanoparticle surface instead of assuming a value from a study with similar but still significantly different conditions.

Another very interesting FRET information concerns the orientation of the DNA on the QD surface. The ssDNA extension can be well approximated by an average of the theoretical parallel and vertical orientations, which presents a flexible ssDNA that can take any orientation on the QD surface. The same behavior should be found for dsDNA if the peptide linker between DNA and QD625 would be responsible for the flexibility (functioning as a hinge). However, the dsDNA extension is almost a perfect reproduction of the theoretical vertical orientation, which presents a stiff dsDNA that does not bend on the QD surface. Although this different behavior between ssDNA and dsDNA is not surprising, it cannot be simply taken for granted for DNA attached to the surface of a nanoparticle. The experimental determination by FRET at low concentrations and physiological conditions provides highly important information concerning the natural structure of DNA-nanoparticle conjugates. As many DNA-based nanosensors depend on distances and conformations that change from single ssDNA (probe alone) to dsDNA (probe-target hybridization), knowledge about the conformational behavior

within such a sensor will be extremely valuable to design and optimize the biological recognition and signal generation.

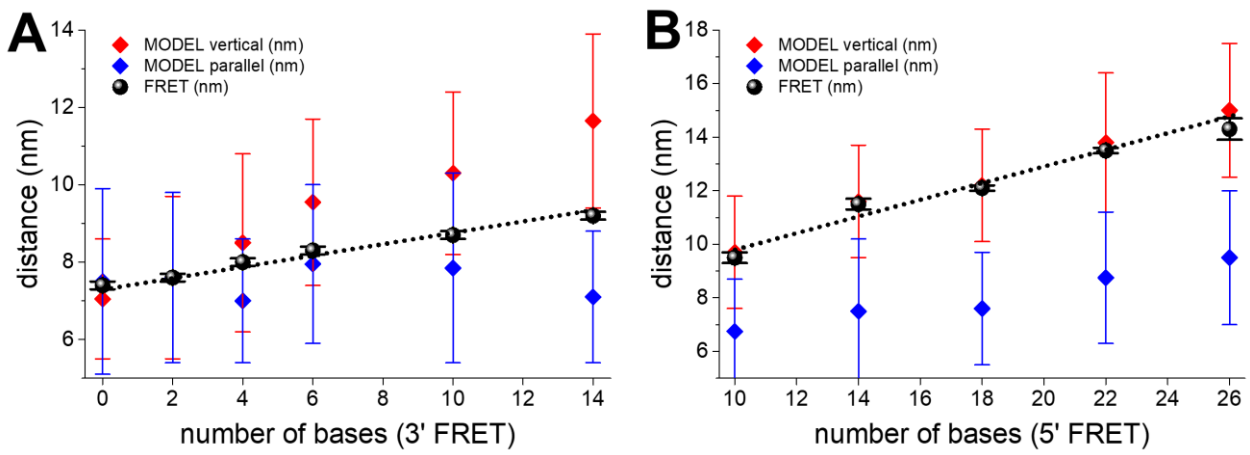

Figure 5.15. Tb-donor-to-QD-acceptor distances measured by FRET-sensitized PL of QD625 (black dots) and modeled in vertical (red diamonds) and parallel (blue diamonds) configuration (see **Figure 5.1**) for 3'FRET (**A**) and 5'-FRET (**B**). Error bars for models present the closest and furthest distance of Tb from the QD in the two different configurations. Error bars for FRET present maximum PL lifetime errors from three measurements with different concentrations. See **Figures 5.3** to **5.13** and **Tables 5.2** and **5.3** for details.

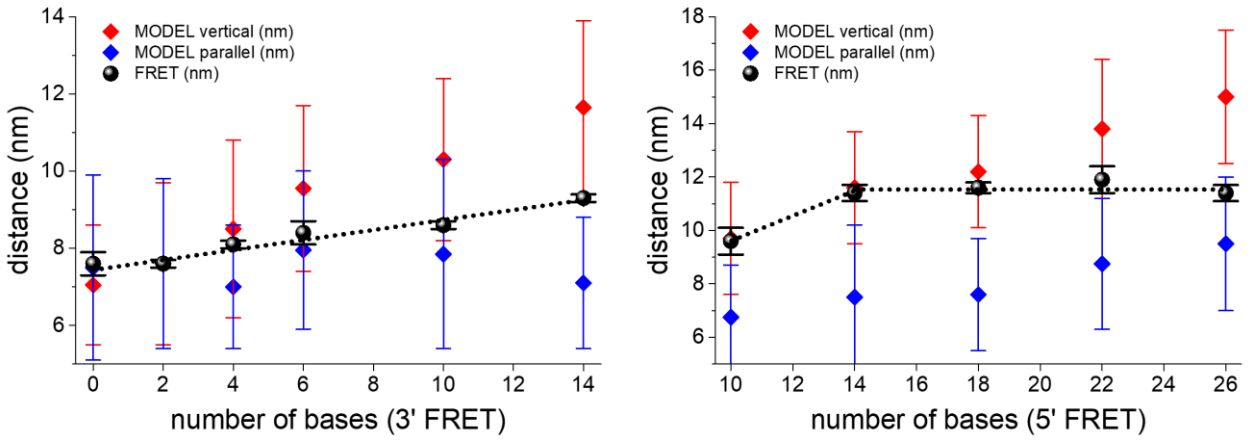

Figure 5.16. Tb-donor-to-QD-acceptor distances measured by FRET-quenched PL of Tb (black dots) and modeled in vertical (red diamonds) and parallel (blue diamonds) configuration (see **Figure 5.1**) for 3'FRET (**A**) and 5'-FRET (**B**). Error bars for models present the closest and furthest distance of Tb from the QD in the two different configurations. Error bars for FRET present maximum PL lifetime errors from three measurements with different concentrations. See **Figures 5.3** to **5.13** and **Tables 5.2** and **5.3** for details.

5.3.5 Prototypical DNA Hybridization Assays

In addition to the structural and conformational information, the precise distance tuning also allows for the generation of many distinct decay curves of FRET-sensitized QD625 PL (cf. **Figure 5.14**). Such PL decays can be used for higher order multiplexed quantification of biomarkers or optical barcoding of cells, as recently demonstrated by time-gated PL detection of other Tb-QD[173], Tb-dye[181], or Tb/Eu-QD[133] FRET pairs. To demonstrate target quantification by concentration-dependent FRET ratios (ratio of time-gated intensities of QD625 and Tb PL) we used peptide-DNA concentrations between 0 and 10 nM while keeping all other assay components constant. As shown in **Figure 5.17**, all 11 configurations provided a FRET-ratio increase (linear up to at least 6 nM) over peptide-DNA concentration. Despite the relatively low assay sensitivities (slopes of the calibration curves) for the very long distance configurations (i.e., 18, 22, and 26 nt), all FRET constructs could be used for quantifying DNA at low nanomolar concentrations. Although such systems need to be adapted to real targets (in our case both QD-peptide-DNA and Tb-DNA were DNA probes), the proof-of-concept hybridization assays demonstrated the possible application of DNA-based Tb-to-QD distance tuning for higher order temporal multiplexing that can also be combined with several different QD colors[182].

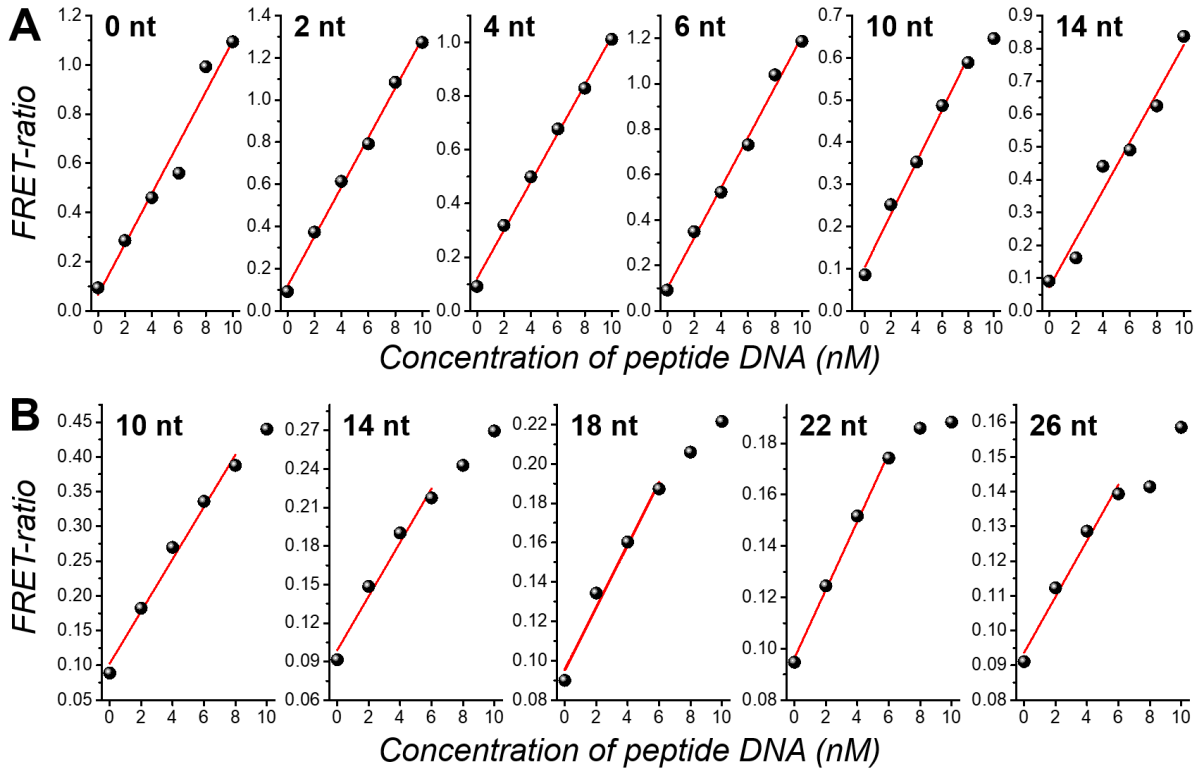

Figure 5.17. Calibration curves of prototypical DNA hybridization assays showing increasing time-gated (0.1 to 2 ms) PL FRET ratios with increasing peptide-DNA concentrations for all 3'-FRET (A) and 5'-FRET (B) configurations.

5.4 Conclusion

In summary, we have extensively investigated the orientation of a 31 nt long DNA attached via a peptide-His_6 linker to a QD by Tb-to-QD FRET and biomolecular modeling. Our results show that time-resolved analysis of FRET-sensitized QD PL can be used to precisely measure the distances along the QD-DNA conjugate by hybridization of different Tb-DNA probes at different positions of the QD-DNA. Long-range QD-to-Tb distances between ca. 7 and 14 nm (from center to center) significantly extended beyond previous FRET systems. The detailed investigation of 11 different DNA configurations on the nanoparticle surface and the comparison of the FRET results with biomolecular modeling allowed us to extract important conformational information from the FRET data. In single-stranded conformation, the DNA extended from the QD with ~0.15 nm per base and the flexible ssDNA could take any orientation between parallel and vertical in regard to the QD surface. In double-stranded conformation, the DNA extended with ~0.31 nm per base pair and the orientation was purely vertical, reflecting the stiffness of dsDNA. Determination of different lengths and orientations of ssDNA and dsDNA on nanoparticle surfaces under physiological conditions and at low nanomolar concentrations is highly important for efficient development and optimization of hybridization-based DNA nanosensors and our Tb-to-QD FRET ruler provided very useful information that should in principle be transferable to any other DNA-nanoparticle conjugate. In addition to the precise conformational FRET analysis, we showed that the DNA distance tuning can be used to generate many distinct PL decay curves (with different average PL lifetimes), whose intensities were dependent on the peptide-DNA concentration, even for configurations with very long donor-acceptor distances (~14 nm). Prototypical DNA-hybridization assays for all 11 configurations suggest that these Tb-to-QD FRET DNA constructs have a strong potential to significantly extend the multiplexing range of the recently developed time-gated temporal optical multiplexing concept. Our results demonstrate that QDs, despite their relatively large sizes, can be used for precise conformational analysis and extended temporal multiplexed detection of nucleic acid biomarkers and that the Tb-QD donor-acceptor FRET pair presents a useful optical tool for both diagnostic and biophysical applications.

6. Summary and Outlook

This thesis presents three successful applications of FRET in two distinct research fields. The first two are multiplexed LTC-to-Dye FRET biosensors for cancer related nucleic acid biomarker detection based on amplification methods and time-gated measurements. We used two strategies to achieve multiplexed detection, temporal-multiplexed detection based on distinguishable decay times of a single LTC-to-dye FRET pair and spectral-temporal multiplexed detection based on different emission spectra of different color dyes and different decay times of the same LTC-to-dye pair. Hybridization chain reaction and rolling circle amplification methods were combined for high sensitivity and for placing Tb donors and dye acceptors at controlled distances within the amplified DNA production. Time-gated measurements were used to collect the PL intensities and calculate the contributions of different analytes in different time-gated windows by a simple matrix calculation. The last one is single and double strand QD conjugated DNA conformation study by LTC-to-QD FRET lifetime. The results demonstrate that QDs can be used for temporal multiplexed detection and Tb-to-QD FRET DNA construct have a strong potential to significantly extend the multiplexing range of the time-gated temporal multiplexing concept. All of these assays are homogeneous, no washing and separation needed even with the amplified assay. All of them are specific, can distinguish very similar sequences. All these detecting techniques are easily transferable to other nucleic acid targets.

In the first work, the multiplexing capacity is not limited to two, we can also try to use this technique for triplex assays and the capacity in real samples also should be figured out in future investigations. In the second work, we have detected four different DNAs, which are the DNA-equivalents of the miRNAs. We did not detect miRNA directly because the calibration curves were not linear. It is difficult to do the matrix calculation with exponential functions, so more optimization should be done for miRNA assays. This first demonstration of spectral-temporal multiplexing quantified only four DNAs by combining two spectral and two temporal components, but when more different acceptor and more time-gated windows are added, the number of detectable targets in a single sample will be greatly increased. Tb-to-QD FRET DNA construct not only presents a valuable alternative to DNA conformation analysis techniques but also have a strong potential to be used for developing biosensors to quantify DNA at low nanomolar concentrations. The proof-of-concept hybridization assays demonstrated the

possible application of DNA-based Tb-to-QD distance tuning for higher order temporal multiplexing that can also be combined with several different QD colors.

Contributions

For this work, I performed the experiments, analyzed the data, and wrote the manuscript.

7. Appendix

7.1 Abbreviations

BSA	bovine serum albumin
ChA	acceptor channel
ChD	donor channel
DHLA	dihydrolipoic acid
DNA	deoxyribonucleic acid
dsDNA	double strands DNA
FDA	Food and Drug Administration
FLIM	fluorescence lifetime imaging
FRET	Förster resonance energy transfer
FWHM	full-width-at-half-maximum
His6	hexahistidine
HPLC	high performance liquid chromatography
IR	infrared
Ln	lanthanides
LOD	limit of detection
LTC	luminescent terbium complex
miRNA	microRNA
NGS	next generation sequencing
NHS	N-hydroxysuccinimide
NIR	near infrared
NMR	nuclear magnetic resonance
NP	nanoparticle
PEG	poly(ethylene glycol)
PL	photoluminescence
PMT	photomultiplier tube

POCT	point-of-care testing
QD	quantum dot
qRT-PCR	quantitative reverse transcription-polymerase chain reaction
RCA	rolling circle amplification
ref.	reference
RNA	ribonucleic acid
sAv	streptavidin
SDS-PAGE	sodium dodecyl sulfate polyacrylamide gel electrophoresis
ssDNA	single strand DNA
TCSPC	time-correlated single-photon counting
TEM	transmission electron microscopy
TG	time-gated
Tm	melting temperature
TR	time-resolved
UC	upconversion
UCNP	upconversion nanoparticle
UV	ultraviolet
Vis	visible

7.2 LTC-ssDNA conjugation protocol (a typical protocol, suitable for all ssDNAs used in this work)

Conjugation:

7.9 μL Carbonate buffer (pH 9.0) + 10 μL ssDNA (100 μM) + 2.1 μL L4Tb-NHS (in DMF, 8 mM) in 0.5 mL Eppendorf-tube.

Concentration of ssDNA in conjugation solution is 50 μM, reaction ratio LTC/ ssDNA= 16/1.

- Shortly vortex
- Intelli Mixer: prewetting tube-walls by rotating the tube
  sample in alu foil
  program F1 - 30 rpm
- Incubation time: overnight

Purification:

Purification buffer: 100 mM HEPES, pH 7.4

A. Desalting Spin Column Preparation

1. Remove column's bottom closure and loosen cap (do not remove cap).
2. Place column in a 2.0 mL collection tube. Centrifuge at 1500 × g for 1 minute to remove storage solution.
3. Place a mark on the side of the column where the compacted resin is slanted upward. Place column in the microcentrifuge with the mark facing outward in all subsequent centrifugation steps.
4. Add 300 μL of purification buffer on top of the resin bed. Centrifuge at 1500 × g for 1 minute to remove buffer.
5. Repeat Step 4 two to three additional times, discarding buffer from the collection tube.

B. Sample Loading

1. Place column in a new collection tube, remove the cap and apply 100 μL of sample (20 μL sample plus 80 μL purification buffer) to the top of the compact resin bed.
2. Centrifuge at 1500 × g for 2 minutes to collect the sample. Discard desalting column after use.

Repeat A and B two more times to fully separate free LTC from reporter 20a-LTC sample (checked with UV table)

Characterization:

Absorbance measurement by PerkinElmer reader

PL emission and lifetime measurement by FT300

7.3 Cy 3.5-ssDNA conjugation protocol (a typical protocol, suitable for all ssDNAs used in this work)

Conjugation:

7.9 μL Carbonate buffer (pH 9.0) + 10 μL ssDNA (100 μM) + 2.1 μL Cy 3.5-NHS (in DMF, 6.6 mM) in 0.5 mL Eppendorf-tube

concentration of ssDNA in conjugation solution is 50 μM, reaction ratio Cy 3.5/ssDNA= 14/1

- shortly vortex
- Intelli Mixer: prewetting tube-walls by rotating the tube
  sample in alu foil
  program F1 - 30 rpm
- incubation time: overnight

Purification:

Purification buffer: 100 mM HEPES, pH 7.4

A. Desalting Spin Column Preparation

1. Remove column's bottom closure and loosen cap (do not remove cap).

2. Place column in a 2.0 mL collection tube. Centrifuge at 1500 × g for 1 minute to remove storage solution.

3. Place a mark on the side of the column where the compacted resin is slanted upward. Place column in the microcentrifuge with the mark facing outward in all subsequent centrifugation steps.

4. Add 300 μL of purification buffer on top of the resin bed. Centrifuge at 1500 × g for 1 minute to remove buffer.

5. Repeat Step 4 two to three additional times, discarding buffer from the collection tube.

B. Sample Loading

1. Place column in a new collection tube, remove the cap and apply 100 μL of sample (20 μL sample plus 80 μL purification buffer) to the top of the compact resin bed.

2. Centrifuge at 1500 × g for 2 minutes to collect the sample. Discard desalting column after use.

Repeat A and B two more times to fully separate free LTC from reporter 20a-LTC sample (checked with UV table)

Characterization:

Absorbance measurement by PerkinElmer reader

PL emission and lifetime measurement by FT300

7.4 Cy 5.5-ssDNA conjugation protocol (a typical protocol, suitable for all ssDNAs used in this work)

Conjugation:

9.0 μL Carbonate buffer (pH 9.0) + 10 μL ssDNA (100 μM) + 1.0 μL Cy 5.5-NHS (in DMF, 16.6 mM) in 0.5 mL Eppendorf-tube

concentration of ssDNA in conjugation solution is 50 μM, reaction ratio Cy 5.5/ ssDNA= 16/1

- shortly vortex
- Intelli Mixer: prewetting tube-walls by rotating the tube
  sample in alu foil
  program F1 - 30 rpm
- incubation time: overnight

Purification:

Purification buffer: 100 mM HEPES, pH 7.4

A. Desalting Spin Column Preparation

1. Remove column's bottom closure and loosen cap (do not remove cap).

2. Place column in a 2.0 mL collection tube. Centrifuge at 1500 × g for 1 minute to remove storage solution.

3. Place a mark on the side of the column where the compacted resin is slanted upward. Place column in the microcentrifuge with the mark facing outward in all subsequent centrifugation steps.

4. Add 300 μL of purification buffer on top of the resin bed. Centrifuge at 1500 × g for 1 minute to remove buffer.

5. Repeat Step 4 two to three additional times, discarding buffer from the collection tube.

B. Sample Loading

1. Place column in a new collection tube, remove the cap and apply 100 μL of sample (20 μL sample plus 80 μL purification buffer) to the top of the compact resin bed.

2. Centrifuge at 1500 × g for 2 minutes to collect the sample. Discard desalting column after use.

Repeat A and B two more times to fully separate free LTC from reporter 20a-LTC sample (checked with UV table)

Characterization:

Absorbance measurement by PerkinElmer reader

PL emission and lifetime measurement by FT300

7.5 Instrument

All FRET measurements were performed by two fluorescence plate readers. The first plate reader was a modified KRYPTOR compact PLUS (Cezanne/Thermo Fisher Scientific, France) using 500 detection bins of 2 µs integration time. The system has an integrated pulsed nitrogen laser with an excitation wavelength of 337 nm and a repetition rate of 20 Hz. The second fluorescence plate reader is a prototype from Edinburgh Instruments (UK) developed during a joined project and referred in this work as EI plate reader. The system allows time-resolved FRET assay measurements using 4000 detection bins of 2 µs integration time. The excitation source was a pulsed nitrogen laser (MNL 100, LTB Berlin) with an excitation wavelength of 337 nm and a repetition rate of 20 Hz.

Dichroic mirrors and bandpass filter

The instrumental construction for all used plate readers is shown in **Figure 7.1**. After sample excitation, a dichroic mirror is used to separate the emission signals from the sample into two individual detection channels. This separation allows the simultaneous measurement of the FRET acceptor signals (ChA) and the FRET donor signals (ChD) using two photomultiplier tubes (PMTs). A further selection of the emission wavelengths inside the channels is obtained by the use of bandpass filters, which are optimized for the emission detection of the LTC and for the Cyanine dyes or QD.

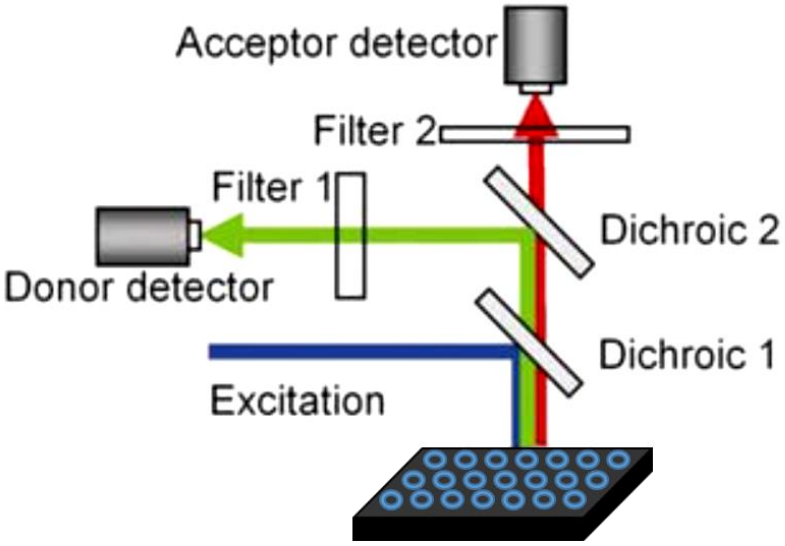

Figure 7.1. Simplified schematic instrumental setup of the used fluorescence plate readers.

8. Bibliography

[1] D. Barh, A. Carpi, M. Verma, and M. Gunduz, *Cancer biomarkers: Minimal and noninvasive early diagnosis and prognosis*. CRC Press, 2014.

[2] D. P. Bartel, "MicroRNAs: genomics, biogenesis, mechanism, and function", *Cell*, vol. 116, no. 2, pp. 281-297, 2004.

[3] I. L. Medintz and N. Hildebrandt, *FRET-Förster resonance energy transfer: from theory to applications*. John Wiley & Sons, 2013.

[4] T. W. J. Gadella, *FRET and FLIM techniques*, vol. 33. Elsevier, 2011.

[5] Y. Wang, P. Howes, E. Kim, C. Spicer, M. Thomas, Y. Lin, S. Crowder, I. Pence and M. Stevens, "Duplex-Specific Nuclease-Amplified Detection of MicroRNA Using Compact Quantum Dot–DNA Conjugates", *ACS Appl. Mater. Interfaces*, vol. 10, no. 34, pp. 28290-28300, 2018.

[6] Y. Zhang and C. Zhang, "Sensitive detection of microRNA with isothermal amplification and a single-quantum-dot-based nanosensor", *Anal. Chem.*, vol. 84, no. 1, pp. 224-231, 2011.

[7] Z. Jin, D. Geißler, X. Qiu, K. D. Wegner, and N. Hildebrandt, "A Rapid, Amplification-Free, and Sensitive Diagnostic Assay for Single-Step Multiplexed Fluorescence Detection of MicroRNA", *Angew. Chem. Int. Ed.*, vol. 54, no. 34, pp. 10024-10029, 2015.

[8] X. Qiu and N. Hildebrandt, “Rapid and multiplexed microRNA diagnostic assay using quantum dot-based forster resonance energy transfer”, *ACS Nano*, vol. 9, no. 8, pp. 8449-8457, 2015.

[9] S. Li, L. Xu, W. Ma, X. Wu, M. Sun, H. Kuang, L. Wang, N. A. Kotov, and C. Xu, “Dual-mode ultrasensitive quantification of microRNA in living cells by chiroplasmonic nanopyramids self-assembled from gold and upconversion nanoparticles”, *J. Am. Chem. Soc.*, vol. 138, no. 1, pp. 306-312, 2015.

[10] N. Hildebrandt, K. D. Wegner, and W. R. Algar, “Luminescent terbium complexes: Superior Förster resonance energy transfer donors for flexible and sensitive multiplexed biosensing”, *Coord. Chem. Rev.*, vol. 273, pp. 125-138, 2014.

[11] D. Geißler and N. Hildebrandt, “Lanthanide Complexes in FRET Applications”, *Curr. Org. Chem.*, vol. 1, no. 1, pp. 17-35, 2011.

[12] J. -C. G. Bünzli, “Benefiting from the Unique Properties of Lanthanide Ions”, *Acc. Chem. Res.*, vol. 39, no. 1, pp. 53-61, 2006.

[13] B. Hötzer, I. L. Medintz, and N. Hildebrandt, “Fluorescence in Nanobiotechnology: Sophisticated Fluorophores for Novel Applications”, *Small*, vol. 8, no. 15, pp. 2297-2326, 2012.

[14] K. E. Sapsford, L. Berti, and I. L. Medintz, “Materials for Fluorescence Resonance Energy Transfer Analysis: Beyond Traditional Donor–Acceptor Combinations”, *Angew. Chem. Int. Ed.*, vol. 45, no. 28, pp. 4562-4589, 2006.

[15] S. H. Kim, J. R. Gunther, and J. A. Katzenellenbogen, “Monitoring a Coordinated Exchange Process in a Four-Component Biological Interaction System: Development of a Time-Resolved Terbium-Based One-Donor/Three-Acceptor Multicolor FRET System”, *J. Am. Chem. Soc.*, vol. 132, no. 13, pp. 4685-4692, 2010.

[16] D. Geißler, S. Stufler, H.-G. Löhmannsröben, and N. Hildebrandt, “Six-Color Time-Resolved Förster Resonance Energy Transfer for Ultrasensitive Multiplexed Biosensing”, *J. Am. Chem. Soc.*, vol. 135, no. 3, pp. 1102-1109, 2013.

[17] T. Kippeny, L. A. Swafford, and S. J. Rosenthal, “Semiconductor Nanocrystals: A Powerful Visual Aid for Introducing the Particle in a Box”, *J. Chem. Educ.*, vol. 79, no. 9, p. 1094, 2002.

[18] C. B. Murray, C. R. Kagan, and M. G. Bawendi, “Synthesis and Characterization of Monodisperse Nanocrystals and Close-Packed Nanocrystal Assemblies”, *Annu. Rev. Mater. Sci.*, vol. 30, no. 1, pp. 545-610, 2000.

[19] D. Geißler, S. Linden, K. Liermann, K. D. Wegner, L. J. Charbonnière, and N. Hildebrandt, “Lanthanides and Quantum Dots as Förster Resonance Energy Transfer Agents for Diagnostics and Cellular Imaging”, *Inorg. Chem.*, vol. 53, no. 4, pp. 1824-1838, 2014.

[20] N. Hildebrandt, L. J. Charbonnière, M. Beck, R. F. Ziessel, and H.-G. Löhmannsröben,

"Quantum Dots as Efficient Energy Acceptors in a Time-Resolved Fluoroimmunoassay", *Angew. Chem. Int. Ed.*, vol. 44, no. 46, pp. 7612-7615, 2005.

[21] Biomarkers Definitions Working Group, "Biomarkers and surrogate endpoints: Preferred definitions and conceptual framework", *Clin. Pharmacol. Ther.*, vol. 69, no. 3, pp. 89-95, 2001.

[22] W. H. Organization and I. P. on C. Safety, "Biomarkers in risk assessment : validity and validation", 2001.

[23] K. E. Sapsford, Ž. Težak, M. Kondratovich, M. A. Pacanowski, I. Zineh, and E. Mansfield, "Biomarkers to improve the benefit/risk balance for approved therapeutics: a US FDA perspective on personalized medicine", *Ther. Deliv.*, vol. 1, no. 5, pp. 631-641, 2010.

[24] S. Y. Loke and A. S. G. Lee, "The future of blood-based biomarkers for the early detection of breast cancer", *Eur. J. Cancer*, vol. 92, pp. 54-68, 2018.

[25] A. N. Bhatt, R. Mathur, A. Farooque, A. Verma, and B. S. Dwarakanath, "Cancer biomarkers - current perspectives", *Indian J. Med. Res.*, vol. 132, no. 8, pp. 129-149, 2010.

[26] R. R. Breaker, "Natural and engineered nucleic acids as tools to explore biology", *Nature*, vol. 432, no. 7019, pp. 838-845, 2004.

[27] D. S. Wilson and J. W. Szostak, "In Vitro Selection of Functional Nucleic Acids", *Annu. Rev. Biochem.*, vol. 68, no. 1, pp. 611-647, 1999.

[28] H. Liang, X. Zhang, Y. Lv, L. Gong, R. Wang, X. Zhu, R. Yang, and W. Tan, "Functional DNA-Containing Nanomaterials: Cellular Applications in Biosensing, Imaging, and Targeted Therapy", *Acc. Chem. Res.*, vol. 47, no. 6, pp. 1891-1901, 2014.

[29] Y. Lee, M. Kim, J. Han, K. H. Yeom, S. Lee, S. H. Baek, and V. N. Kim, "MicroRNA genes are transcribed by RNA polymerase II", *EMBO J.*, vol. 23, no. 20, pp. 4051-4060, 2004.

[30] A. M. Denli, B. B. J. Tops, R. H. A. Plasterk, R. F. Ketting, and G. J. Hannon, "Processing of primary microRNAs by the Microprocessor complex", *Nature*, vol. 432, no. 7014, pp. 231-235, 2004.

[31] T. P. Chendrimada, R. I. Gregory, E. Kumaraswamy, J. Norman, N. Cooch, K. Nishikura, and R. Shiekhattar. "TRBP recruits the Dicer complex to Ago2 for microRNA processing and gene silencing", *Nature*, vol. 436, no. 7051, pp. 740-744, 2005.

[32] A. A. Moustafa, H. Kim, R. S. Albeltagy, O. H. El-Habit, and A. B. A.-Mageed, "MicroRNAs in prostate cancer: From function to biomarker discovery", *Exp. Biol. Med.*, vol. 243, no. 10, pp. 817-825, 2018.

[33] X. Jin, Y. Chen, H. Chen, S. Fei, D. Chen, *et al.*, "Evaluation of Tumor-Derived Exosomal miRNA as Potential Diagnostic Biomarkers for Early-Stage Non–Small Cell

Lung Cancer Using Next-Generation Sequencing", *Clin. Cancer Res.*, vol. 23, no. 17, pp. 5311-5319, 2017.

[34] V. Y. Shin, J. M. Siu, I. Cheuk, E. K. O. Ng, and A. Kwong, "Circulating cell-free miRNAs as biomarker for triple-negative breast cancer", *Br. J. Cancer*, vol. 112, no. 11, pp. 1751-1759, 2015.

[35] K. Kai, R. L. Dittmar, and S. Sen, "Secretory microRNAs as biomarkers of cancer", *Semin. Cell Dev. Biol.*, vol. 78, pp. 22-36, 2018.

[36] T. Kilic, A. Erdem, M. Ozsoz, and S. Carrara, "microRNA biosensors: Opportunities and challenges among conventional and commercially available techniques", *Biosens. Bioelectron.*, vol. 99, pp. 525-546, 2018.

[37] D. L. Andrews, "A unified theory of radiative and radiationless molecular energy transfer", *Chem. Phys.*, vol. 135, no. 2, pp. 195-201, 1989.

[38] L. Stryer and R. P. Haugland, "Energy transfer: a spectroscopic ruler", *Proc. Natl. Acad. Sci. U. S. A.*, vol. 58, no. 2, pp. 719-726,1967.

[39] B. Schuler and W. A. Eaton, "Protein folding studied by single-molecule FRET", *Curr. Opin. Struct. Biol.*, vol. 18, no. 1, pp. 16-26, 2008.

[40] B. Prevo and E. J. G. Peterman, "Förster resonance energy transfer and kinesin motor proteins", *Chem. Soc. Rev.*, vol. 43, no. 4, pp. 1144-1155, 2014.

[41] J. Szöllosi, S. Damjanovich, and L. Mátyus, "Application of fluorescence resonance energy transfer in the clinical laboratory: Routine and research", *Cytometry*, vol. 34, no. 4, pp. 159-179, 1998.

[42] E. Hirata and E. Kiyokawa, "Future Perspective of Single-Molecule FRET Biosensors and Intravital FRET Microscopy", *Biophys. J.*, vol. 111, no. 6, pp. 1103-1111, 2016.

[43] S. Arshad Hussain, D. Dey, S. Chakraborty, J. Saha, A. D. Roy *et al.*, "Fluorescence Resonance Energy Transfer (FRET) sensor", *Sci. Letts. J.*, vol. 4, no. 19, 2015.

[44] R. B. Sekar and A. Periasamy, "Fluorescence resonance energy transfer (FRET) microscopy imaging of live cell protein localizations", *J. Cell Biol.*, vol. 160, no. 5, pp. 629-633, 2003.

[45] T. Főrster, "10th Spiers Memorial Lecture. Transfer mechanisms of electronic excitation", *Discuss. Faraday Soc.*, vol. 27, pp. 7-17, 1959.

[46] J. R. Lakowicz, *Principles of fluorescence spectroscopy*. Springer, 2006.

[47] T. Förster, "Zwischenmolekulare Energiewanderung und Fluoreszenz", *Ann. Phys.*, vol. 437, no. 1, pp. 55-75, 1948.

[48] H. C. Ishikawa-Ankerhold, R. Ankerhold, and G. P. C. Drummen, "Advanced Fluorescence Microscopy Techniques-FRAP, FLIP, FLAP, FRET and FLIM", *Molecules*, vol. 17, no. 4, pp. 4047-4132, 2012.

[49] D. Shrestha, A. Jenei, P. Nagy, G. Vereb, and J. Szöllősi, "Understanding FRET as a Research Tool for Cellular Studies", *Int. J. Mol. Sci.*, vol. 16, no. 12, pp. 6718-6756, 2015.

[50] M. Cebecauer, M. Spitaler, A. Sergé, and A. I. Magee, "Signalling complexes and clusters: functional advantages and methodological hurdles.," *J. Cell Sci.*, vol. 123, no. Pt 3, pp. 309-320, 2010.

[51] A. Miermont, F. Waharte, S. Hu, M. N. McClean, S. Bottani, S. Léon, and P. Hersena, "Severe osmotic compression triggers a slowdown of intracellular signaling, which can be explained by molecular crowding", *Proc. Natl. Acad. Sci.*, vol. 110, no. 14, pp. 5725-5730, 2013.

[52] E. A. Jares-Erijman and T. M. Jovin, "FRET imaging", *Nat. Biotechnol.*, vol. 21, no. 11, pp. 1387-1395, 2003.

[53] E. A. Jares-Erijman and T. M. Jovin, "Imaging molecular interactions in living cells by FRET microscopy", *Curr. Opin. Chem. Biol.*, vol. 10, no. 5, pp. 409-416, 2006.

[54] A. P. Bogiel and T. W. J. Gadella, "FRET microscopy: from principle to routine technology in cell biology", *J. Microsc.*, vol. 241, no. 2, pp. 111-118, 2011.

[55] D. M. Charron and G. Zheng, "Nanomedicine development guided by FRET imaging", *Nano Today*, vol. 18, pp. 124-136, 2018.

[56] R. Roy, S. Hohng, and T. Ha, "A practical guide to single-molecule FRET", *Nat. Methods*, vol. 5, no. 6, pp. 507-516, 2008.

[57] P. Maleki, J. B. Budhathoki, W. A. Roy, and H. Balci, "A practical guide to studying G-quadruplex structures using single-molecule FRET", *Mol. Genet. Genomics*, vol. 292, no. 3, pp. 483-498, 2017.

[58] B. Schuler, "Single-molecule FRET of protein structure and dynamics - a primer" *J. Nanobiotechnology*, vol. 11 Suppl 1, p. S2, 2013.

[59] E. Lerner, T. Cordes, A. Ingargiola, Y. Alhadid, S. Chung, X. Michalet, S. Weiss, "Toward dynamic structural biology: Two decades of single-molecule Förster resonance energy transfer", *Science*, vol. 359, no. 6373, pp. 1133, 2018.

[60] S. Spindel, J. Granek, and K. E. Sapsford, "*In Vitro* FRET Sensing, Diagnostics, and Personalized Medicine" in *FRET - Förster Resonance Energy Transfer*, Weinheim, Germany: Wiley-VCH Verlag GmbH & Co. KGaA, pp. 269-322, 2013.

[61] S. Zadran, S. Standley, K. Wong, E. Otiniano, A. Amighi, and M. Baudry, "Fluorescence resonance energy transfer (FRET)-based biosensors: visualizing cellular dynamics and bioenergetics", *Appl. Microbiol. Biotechnol.*, vol. 96, no. 4, pp. 895-902, 2012.

[62] V. Gubala, L. F. Harris, A. J. Ricco, M. X. Tan, and D. E. Williams, "Point of Care Diagnostics: Status and Future", *Anal. Chem.*, vol. 84, no. 2, pp. 487-515, 2012.

[63] G. P. Patrinos and W. Ansorge, *Molecular diagnostics*. Elsevier/Academic Press, 2010.

[64] W. W. Grody, *Molecular diagnostics : techniques and applications for the clinical laboratory*. Elsevier/Academic Press, 2010.

[65] L. Buckingham, *Molecular diagnostics : fundamentals, methods, and clinical applications*. F.A. Davis Company, 2012.

[66] W. R. Algar and U. J. Krull, "Towards multi-colour strategies for the detection of oligonucleotide hybridization using quantum dots as energy donors in fluorescence resonance energy transfer (FRET)", *Anal. Chim. Acta*, vol. 581, no. 2, pp. 193-201, 2007.

[67] V. V. Didenko, "DNA Probes Using Fluorescence Resonance Energy Transfer (FRET): Designs and Applications", *Biotechniques*, vol. 31, no. 5, pp. 1106-1121, 2001.

[68] E. Navarro, G. Serrano-Heras, M. J. Castaño, and J. Solera, "Real-time PCR detection chemistry", *Clin. Chim. Acta*, vol. 439, pp. 231-250, 2015.

[69] S. Shionoya, W. M. Yen, H. Yamamoto, *Phosphor handbook.* CRC Press/Taylor and Francis, 2007.

[70] J. Kido and Y. Okamoto, "Organo lanthanide metal complexes for electroluminescent materials", *Chem. Rev.*, vol. 102, no. 6, pp. 2357-2368, 2002.

[71] D. Tu, W. Zheng, Y. Liu, H. Zhu, and X. Chen, "Luminescent biodetection based on lanthanide-doped inorganic nanoprobes", *Coord. Chem. Rev.*, vol. 273, pp. 13-29, 2014.

[72] M. C. Heffern, L. M. Matosziuk, and T. J. Meade, "Lanthanide Probes for Bioresponsive Imaging", *Chem. Rev.*, vol. 114, no. 8, pp. 4496-4539, 2014.

[73] D. Kim, N. Lee, Y. Il Park, and T. Hyeon, "Recent Advances in Inorganic Nanoparticle-Based NIR Luminescence Imaging: Semiconductor Nanoparticles and Lanthanide Nanoparticles", *Bioconjug. Chem.*, vol. 28, no. 1, pp. 115-123, 2017.

[74] C. Zhao, Y. Sun, J. Ren, and X. Qu, "Recent progress in lanthanide complexes for DNA sensing and targeting specific DNA structures", *Inorganica Chim. Acta*, vol. 452, pp. 50-61, 2016.

[75] J. Vuojola and T. Soukka, "Luminescent lanthanide reporters: new concepts for use in bioanalytical applications", *Methods Appl. Fluoresc.*, vol. 2, no. 1, p. 012001, 2014.

[76] Y. Liu, D. Tu, H. Zhu, and X. Chen, "Lanthanide-doped luminescent nanoprobes: controlled synthesis, optical spectroscopy, and bioapplications", *Chem. Soc. Rev.*, vol. 42, no. 16, p. 6924, 2013.

[77] J.-C. G. Bünzli, "Lanthanide Luminescence for Biomedical Analyses and Imaging", *Chem. Rev.*, vol. 110, no. 5, pp. 2729-2755, 2010.

[78] Y. Zhang, W. Wei, G. K. Das, and T. T. Yang Tan, "Engineering lanthanide-based materials for nanomedicine", *J. Photochem. Photobiol. C Photochem. Rev.*, vol. 20, pp. 71-96, 2014.

[79] J.-C. G. Bünzli and C. Piguet, "Taking advantage of luminescent lanthanide ions", *Chem.*

Soc. Rev., vol. 34, no. 12, p. 1048, 2005.

[80] K. N. Allen and B. Imperiali, "Lanthanide-tagged proteins-an illuminating partnership", *Curr. Opin. Chem. Biol.*, vol. 14, no. 2, pp. 247-254, 2010.

[81] G. Blasse, "The influence of charge-transfer and rydberg states on the luminescence properties of lanthanides and actinides" in *Spectra and Chemical Interactions*, Berlin, Heidelberg: Springer Berlin Heidelberg, pp. 43-79, 1976.

[82] P. Dorenbos, "The 4fn↔4fn−15d transitions of the trivalent lanthanides in halogenides and chalcogenide", *J. Lumin.*, vol. 91, no. 1, pp. 91-106, 2000.

[83] S. A. Cotton, *Lanthanides and actinides.* Macmillan Education, 1991.

[84] K. A. Gschneidner, L. Eyring, and G. H. Lander, *Handbook on the physics and chemistry of rare earths.* vol. 32, North-Holland, 2001.

[85] M. H. V Werts, "Making sense of lanthanide luminescence" *Sci. Prog.*, vol. 88, no.2, pp. 101-131, 2005.

[86] A. Thibon and V. C. Pierre, "Principles of responsive lanthanide-based luminescent probes for cellular imaging", *Anal. Bioanal. Chem.*, vol. 394, no. 1, pp. 107-120, 2009.

[87] R. D. Teo, J. Termini, and H. B. Gray, "Lanthanides: Applications in Cancer Diagnosis and Therapy", *J. Med. Chem.*, vol. 59, no. 13, pp. 6012-6024, 2016.

[88] Y. Min, J. Li, F. Liu, P. Padmanabhan, E. K. L. Yeow, and B. Xing, "Recent Advance of Biological Molecular Imaging Based on Lanthanide-Doped Upconversion-Luminescent Nanomaterials", *Nanomaterials*, vol. 4, no. 1, pp. 129-154, 2014.

[89] H. U. Rashid, M. A. U. Martines, J. Jorge, P. M. Moraes, M. N. Umar, K. Khan, and H. U. Rehmana, "Cyclen-based Gd^{3+} complexes as MRI contrast agents: Relaxivity enhancement and ligand design", *Bioorg. Med. Chem.*, vol. 24, no. 22, pp. 5663-5684, 2016.

[90] S. Lacerda and É. Tóth, "Lanthanide Complexes in Molecular Magnetic Resonance Imaging and Theranostics", *Chem. Med. Chem.*, vol. 12, no. 12, pp. 883-894, 2017.

[91] T. Zhang, X. Zhu, W. K. Wong, H. L. Tam, and W. Y. Wong, "Light-Harvesting Ytterbium(III)-Porphyrinate-BODIPY Conjugates: Synthesis, Excitation-Energy Transfer, and Two-Photon-Induced Near-Infrared-Emission Studies", *Chem. Eur. J.*, vol. 19, no. 2, pp. 739-748, 2013.

[92] I. Hemmilä and V. Laitala, "Progress in Lanthanides as Luminescent Probes", *J. Fluoresc.*, vol. 15, no. 4, pp. 529-542, 2005.

[93] C. Lin, Y. Liu, and H. Yan, "Self-Assembled Combinatorial Encoding Nanoarrays for Multiplexed Biosensing", *Nano Lett.*, vol. 7, no. 2, pp. 507-512, 2007.

[94] K. Faulds, R. Jarvis, W. E. Smith, D. Graham, and R. Goodacre, "Multiplexed detection of six labelled oligonucleotides using surface enhanced resonance Raman scattering

(SERRS)", *Analyst*, vol. 133, no. 11, p. 1505, 2008.

[95] D. Cai, K. B. Cohen, T. Luo, J. W. Lichtman, and J. R. Sanes, "Improved tools for the Brainbow toolbox", *Nat. Methods*, vol. 10, no. 6, pp. 540-547, 2013.

[96] I. L. Medintz, D. Farrell, K. Susumu, S. A. Trammell, J. R. Deschamps *et al.*, "Multiplex Charge-Transfer Interactions between Quantum Dots and Peptide-Bridged Ruthenium Complexes", *Anal. Chem.*, vol. 81, no. 12, pp. 4831-4839, 2009.

[97] D. Geißler, L. J. Charbonnière, R. F. Ziessel, N. G. Butlin, H.-G. Löhmannsröben, and N. Hildebrandt, "Quantum Dot Biosensors for Ultrasensitive Multiplexed Diagnostics", *Angew. Chem. Int. Ed.*, vol. 49, no. 8, pp. 1396-1401, 2010.

[98] A. Waggoner, "Optical probes of membrane potential", *J. Membr. Biol.*, vol. 27, no. 1, pp. 317-334, 1976.

[99] A. J. Koning, P. Y. Lum, J. M. Williams, and R. Wright, "DiOC6 staining reveals organelle structure and dynamics in living yeast cells", *Cell Motil. Cytoskeleton*, vol. 25, no. 2, pp. 111-128, 1993.

[100] M. Terasaki, J. Song, J. R. Wong, M. J. Weiss, and L. B. Chen, "Localization of endoplasmic reticulum in living and glutaraldehyde-fixed cells with fluorescent dyes", *Cell*, vol. 38, no. 1, pp. 101-108, 1984.

[101] M. G. Honig and R. I. Hume, "Dil and diO: versatile fluorescent dyes for neuronal labelling and pathway tracing", *Trends Neurosci.*, vol. 12, no. 9, pp. 333-335, 1989.

[102] H. Y. Yang, Y. Fu, M. -S. Jang, Y. Li, J. H. Lee *et al.*, "Multifunctional Polymer Ligand Interface CdZnSeS/ZnS Quantum Dot/Cy3-Labeled Protein Pairs as Sensitive FRET Sensors", *ACS Appl. Mater. Interfaces*, vol. 8, no. 51, pp. 35021-35032, 2016.

[103] P. J. Cywiński, L. Olejko, and H.-G. Löhmannsröben, "A time-resolved luminescent competitive assay to detect L-selectin using aptamers as recognition elements," *Anal. Chim. Acta*, vol. 887, pp. 209-215, 2015.

[104] Y. Choi, L. Kotthoff, L. Olejko, U. Resch-Genger, and I. Bald, "DNA Origami-Based Förster Resonance Energy-Transfer Nanoarrays and Their Application as Ratiometric Sensors", *ACS Appl. Mater. Interfaces*, vol. 10, no. 27, pp. 23295-23302, 2018.

[105] A. Striolo, J. Ward, J. M. Prausnitz, W. J. Parak, D. Zanchet *et al.*, "Molecular Weight, Osmotic Second Virial Coefficient, and Extinction Coefficient of Colloidal CdSe Nanocrystals", *J. Phys. Chem. B*, vol. 106, no. 21, pp. 5500-5505, 2002.

[106] J. Weng and J. Ren, "Luminescent quantum dots: a very attractive and promising tool in biomedicine", *Curr. Med. Chem.*, vol. 13, no. 8, pp. 897-909, 2006.

[107] B. O. Dabbousi, J. R.-Viejo, F. V. Mikulec, J. R. Heine, H. Mattoussi *et al.*, "(CdSe)ZnS Core−Shell Quantum Dots: Synthesis and Characterization of a Size Series of Highly Luminescent Nanocrystallites", *J. Phys. Chem. B*, vol. 101, no. 46, pp. 9463-9475, 1997.

[108] A. J. Sutherland, "Quantum dots as luminescent probes in biological systems", *Curr.*

Opin. Solid State Mater. Sci., vol. 6, no. 4, pp. 365-370, 2002.

[109] P. Zrazhevskiy, M. Sena, and X. Gao, "Designing multifunctional quantum dots for bioimaging, detection, and drug delivery", *Chem. Soc. Rev.*, vol. 39, no. 11, p. 4326, 2010.

[110] E. Samimi, P. Karami, and M. J. Ahar, "A Review on Aptamer-Conjugated Quantum Dot Nanosystems for Cancer Imaging and Theranostic", *J. Nanomedicine Res.*, vol. 5, no. 3, p. 1, 2017.

[111] K. E. Sapsford, W. R. Algar, L. Berti, K. B. Gemmill, B. J. Casey *et al.*, "Functionalizing Nanoparticles with Biological Molecules: Developing Chemistries that Facilitate Nanotechnology", *Chem. Rev.*, vol. 113, no. 3, pp. 1904-2074, 2013.

[112] J. B. B.-Canosa, M. Wu, K. Susumu, E. Petryayeva, T. L.Jennings *et al.*, "Recent progress in the bioconjugation of quantum dots", *Coord. Chem. Rev.*, vol. 263, pp. 101-137, 2014.

[113] I. L. Medintz, H. T. Uyeda, E. R. Goldman, and H. Mattoussi, "Quantum dot bioconjugates for imaging, labelling and sensing", *Nat. Mater.*, vol. 4, no. 6, pp. 435-446, 2005.

[114] A. Foubert, N. V.Beloglazova, A. Rajkovic, B. Sas, A. Madder *et al.*, "Bioconjugation of quantum dots: Review & impact on future application", *TrAC Trends Anal. Chem.*, vol. 83, pp. 31-48, 2016.

[115] Y. Xing, Q. Chaudry, C. Shen, K. Y. Kong, H. E. Zhau *et al.*, "Bioconjugated quantum dots for multiplexed and quantitative immunohistochemistry", *Nat. Protoc.*, vol. 2, no. 5, pp. 1152-1165, 2007.

[116] A. Schroedter, H. Weller, R. Eritja, W. E. Ford, and J. M. Wessels, "Biofunctionalization of Silica-Coated CdTe and Gold Nanocrystals", *Nano Lett.*, vol. 2, no.12, pp. 1363-1367, 2002.

[117] H. Akkiraju, J. Bonor, and A. Nohe, "Development of Fluorescently Tagged BMP-2 analog", *Biophys. J.*, vol. 100, no. 3, p. 137a, 2011.

[118] X. Wei, Y. Wang, and Y. Bai, "Conjugation behaviours of CdTe quantum dots and antibody by a novel immunochromatographic method", *IET Nanobiotechnology*, vol. 5, no. 1, pp. 14-19, 2011.

[119] A. Hoshino, K. Fujioka, T. Oku, S. Nakamura, M. Suga *et al.*, "Quantum dots targeted to the assigned organelle in living cells", *Microbiol. Immunol.*, vol. 48, no. 12, pp. 985-994, 2004.

[120] J. M. Slocik, J. T. Moore, and D. W. Wright, "Monoclonal Antibody Recognition of Histidine-Rich Peptide Encapsulated Nanoclusters", *Nano Lett.*, vol. 2, no.3, pp. 1169-173, 2002.

[121] K. Boeneman, J. R. Deschamps, S. B.-White, D. E. Prasuhn, J. B. B.-Canosa *et al.*,

"Quantum Dot DNA Bioconjugates: Attachment Chemistry Strongly Influences the Resulting Composite Architecture", *ACS Nano*, vol. 4, no. 12, pp. 7253-7266, 2010.

[122] E. R. Goldman, E. D. Balighian, H. Mattoussi, M. K. Kuno, J. M. Mauro *et al.*, "Avidin: A Natural Bridge for Quantum Dot-Antibody Conjugates", *J. Am. Chem. Soc.*, vol. 124, no. 22, pp. 6378-6382, 2002.

[123] J. Zhou, Y. Yang, and C. Zhang, "Toward Biocompatible Semiconductor Quantum Dots: From Biosynthesis and Bioconjugation to Biomedical Application", *Chem. Rev.*, vol. 115, no. 21, pp. 11669-11717, 2015.

[124] E. Oh, M. Y. Hong, D. Lee, S. H. Nam, H. C. Yoon, and H. S. Kim, "Inhibition Assay of Biomolecules based on Fluorescence Resonance Energy Transfer (FRET) between Quantum Dots and Gold Nanoparticles", *J. Am. Chem. Soc.*, vol. 127, no. 10, pp. 3270-3271, 2005.

[125] M. Wu, E. Petryayeva, and W. R. Algar, "Quantum Dot-Based Concentric FRET Configuration for the Parallel Detection of Protease Activity and Concentration", *Anal. Chem.*, vol. 86, no. 22, pp. 11181-11188, 2014.

[126] M. K. So, C. Xu, A. M. Loening, S. S. Gambhir, and J. Rao, "Self-illuminating quantum dot conjugates for in vivo imaging", *Nat. Biotechnol.*, vol. 24, no. 3, pp. 339-343, 2006.

[127] R. Freeman, X. Liu, and I. Willner, "Chemiluminescent and Chemiluminescence Resonance Energy Transfer (CRET) Detection of DNA, Metal Ions, and Aptamer–Substrate Complexes Using Hemin/G-Quadruplexes and CdSe/ZnS Quantum Dots," *J. Am. Chem. Soc.*, vol. 133, no. 30, pp. 11597-11604, 2011.

[128] N. Hildebrandt, L. J. Charbonnière, and H.-G. Löhmannsröben, "Time-resolved analysis of a highly sensitive Förster resonance energy transfer immunoassay using terbium complexes as donors and quantum dots as acceptors", *J. Biomed. Biotechnol.*, vol. 2007, no. 7, p. 79169, 2007.

[129] S. Bhuckory, O. Lefebvre, X. Qiu, K. D. Wegner, and N. Hildebrandt, "Evaluating Quantum Dot Performance in Homogeneous FRET Immunoassays for Prostate Specific Antigen", *Sensors (Basel).*, vol. 16, no. 2, p. 197, 2016.

[130] W. R. Algar, D. Wegner, A. L. Huston, J. B. B.-Canosa, M. H. Stewart *et al.*, "Quantum Dots as Simultaneous Acceptors and Donors in Time-Gated Förster Resonance Energy Transfer Relays: Characterization and Biosensing", *J. Am. Chem. Soc.*, vol. 134, no. 3, pp. 1876-1891, Jan. 2012.

[131] S. Su, J. Fan, B. Xue, L. Yuwen, X. Liu *et al.*, "DNA-Conjugated Quantum Dot Nanoprobe for High-Sensitivity Fluorescent Detection of DNA and micro-RNA", *ACS Appl. Mater. Interfaces*, vol. 6, no. 2, pp. 1152-1157, 2014.

[132] D. J. Huang, Z. M. Huang, H. Y. Xiao, Z. K. Wu, L. J. Tang, and J. H. Jiang, "Protein scaffolded DNA tetrads enable efficient delivery and ultrasensitive imaging of miRNA through crosslinking hybridization chain reaction", *Chem. Sci.*, vol. 9, no. 21, pp. 4892-

4897, 2018.

[133] X. Qiu, J. Guo, Z. Jin, A. Petreto, I. L. Medintz, and N. Hildebrandt, “Multiplexed Nucleic Acid Hybridization Assays Using Single-FRET-Pair Distance-Tuning”, *Small*, vol. 13, no. 25, p. 1700332, 2017.

[134] Y. Zhao, F. Chen, Q. Li, L. Wang, and C. Fan, “Isothermal Amplification of Nucleic Acids”, *Chem. Rev.*, vol. 115, no. 22, pp. 12491-12545, 2015.

[135] M. Baker, “MicroRNA profiling: separating signal from noise,” *Nat. Methods*, vol. 7, no. 9, pp. 687-692, 2010.

[136] S. Ro, C. Park, J. Jin, K. M. Sanders, and W. Yan, “A PCR-based method for detection and quantification of small RNAs”, *Biochem. Biophys. Res. Commun.*, vol. 351, no. 3, pp. 756-763, 2006.

[137] Y. Zhou, Q. Huang, J. Gao, J. Lu, X. Shen, and C. Fan, “A dumbbell probe-mediated rolling circle amplification strategy for highly sensitive microRNA detection”, *Nucleic Acids Res.*, vol. 38, no. 15, p. 156, 2010.

[138] R. Deng, L. Tang, Q. Tian, Y. Wang, L. Lin, and J. Li, “Toehold-initiated Rolling Circle Amplification for Visualizing Individual MicroRNAs In Situ in Single Cells”, *Angew. Chem. Int. Ed.*, vol. 53, no. 9, pp. 2389-2393, 2014.

[139] W. Dai, H. Dong, K. Guo, and X. Zhang, “Near-infrared triggered strand displacement amplification for MicroRNA quantitative detection in single living cells”, *Chem. Sci.*, vol. 9, no. 7, pp. 1753-1759, 2018.

[140] X. Qu, H. Jin, Y. Liu, and Q. Sun, “Strand Displacement Amplification Reaction on Quantum Dot-Encoded Silica Bead for Visual Detection of Multiplex MicroRNAs”, *Anal. Chem.*, vol. 90, no. 5, pp. 3482-3489, 2018.

[141] H. Jia, Z. Li, C. Liu, and Y. Cheng, “Ultrasensitive Detection of microRNAs by Exponential Isothermal Amplification”, *Angew. Chem. Int. Ed.*, vol. 49, no. 32, pp. 5498-5501, 2010.

[142] R. M. Dirks and N. A. Pierce, “From The Cover: Triggered amplification by hybridization chain reaction”, *Proc. Natl. Acad. Sci.*, vol. 101, no. 43, pp. 15275-15278, 2004.

[143] Y. Chen, L. Chen, Y. Ou, L. Guo, and F. Fu, “Enzyme-free detection of DNA based on hybridization chain reaction amplification and fluorescence resonance energy transfer”, *Sensors Actuators B Chem.*, vol. 233, pp. 691-696, 2016.

[144] X. M. Shi, G. C. Fan, X. Tang, Q. Shen, and J. J. Zhu, “Ultrasensitive photoelectrochemical biosensor for the detection of HTLV-I DNA: A cascade signal amplification strategy integrating λ-exonuclease aided target recycling with hybridization chain reaction and enzyme catalysis”, *Biosens. Bioelectron.*, vol. 109, pp. 190-196, 2018.

[145] L. Yang, C. Liu, W. Ren, and Z. Li, "Graphene Surface-Anchored Fluorescence Sensor for Sensitive Detection of MicroRNA Coupled with Enzyme-Free Signal Amplification of Hybridization Chain Reaction", *ACS Appl. Mater. Interfaces*, vol. 4, no. 12, pp. 6450-6453, 2012.

[146] Z. Ge, M. Lin, P. Wang, H. Pei, J. Yan *et al.*, "Hybridization Chain Reaction Amplification of MicroRNA Detection with a Tetrahedral DNA Nanostructure-Based Electrochemical Biosensor", *Anal. Chem.*, vol. 86, no. 4, pp. 2124-2130, 2014.

[147] H. M. T. Choi, J. Y. Chang, L. A. Trinh, J. E. Padilla, S. E. Fraser, and N. A. Pierce, "Programmable in situ amplification for multiplexed imaging of mRNA expression", *Nat. Biotechnol.*, vol. 28, no. 11, pp. 1208-1212, 2010.

[148] J. Huang, H. Wang, X. Yang, K. Quan, Y. Yang *et al.*, "Fluorescence resonance energy transfer-based hybridization chain reaction for in situ visualization of tumor-related mRNA", *Chem. Sci.*, vol. 7, no. 6, pp. 3829-3835, 2016.

[149] X. Li, J. Li, C. Zhu, X. Zhang, and J. Chen, "A new electrochemical immunoassay for prion protein based on hybridization chain reaction with hemin/G-quadruplex DNAzyme", *Talanta*, vol. 182, pp. 292-298, 2018.

[150] R. Lin, Q. Feng, P. Li, P. Zhou, R. Wangm *et al.*, "A hybridization-chain-reaction-based method for amplifying immunosignals", *Nat. Methods*, vol. 15, no. 4, pp. 275-278, 2018.

[151] G. Zhu, S. Zhang, E. Song, J. Zheng, R. Hu *et al.*, "Building Fluorescent DNA Nanodevices on Target Living Cell Surfaces", *Angew. Chem. Int. Ed.*, vol. 52, no. 21, pp. 5490-5496, 2013.

[152] K. Quan, J. Li, J. Wang, N. Xie, Q. Wei *et al.*, "Dual-microRNA-controlled double-amplified cascaded logic DNA circuits for accurate discrimination of cell subtypes", *Chem. Sci.*, vol. 10, no. 5, pp. 1442-1449, 2019.

[153] H. Wang, C. Li, X. Liu, X. Zhou, and F. Wang, "Construction of an enzyme-free concatenated DNA circuit for signal amplification and intracellular imaging", *Chem. Sci.*, vol. 9, no. 26, pp. 5842-5849, 2018.

[154] B. Xie, Q. Ding, H. Han, and D. Wu, "miRCancer: a microRNA-cancer association database constructed by text mining on literature", *Bioinformatics*, vol. 29, no. 5, pp. 638-644, 2013.

[155] X. Yang, Y. Yu, and Z. Gao, "A Highly Sensitive Plasmonic DNA Assay Based on Triangular Silver Nanoprism Etching", *ACS Nano*, vol. 8, no. 5, pp. 4902-4907, 2014.

[156] M. Mandelkern, J. G. Elias, D. Eden, and D. M. Crothers, "The dimensions of DNA in solution", *J. Mol. Biol.*, vol. 152, no. 1, pp. 153-161, 1981.

[157] M. Nilsson, H. Malmgren, M. Samiotaki, M. Kwiatkowski, B. P. Chowdhary, and U. Landegren, "Padlock probes: circularizing oligonucleotides for localized DNA detection", *Science*, vol. 265, no. 5181, pp. 2085-2088, 1994.

[158] M. Nilsson, G. Barbany, D.-O. Antson, K. Gertow, and U. Landegren, "Enhanced detection and distinction of RNA by enzymatic probe ligation", *Nat. Biotechnol.*, vol. 18, no. 7, pp. 791-793, 2000.

[159] C. Larsson, J. Koch, A. Nygren, G. Janssen, A. K. Raap *et al.*, "In situ genotyping individual DNA molecules by target-primed rolling-circle amplification of padlock probes", *Nat. Methods*, vol. 1, no. 3, pp. 227-232, 2004.

[160] D. C. Thomas, G. A. Nardone, and S. K. Randall, "Amplification of padlock probes for DNA diagnostics by cascade rolling circle amplification or the polymerase chain reaction", *Arch. Pathol. Lab. Med.*, vol. 123, no. 12, pp. 1170-1176, 1999.

[161] S. P. Jonstrup, J. Koch, and J. Kjems, "A microRNA detection system based on padlock probes and rolling circle amplification", *RNA*, vol. 12, no. 9, pp. 1747-1752, 2006.

[162] H. Schwarzenbach, K. M.-Langosch, B. Steinbach, V. Müller, and K. Pantel, "Diagnostic potential of PTEN-targeting miR-214 in the blood of breast cancer patients", *Breast Cancer Res. Treat.*, vol. 134, no. 3, pp. 933-941, 2012.

[163] S. Li, Q. Qiang, H. Shana, M. Shi, G. Gan *et al.*, "MiR-20a and miR-20b negatively regulate autophagy by targeting RB1CC1/FIP200 in breast cancer cells", *Life Sci.*, vol. 147, pp. 143-152, 2016.

[164] F. M.-Aguilar, C. M. L.-Aguirre, J. C. M.-Rocha, J. A.-Chávez, V. Trevino e*t al.*, "Differential expression of miR-21, miR-125b and miR-191 in breast cancer tissue", *Asia. Pac. J. Clin. Oncol.*, vol. 9, no. 1, pp. 53-59, 2013.

[165] K. M. A.-Salah, M. M. Zourob, F. Mouffouk, S. A. Alrokayan, M. A. Alaamery, and A. A. Ansari, "DNA-Based Nanobiosensors as an Emerging Platform for Detection of Disease", *Sensors (Basel).*, vol. 15, no. 6, pp. 14539-14568, 2015.

[166] A. Kundu, S. Nandi, and A. K. Nandi, "Nucleic acid based polymer and nanoparticle conjugates: Synthesis, properties and applications", *Prog. Mater. Sci.*, vol. 88, pp. 136-185, 2017.

[167] J. Shi, F. Tian, J. Lyu, and M. Yang, "Nanoparticle based fluorescence resonance energy transfer (FRET) for biosensing applications", *J. Mater. Chem. B*, vol. 3, no. 35, pp. 6989-7005, 2015.

[168] A. Banerjee, T. Pons, N. Lequeux, and B. Dubertret, "Quantum dots-DNA bioconjugates: synthesis to applications", *Interface Focus*, vol. 6, no. 6, p. 20160064, 2016.

[169] C. Zhang, C. Ding, D. Xiang, L. Li, X. Ji *et al.*, "DNA Functionalized Fluorescent Quantum Dots for Bioanalytical Applications", *Chinese J. Chem.*, vol. 34, no. 3, pp. 317-325, 2016.

[170] G. Wang, Z. Li, and N. Ma, "Next-Generation DNA-Functionalized Quantum Dots as Biological Sensors", *ACS Chem. Biol.*, vol. 13, no. 7, pp. 1705-1713, 2018.

[171] M. Stanisavljevic, S. Krizkova, M. Vaculovicova, R. Kizek, and V. Adam, "Quantum

dots-fluorescence resonance energy transfer-based nanosensors and their application", *Biosens. Bioelectron.*, vol. 74, pp. 562-574, 2015.

[172] M. Cardoso Dos Santos and N. Hildebrandt, "Recent developments in lanthanide-to-quantum dot FRET using time-gated fluorescence detection and photon upconversion", *TrAC Trends Anal. Chem.*, vol. 84, pp. 60-71, 2016.

[173] Y. Lu, J. Zhao, R. Zhang, Y. Liu, D. Liu *et al.*, "Tunable lifetime multiplexing using luminescent nanocrystals", *Nat. Photonics*, vol. 8, no. 1, pp. 32-36, 2014.

[174] Y. Lu, J. Lu, J. Zhao, J. Cusido, F. M. Raymo *et al.*, "On-the-fly decoding luminescence lifetimes in the microsecond region for lanthanide-encoded suspension arrays", *Nat. Commun.*, vol. 5, no. 1, p. 3741, 2014.

[175] K. Hoffmann, T. Behnke, D. Drescher, J. Kneipp, and U. R.-Genger, "Near-Infrared-Emitting Nanoparticles for Lifetime-Based Multiplexed Analysis and Imaging of Living Cells", *ACS Nano*, vol. 7, no. 8, pp. 6674-6684, 2013.

[176] K. L. Hess, E. Oh, L. H. Tostanoski, J. I. Andorko, K. Susumu *et al.*, "Engineering Immunological Tolerance Using Quantum Dots to Tune the Density of Self-Antigen Display", *Adv. Funct. Mater.*, vol. 27, no. 22, p. 1700290, 2017.

[177] J. C. Breger, M. Muttenthaler, J. B. Delehanty, D. A. Thompson, E. Oh *et al.*, "Nanoparticle cellular uptake by dendritic wedge peptides: achieving single peptide facilitated delivery", *Nanoscale*, vol. 9, no. 29, pp. 10447-10464, 2017.

[178] B. C. Mei, K. Susumu, I. L. Medintz, J. B. Delehanty, T. J. Mountziaris, and H. Mattoussi, "Modular poly(ethylene glycol) ligands for biocompatible semiconductor and gold nanocrystals with extended pH and ionic stability", *J. Mater. Chem.*, vol. 18, no. 41, p. 4949, 2008.

[179] Y. T. Wu, X. Qiu, S. Lindbo, K. Susumu, I. L. Medintz *et al.*, "Quantum Dot-Based FRET Immunoassay for HER2 Using Ultrasmall Affinity Proteins", *Small*, vol. 14, no. 35, p. 1802266, 2018.

[180] W. R. Algar, M. G. Ancona, A. P. Malanoski, K. Susumu, and I. L. Medintz, "Assembly of a Concentric Förster Resonance Energy Transfer Relay on a Quantum Dot Scaffold: Characterization and Application to Multiplexed Protease Sensing", *ACS Nano*, vol. 6, no. 12, pp. 11044-11058, 2012.

[181] C. Chen, P. Zhang, G. Gao, D. Gao, Y. Yang *et al.*, "Near-Infrared-Emitting Two-Dimensional Codes Based on Lattice-Strained Core/(Doped) Shell Quantum Dots with Long Fluorescence Lifetime", *Adv. Mater.*, vol. 26, no. 36, pp. 6313-6317, 2014.

[182] B. C. Mei, K. Susumu, I. L. Medintz, and H. Mattoussi, "Polyethylene glycol-based bidentate ligands to enhance quantum dot and gold nanoparticle stability in biological media", *Nat. Protoc.*, vol. 4, no. 3, pp. 412-423, 2009.

9. Synthèse en français

Le cancer tue des millions de personnes chaque année, c'est l'un des plus grands problèmes de santé des êtres humains. Le prix Nobel de physiologie ou médecine 2018 a été décerné à James P. Allison et Tasuku Honjo pour leur découverte du traitement du cancer par inhibition de la régulation immunitaire négative. Si le cancer peut être diagnostiqué à un stade précoce, les chances de succès des traitements seront considérablement augmentées. Reconnaître les signes avant-coureurs possibles du cancer et agir rapidement mène à un diagnostic précoce.

L'une des meilleures façons de diagnostiquer précocement un cancer est d'identifier des biomarqueurs sériques ou tissulaires. Les biomarqueurs du cancer peuvent être de l'ADN, de l'ARN, des protéines, des métabolites ou des processus comme l'apoptose, l'angiogenèse ou la prolifération [1]. Ces biomarqueurs sont produits par la tumeur elle-même ou par d'autres tissus et peuvent se trouver dans divers fluides, tissus et lignées cellulaires, en réponse à la présence du cancer ou d'affections connexes. Les microARNs (miARNs), qui sont de petits (~22bp) ARNs non codants hautement conservés et exprimés de façon endogène dans chaque type cellulaire, ont émergé en tant que nouveau type de biomarqueur spécifique du cancer [2]. Ils fonctionnent comme des régulateurs de l'expression génétique en réduisant au silence des transcrits cibles par complémentation des paires de bases. Les miARNs peuvent être sécrétés par les cellules et se trouvent dans une variété de fluides corporels comme le sang, la salive et l'urine, où ils sont quantifiables et extrêmement stables [1]. Pour ces raisons, les miARNs sont considérés aujourd'hui comme des candidats idéaux en tant biomarqueurs non-invasifs pour le cancer.

La détection des acides nucléiques par transfert d'énergie de résonance de type Förster (FRET) est l'une des techniques les plus prometteuses qui peut répondre à presque toutes les exigences d'un diagnostic rapide, simple et multiplexé [3]. Le FRET est un transfert d'énergie non radiatif d'une molécule donneuse excitée (FRET-donneur) vers une molécule acceptrice à l'état fondamental (FRET-accepteur) par des interactions dipôle-dipôle [4]. Les principales conditions pour que le FRET apparaisse sont que le donneur et l'accepteur doivent être proches l'un de l'autre et qu'il doit exister un recouvrement spectral entre l'émission du donneur et l'excitation de l'accepteur. En raison de la forte dépendance à la distance entre le donneur et l'accepteur, les biocapteurs basés sur le principe du FRET sont très performants pour l'analyse des interactions biologiques et des changements structuraux à l'échelle nanométrique (environ 1 à 20 nm). Pour la plupart des tests de détection des acides nucléiques basés sur le FRET, le donneur et l'accepteur sont conjugués à l'ADN, le miARN ciblant cet ADN peut s'hybrider pour modifier la distance entre le donneur et l'accepteur, modifiant ainsi l'efficacité et la durée de vie du signal FRET. Les miARNs peuvent être détectés qualitativement et quantitativement par le changement de l'efficacité de FRET et de l'intensité de la photoluminescence (PL) du donneur ou de l'accepteur [5-9].

Avec le nombre croissant de systèmes de détection basés sur le FRET développés, de nombreux types de fluorophores ont été utilisés comme donneurs de FRET. Comparé aux fluorophores traditionnels, le complexe de lanthanide terbium (LTC) en tant que donneur de FRET présente des avantages uniques pour la détection par multiplexage avec différents accepteurs de FRET, comme les colorants organiques et les points quantiques ("quantum dots", QDs) [10-11]. En raison des transitions interdites f-f dans les ions terbium, le LTC possède des propriétés photo-physiques particulières, comme un grand décalage de Stokes, de multiples et étroites bandes d'émission et des durées de vie extrêmement longues (jusqu'à quelques millisecondes) qui permettent des mesures avec une sélection temporelle ("time-gated measurements", TG) [12]. Ces mesures en sélection temporelle (TG) permettent la distinction entre le signal FRET (longue durée de vie) et le bruit de fond dû à l'auto-fluorescence (de courte durée de vie) avec une très haute sensibilité de détection. Les bandes d'émission du Terbium (Tb) sont bien séparées et donc très bénéfiques pour le multiplexage spectral ; les temps de décroissance long et distinguables (en raison des différentes efficacités de FRET) des accepteurs sensibilisés offrent un grand potentiel pour le multiplexage temporel.

Les colorants ou sondes fluorescentes, aussi appelés fluorophores, sont des molécules non protéiques qui absorbent la lumière et la réémettent à une plus grande longueur d'onde. Ils sont utilisés dans les expériences biologiques depuis des décennies parce qu'ils sont faciles à manipuler et non toxiques. Les sondes fluorescentes offrent une plus grande photo-stabilité et luminosité que les protéines fluorescentes et ne nécessitent pas de temps de maturation. Les sondes fluorescentes sont également populaires en raison de leur rendement quantique élevé, de leur solubilité et de leur facilité de bio-conjugaison. Leur grande variété et leur grande disponibilité commerciale en ont fait la classe de fluorophores la plus fréquemment utilisée pour le FRET [13-14]. La combinaison de donneur LTC avec des sondes fluorescentes acceptrices a été utilisée dans des expériences de bio-détection multiplexée en FRET [15-16]. Bien qu'il soit possible de multiplexer les LTC et les sondes fluorescentes et d'obtenir une sensibilité élevée, la mauvaise séparation des spectres d'absorption et d'émission induit des interférences spectrales entre différents accepteurs durant le multiplexage spectral, et une correction appropriée est nécessaire.

Pour des bandes d'émission beaucoup plus étroites et des maximums de longueur d'onde d'émission réglables en fonction de leurs tailles, les QDs sont d'excellents candidats en tant qu'accepteurs de FRET pour le multiplexage. Les QDs ont plusieurs propriétés photo-physiques intrinsèques uniques : des rendements quantiques relativement élevés ; les QDs adaptables en taille et en type de matériau peuvent être utilisés pour donner un meilleur recouvrement spectral avec leur partenaire de FRET ; des coefficients d'extinction 10 à 100 fois supérieurs aux sondes fluorescentes, coefficients qui sont extrêmement importants pour le recouvrement spectral avec l'émission du LTC [17-18]. Des distances de Förster R_0 supérieures à 10 nm peuvent être obtenues avec des paires de FRET LTC-QD, ce qui est nettement supérieur aux valeurs de R_0 des paires donneur-accepteur conventionnelles [19-20]. La combinaison des LTC et des QDs pour des mesures de FRET a donc un potentiel très élevé (en termes de haute sensibilité et de grand R_0).

Cette thèse est divisée en six chapitres et est complétée par une annexe et la bibliographie. Après une introduction présentant le contexte de ce travail, trois projets individuels sont présentés. Chaque chapitre est organisé en une introduction, une section de matériel et méthode, les résultats, une discussion et une conclusion.

Le premier projet (**Figure 1.1**) présente des expériences de duplexage temporel pour la détection de miARNs en utilisant une seule paire de FRET Tb-sonde fluorescente et la technique de réaction d'hybridation en chaîne (HCR). J'ai fait la démonstration de la mise en œuvre du FRET en sélection temporelle (TG, "time-gated") entre les donneurs (Tb) et les accepteurs (sondes fluorescentes) en utilisant la technique de HCR pour la quantification multiplexée des miARNs (miR-20a et miR-21) et de leurs analogues d'ADN. Le HCR-TG-FRET a permis une quantification des acides nucléiques sans lavage avec des limites de détection (LOD) très basses, jusqu'à 240 attomoles (1,7 pM) de miARNs et 123 attomoles (0,88 pM) d'ADN. Une distinction efficace entre des miARNs très homologues a démontré une spécificité très élevée. Le multiplexage en une seule mesure, une seule longueur d'onde d'excitation et une seule paire de FRET a permis de quantifier simultanément miR-20a et miR-21 à des concentrations comprises entre 30 pM et 300 pM dans le même échantillon. Le HCR-TG-FRET a montré une performance similaire pour les échantillons avec ou sans sérum sans l'utilisation d'inhibiteurs de RNase. Nos résultats présentent une amélioration significative des approches actuelles par HCR en matière de simplicité, de sensibilité et de multiplexage. La performance diagnostique polyvalente du HCR-TG-FRET, même dans des environnements biologiques complexes, présente un avantage important pour la biodétection des acides nucléiques.

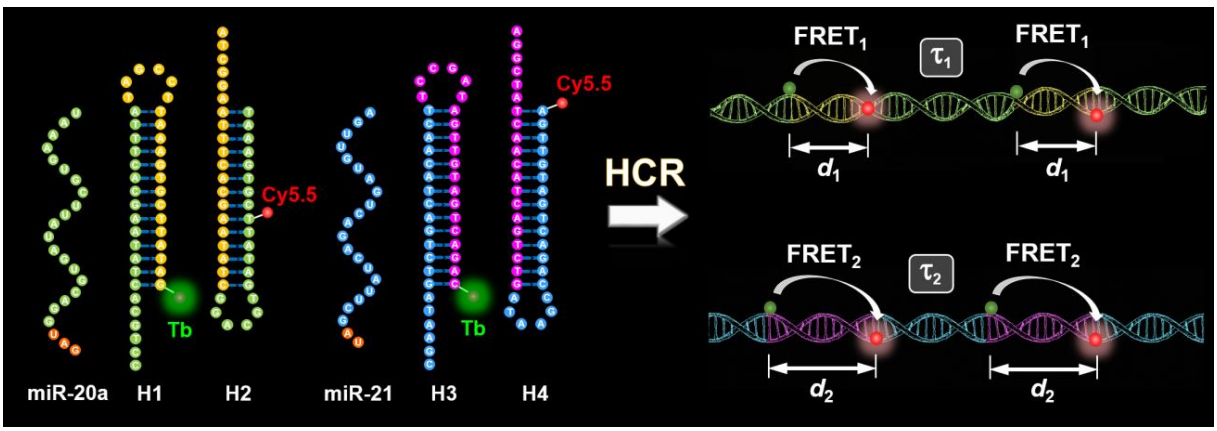

Figure 1.1. Représentation schématique pour la détection duplexée des miRNAs (miR-20a et miR-21) en utilisant le HCR-TG-FRET.

Dans le deuxième projet (**Figure 1.2**), j'ai combiné le multiplexage temporel et le multiplexage spectral, mis au point un test FRET Tb-sondes fluorescentes quadruplexé et un test RCA (amplification circulaire de l'ADN) pour la détection de l'ADN simple brin (ssDNA). Nous avons démontré la possibilité de faire une mesure de FRET en sélection temporelle d'un complexe Tb à longue durée de vie avec des sondes fluorescentes Cy3.5 et Cy5.5 pour le multiplexage spectro-temporel de quatre cibles d'ADN différentes dans le même échantillon (avec deux fenêtres temporelles et deux couleurs différentes). Nous avons utilisé l'amplification circulaire de l'ADN (RCA) pour obtenir une détection à haute sensibilité et pour placer les fragments d'ADN contenant les donneurs de FRET (Tb) et les fragments d'ADN contenant les sondes acceptrices à des distances contrôlées dans les concatémères d'ADN. Nous avons sélectionné quatre courts ADNs simple brins différents (ADN-20a, ADN-20b, ADN-21 et ADN-191), qui sont les équivalents ADN des miARNs hsa-mir-20a/20b/21/191, tous étant liés au cancer du sein. Le principe du RCA-FRET est que chaque cible d'ADN est reconnue par les séquences terminales d'une sonde à cadenas ("padlock probe") spécifique. Après cette étape d'hybridation, une ligase ferme le cadenas, qui transforme la cible en une amorce pour la synthèse ultérieure d'ADN. L'amplification de l'ADN par RCA est effectuée à 37 °C pendant 2 h et le produit d'amplification obtenu est marqué (hybridation spécifique) par des séquences d'ADN conjuguées à un donneur de FRET (Tb) ou des colorants accepteurs de FRET. Le choix précis de la distance entre les sondes d'ADN conduit à des déclins de PL spécifiques des paires donneur/accepteur de FRET utilisées et à une quantification simple, sans séparation (sans purification préalable de l'échantillon) et multiplexée de l'ADN. Le test de RCA-FRET a permis de distinguer des séquences d'ADN très homologues et a permis d'obtenir des limites de détection entre 40 et 570 zeptomoles (0,3 à 4,1 fM) pour quatre ADNs cibles différents. Nous avons démontré la possibilité de combiner les dimensions spectrale et temporelle de la PL pour un multiplexage d'ordre supérieur avec la dimension d'intensité du PL pour la quantification des quatre différents ADN à de faibles concentrations (fM) dans un même échantillon, en utilisant une seule source d'excitation et seulement deux couleurs de fluorescence.

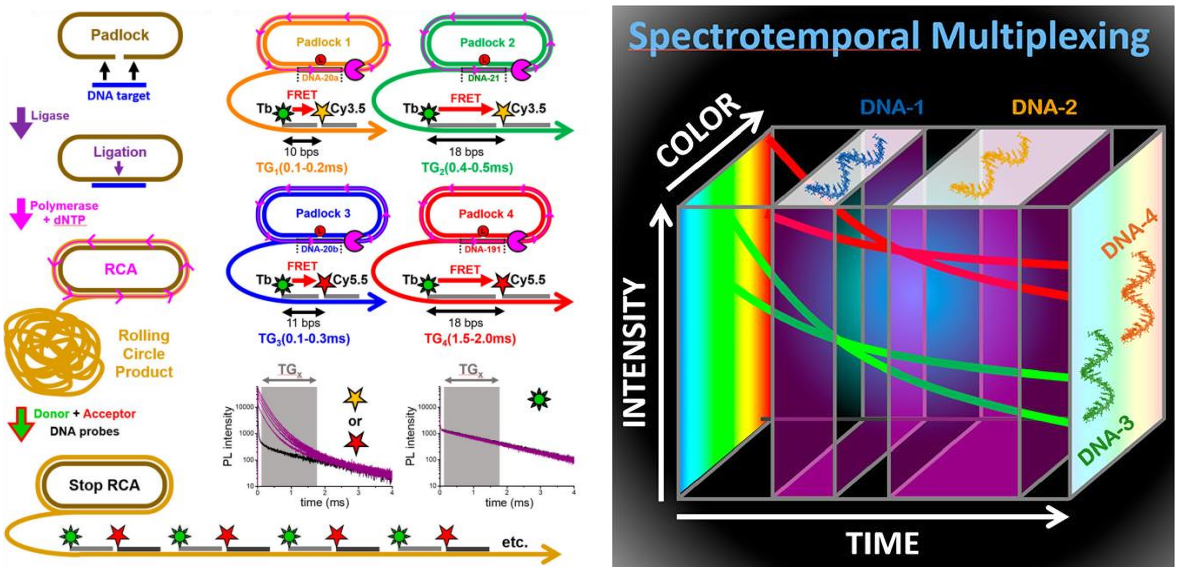

Figure 1.2. Le principe du test spectro-temporel quadruplexé de RCA-FRET et le multiplexage de la PL en trois dimensions. Axes x : durée de vie ; y : couleur ; z : Intensité PL.

Dans le troisième projet (**Figure 1.3**), j'ai étudié la FRET à multiplexage temporel Tb-QD en ajustant la longueur de l'ADN séparant les deux marqueurs Tb et QD. J'ai analysé par modélisation moléculaire et mesure de FRET résolue en temps 11 configurations d'un ADN de 31 nt de long, lié à un QD par une séquence peptide-His_6 (peptide-ADN), hybridé avec différentes sondes d'ADN complémentaires auxquelles est conjugué le Tb, l'hybridation des sondes à l'ADN séparant le Tb du QD par des distances de 0 à 26 nt. Nos résultats montrent que l'augmentation des distances Tb-QD a conduit à une augmentation de la durée de vie de la sensibilisation des QDs, les 11 configurations pouvant être identifiées sans "fitting" des courbes de décroissance de durée de vie de PL. Les déclins de PL temporellement distincts des différentes configurations d'ADN peuvent être utilisés pour des essais d'hybridation prototypiques. Un tel réglage fin des mesures de PL par déplacement du donneur de Tb de quelques nucléotides démontre la grande sensibilité du FRET à la distance donneur/accepteur et la possibilité d'étendre le multiplexage temporel à l'utilisation de nanoparticules tels que les QDs.

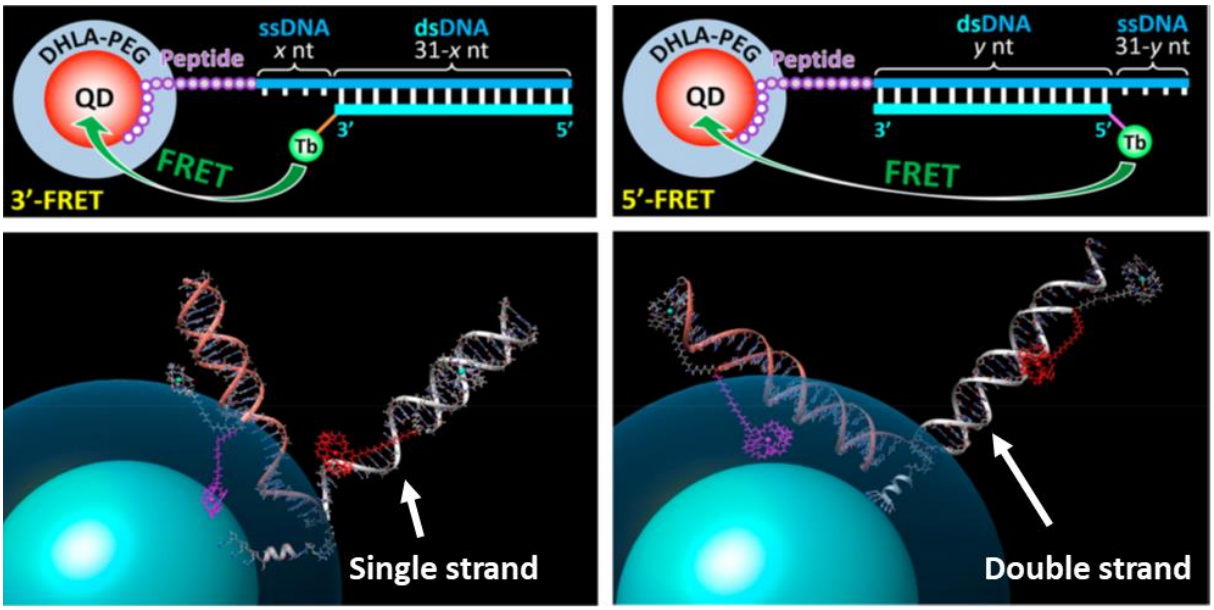

Figure 1.3. En haut : Représentation schématique du FRET Tb-QD à multiplexage temporel. En bas : La modélisation moléculaire a été utilisée pour calculer les distances Tb-QD dans les configurations de liaison de l'ADN parallèlement et verticalement à la surface.

Cette thèse présente trois applications réussites de l'FRET dans deux domaines de recherche distincts. Les deux premiers sont des biocapteurs LTC-Colorant FRET multiplexés pour la détection de biomarqueurs d'acides nucléiques liés au cancer, basés sur des méthodes d'amplification et des mesures à des lapse de temps déterminé. Nous avons utilisé deux stratégies pour réaliser la détection multiplexée, la détection temporelle multiplexée basée sur

les temps de décroissance remarquable d'une paire FRET LTC-Colorant et la détection spectral-temporelle multiplexé basée sur des spectres d'émission différents de différents colorants et des temps de décroissance différents de la même paire LTC-Colorant. Les méthodes de réaction en chaîne d'hybridation et d'amplification par cercle de roulant ont été combinées pour obtenir une sensibilité élevée et pour placer les Tb donneurs et les colorants accepteurs à des distances contrôlées sur l'ADN amplifié. Des mesures à des laps de temps déterminés ont été utilisées pour recueillir les intensités PL et calculer les contributions de différentes analytes dans différentes fenêtres temporelles à l'aide d'une simple matrice de calcul. La dernière est l'étude de conformation de l'ADN conjugué QD à simple et double brin par la durée de vie des FRET LTC-QD. Les résultats démontrent que les QD peuvent être utilisés pour la détection temporelle multiplexée et que la construction d'ADN Tb-QD FRET a un fort potentiel d'extension significative de la plage de multiplexage du concept de multiplexage temporel. Tous ces tests sont homogènes, aucun lavage ni séparation n'est nécessaire même avec le test amplifié. Ils sont tous spécifiques, peuvent distinguer des séquences très similaires. Toutes ces techniques de détection sont facilement transférables à d'autres cibles d'acides nucléiques.

Dans le premier travail, la capacité de multiplexage n'est pas limitée à deux, nous pouvons également essayer d'utiliser cette technique pour des essais triplex et la capacité en échantillons réels devrait également être déterminée dans les recherches futures. Dans le second travail, nous avons détecté quatre ADN différents, qui sont les équivalents ADN des miARNs. Nous n'avons pas détecté directement les miARN parce que les courbes d'étalonnage n'étaient pas linéaires. Il est difficile d'effectuer le calcul de la matrice avec des fonctions exponentielles, pour cela il faudrait faire plus d'optimisation pour les tests miRNA. Cette première démonstration de multiplexage spectral-temporel n'a quantifié que quatre ADN en combinant deux composantes spectrales et deux composantes temporelles, mais lorsque plus d'accepteurs différents et plus de fenêtres temporelles sont ajoutés, le nombre de cibles détectables dans un seul échantillon sera considérablement augmenté. La construction du complexe Tb-QD FRET ADN représente non seulement une alternative valable aux techniques d'analyse de conformation de l'ADN, mais elle a également un fort potentiel pour être utilisée pour développer des biocapteurs permettant de quantifier l'ADN à de faibles concentrations nano molaires. Les essais d'hybridation de preuve de concept ont démontré l'application possible de l'accord de distance Tb-QD basé sur l'ADN pour le multiplexage temporel d'ordre supérieur qui peut également être combiné avec plusieurs couleurs QD différentes.

université PARIS-SACLAY
ÉCOLE DOCTORALE
Physique et ingénierie : électrons, photons, sciences du vivant (EOBE)

Titre: Transfert d'énergie par résonance de type Förster résolu en temps pour la bio-détection multiplexée des acides nucléiques

Mots clés: FRET, complexe de lanthanide, multiplexage, résolue dans le temps, acides nucléiques

Résumé: Les biomarqueurs à base d'acides nucléiques, qui sont impliqués dans le contrôle de l'expression génétique, sont spécifiques de nombreux types de cancers. Les applications basées sur le transfert d'énergie par résonance de Förster (FRET) sont parmi les plus prometteuses pour la biodétection d'acides nucléiques. Comme la détection simultanée de plusieurs acides nucléiques est très demandée et que le multiplexage spectral est limité par des interférences (optical crosstalk), le multiplexage temporel est utilisé ici pour ajouter de nouvelles possibilités de multiples détections simultanées. La thèse porte sur le développement de systèmes comprenant différentes distances entre molécules donneuses et acceptrices de FRET (Terbium vers fluorophores) pour créer des signaux d'intensité spécifiques correspondant à différentes séquences d'acides nucléiques. Les distances Tb-to-dye peuvent être arrangées en positionnant spécifiquement le donneur Tb sur des molécules d'ADN de différentes longueurs. Les technologies d'amplification d'acides nucléiques, telles que la réaction d'hybridation en chaîne (HCR) et l'amplification circulaire de l'ADN (RCA), ont été utilisées pour obtenir simplicité, rapidité, sélectivité et sensibilité dans la détection d'acides nucléiques. Le multiplexage temporel du signal de FRET a également été combiné avec le multiplexage spectral (couleur) pour le démultiplier. De plus, la possibilité d'un multiplexage temporel à base de nanoparticules a été démontrée.

Title: Time-resolved Multiplexed Förster Resonance Energy Transfer for Nucleic Acid Biosensing

Keywords: FRET, lanthanide complex, multiplexing, time-resolved, nucleic acid

Abstract: Nucleic acid biomarkers, which involve in gene expression control, are found specific for many kinds of cancers. Förster Resonance Energy Transfer (FRET) based applications are one of the most promising for nucleic acid biosensing. As parallel detection of multiple nucleic acids is highly demanded and spectral multiplexing is limited by optical crosstalk, temporal multiplexing is used for opening another dimension of the multiplexing. The thesis focuses on developing different Tb-to-dye FRET distances to create specific intensity signals corresponding to different nucleic acid sequences. The Tb-dye distances can be tuned by specific location of the Tb donor using different lengths of DNA. Amplification technologies, such as hybridization chain reaction (HCR) and rolling circle amplification (RCA), are used to achieve simplicity, rapidity, selectivity, and sensitivity of nucleic acid detection. Temporal multiplexing FRET was also combined with spectral (color) multiplexing for higher order multiplexed detection. Moreover, a single Tb-QD FRET modeling demonstrated the possibility of nanoparticle-based temporal multiplexing.

Université Paris-Saclay
Espace Technologique / Immeuble Discovery
Route de l'Orme aux Merisiers RD 128 / 91190 Saint-Aubin, France